UNIVERSITÀ DEGLI STUDI DI MESSINA

Dottorato di Ricerca in Fisica - XXIX Ciclo

Isospin influence on dynamical and statistical emission of heavy fragments in heavy ion collisions at Fermi energies

Sebastianella Norella

PhD Thesis

Coordinatore:
Prof. L. Torrisi

Tutor:
Prof. A. Trifiró

SSD: FIS/04

Co-Tutor:
Dott. P. Russotto

Contents

Introduction

In semi-peripheral heavy-ion collisions at Fermi energies (20-100 $AMeV$), the reaction dynamics result mainly in binary products such as excited projectile-like (PLF) and target-like (TLF) fragments, that de-excite following an evaporation path. However also a dynamical IMFs (Intermediate Mass Fragments, defined as fragments of atomic number $Z \geq 3$) emission can take place. The production of these IMFs is due to different reaction mechanisms and different time scales [1]. The analysis of previous experiments (REVERSE and TIMESCALE), in which the systems $^{124,112}Sn+^{64,58}Ni$ at 35 $AMeV$ beam energy have been studied, has shown a well-defined chronology: light fragments ($Z < 9$) are mainly emitted in fast fragmentation of neck connecting PLF and TLF, while the emission of IMF with $Z \geq 9$ occurs at a later stage of the neck expansion process and it is dominated by an asymmetric mass splitting of the PLF in an aligned break-up configuration ("dynamical fission") or by a sequential statistical decay of the PLF. These different decay patterns for the PLF break-up are characterized by peculiar angular distributions. In order to estimate the weight of these two components (dynamical and statistical) the fission-like angular distributions were used. It resulted that the dynamical component becomes more important with increasing energy dissipation and-or mass asymmetry. Comparing the two systems ($^{124}Sn +^{64} Ni$ and $^{112}Sn +^{58} Ni$), it has been shown [2, 3] that while statistical fission probability is almost the same for the two reactions, the dynamical component is larger for the neutron rich system. This effect could be due to the different N/Z ratio of the two systems. However, some simulations have shown that it could also be related to the different size [4, 5].

In order to disentangle the effects related to the isopin from the ones related to the size of the two interacting systems, a new experiment, named InKiIsSy, has been carried out at Laboratori Nazionali del Sud in April 2013. During this experiment the $^{124}Xe +^{64} Zn$ reaction has been studied at 35 $AMeV$ beam energy, it has the same mass of the neutron rich system ($^{124}Sn +^{64} Ni$) and a N/Z ratio close to the value of the neutron poor one ($^{112}Sn +^{58} Ni$). During the InKiIsSy experiment also the $^{124}Xe +^{64} Ni$ system was analyzed, in order to compare two systems ($^{124}Xe +^{64} Zn$ and $^{124}Xe +^{64} Ni$) with same mass and beam but with different N/Z ratio for the target.

In this work the experimental results of these measurements will be shown, comparing them also with the ones of the REVERSE experiment.

Chapter 1

Heavy Ion Collisions at intermediate energies

1.1 Semi-peripheral reactions at Fermi energies

Semi-peripheral Heavy-Ion (HI) collisions at low energies ($E < 10\ AMeV$) are characterized by deep inelastic processes. The final states of these reactions are usually characterized by the presence of a massive fragment with velocity close to the projectile one, indicated with the term PLF (Projectile-Like Fragments), observed in coincidence with a fragment whose mass is close to the target one, indicated with the term TLF (Target-Like Fragment), as schematically shown in fig. 1.1. These primary fragments are often accompained by some reaction products coming from their statistical decay [6].

Increasing the beam energy into the Fermi energy domain (20-100 $AMeV$), these binary

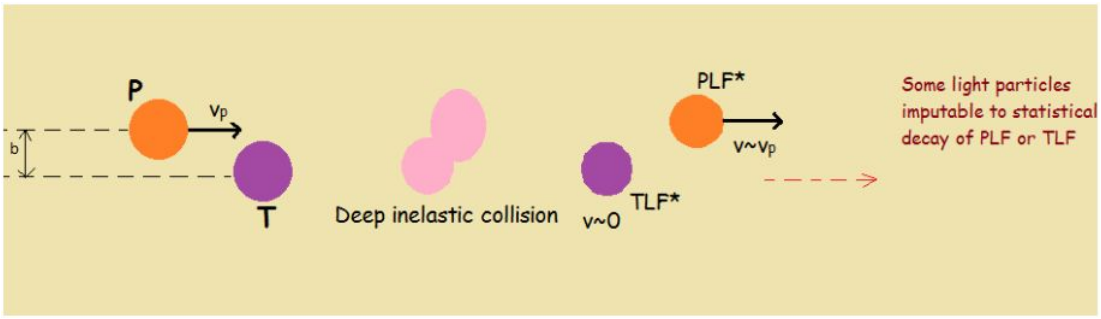

Figure 1.1: Schematic representation of semi-peripheral Heavy-Ion reaction at low energy ($E < 10AMeV$).

reactions begin to be accompained by a copious emission of IMFs (Intermediate Mass Fragments), defined as fragments of atomic number $3 \leq Z \leq 20$. IMFs show a typical kinematics distribution centred at a velocity intermediate between that of Target-Like Fragment

and the one of Projectile-Like Fragment (fig. 1.2); it follows that their emission could not be explained by the statistical PLF or TLF decay alone [1, 7, 8, 9, 10, 11, 12, 13, 14]. The

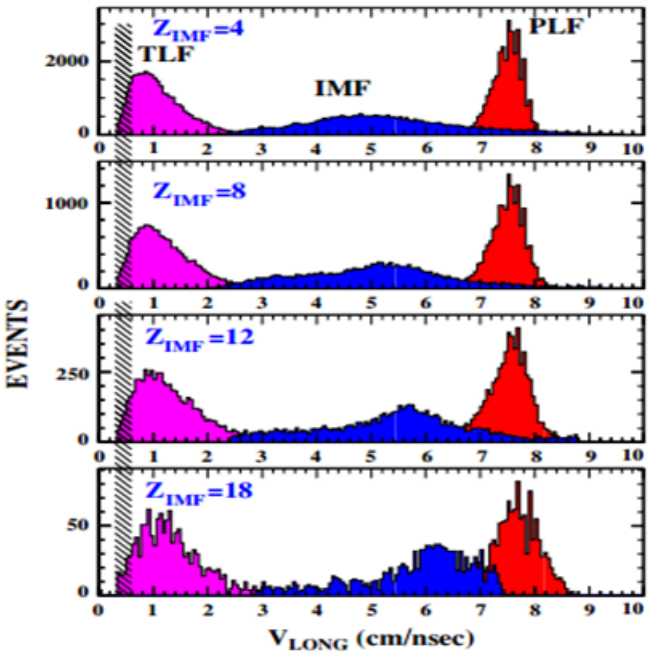

Figure 1.2: Longitudinal velocity distribution of PLF, TLF and IMF for $Z_{IMFs} = 4, 8, 12, 18$ for $^{124}Sn +^{64} Ni$ system [1].

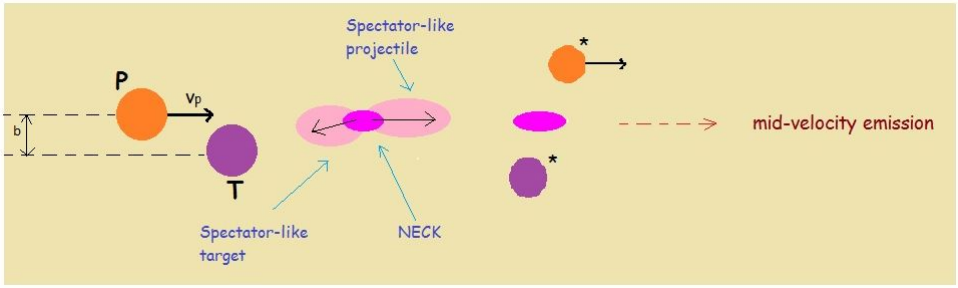

Figure 1.3: A schematic representation of neck emission process.

production of these IMFs may involve different timescales and different reaction mechanisms [1], ranging from a prompt fragmentation of the neck to a fast non-equilibrated fission-like mechanism or an equilibrated sequential decay. The observation of fig. 1.2 suggests that lighter IMFs are probably emitted from a transient neck matter zone connecting PLF and TLF, during reseparation of these two fragments. Fig. 1.3 shows a schematic representation of this neck emission process. Moreover light particles and IMFs emitted in the mid-rapidity region velocity are neutron richer than fragments statistically emitted from the PLF/TLF source [10]. Several experiments have been performed in order

to investigate the mechanisms of formation of these fragments. In particular, the systems $^{124}Sn + ^{64}Ni$ and $^{112}Sn + ^{58}Ni$ at 35 $AMeV$ beam energy were investigated in the REVERSE experiment, performed at LNS of Catania. In ref. [1] the so-called "ternary events" were considered. They are those semiperipheral reactions in which one can observe a production of IMF in almost ideal condition, since the final-state configuration involves one IMF accompanying PLF and TLF. The REVERSE experiment was undertaken using the forward part of CHIMERA array [15]. The inverse kinematics of these reactions allowed to detect and easily distinguish ternary events. Infact, in these conditions, the reaction products are focused at forward angle, where CHIMERA detector presents almost 85% of detection efficiency [16]. Fig. 1.4 presents the two-dimensional distribution of fragments for the $^{124}Sn + ^{64}Ni$ reaction as a function of Z of a given fragment and its parallel velocity along the beam axis. In this plot it's possible to distinguish three strongly popu-

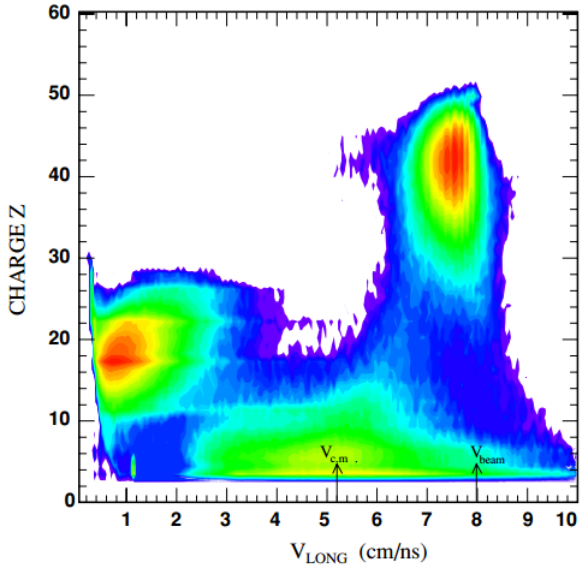

Figure 1.4: Distribution of fragments for the $^{124}Sn + ^{64}Ni$ reaction as a function of their atomic number Z and their longitudinal velocity [1].

lated regions, recognized as PLF, TLF and IMF regions. In particular, the PLFs cover the area corresponding to heavy and relatively fast fragments of atomic number approaching the Z of Sn projectile ($Z_{proj} = 50$) and moving with velocities close to the projectiles ones, while TLFs cover the region around $Z \sim 18$ and $v_{long} \sim 1$ cm/ns. Instead, IMFs cover the region of intermediate velocities. They are mostly light fragments, but they can have also larger Z values, up to $Z = 18 - 20$. As shown in fig. 1.2 where a plot of longitudinal velocity in laboratory reference frame for the three classes of fragments (PLF, TLF and IMF) for different Z_{IMF} (IMF atomic number) in the case of $^{124}Sn + ^{64}Ni$ reaction is reported [1], the average longitudinal velocity of IMF can be correlated with the velocity

intermediate between the parallel velocities of TLF and PLF. Moreover, the longitudinal velocity of lighter IMF increases with increasing of IMF atomic number Z_{IMF}, showing a strong kinematical correlation with PLF for heavier IMF. In order to obtain important information on the mechanism of these ternary reactons, relative velocities characterizing binary subsystems of the total three body system were examined. In particular, correlations between relative velocities of IMF with respect to PLF (V_{rel}(IMF,PLF)) and TLF (V_{rel}(IMF,TLF)) were analyzed. These relative velocities were normalized to the velocity V_{Viola} corresponding to the kinetic energy due to Coulomb repulsion for the binary subsystems as given by the Viola systematic [17]. The correlation between relative velocities for $Z_{IMF} = 4, 8, 12, 18$ are shown in fig. 1.5, from ref. [1]. This kind of correlation gives infor-

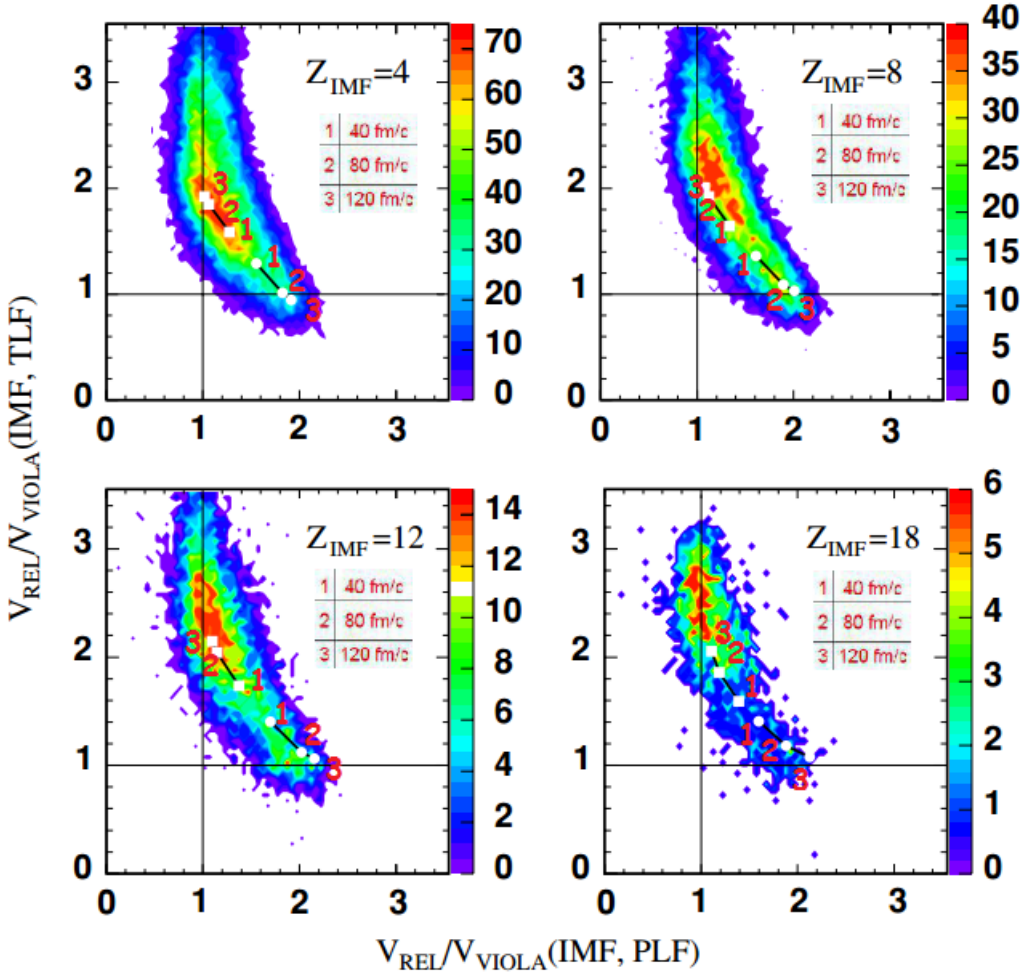

Figure 1.5: Correlations between relative velocities V_{rel}/V_{Viola}(IMF,PLF) and V_{rel}/V_{Viola}(IMF,TLF) for different intermediate mass fragments of $Z_{IMF} = 4, 8, 12, 18$. Experimental distributions are compared with model calculations assuming that the IMF is released from the projectile (squares) or from target nucleus (circles) after a time interval of 40, 80 or 120 fm/c from the re-separation of the primary binary system at $t = 0$ [1].

mation on the scenario of IMF formation and on the time when the IMF separates from

PLF or TLF (or from both in the case of the instantaneous ternary split). The experimental distributions are compared with model calculations assuming that the IMF is released from the projectile (squares) or from target nucleus (circles) after a time interval of 40, 80 or 120 fm/c from the re-separation of the primary binary system at $t = 0$ [1, 10]. Beyond 120 fm/c the predicted points of the V_{rel}/V_{Viola}(IMF,PLF) vs V_{rel}/V_{Viola}(IMF,TLF) correlation become undistinguishable from much later "true" sequential decay processes [18]. Specifically, considering the V_{rel}/V_{Viola}(IMF,PLF) vs V_{rel}/V_{Viola}(IMF,TLF) plots, events close to the diagonal correspond to prompt ternary divisions (emission of IMF from the neck matter connecting PLF and TLF at its early stage of expansion), while events approaching V_{rel}/V_{Viola}(IMF,PLF)=1 and V_{rel}/V_{Viola}(IMF,TLF)=1 correspond to the sequential split of the primary projectile-like nucleus or the target-like nucleus, respectively. As it's possible to see from the localization of events in the relative velocity correlation plot, the majority of light IMFs with $Z_{IMF} <\sim 10$ are emitted in almost prompt or "fast two-step" processes, within times of about 40-80 fm/c. Instead, the heavier IMFs ($Z_{IMF} >\sim 10$) are preferentially emitted not immediately after reseparation of the colliding nuclei, but rather in somewhat later stage, starting at times of about 120 fm/c. Within the time interval of about 100 fm/c the studied system moves over a distance of about 20 fm, comparable with its size; so the emission of these IMFs (at times of about 120 fm/c) can still be associated with fragmentation of the neck formed between the nuclei after collision. This process is intermediate between a genuine prompt ternary decay of the colliding system and true sequential decay of projectile nucleus. In this case, in which the deduced time intervals extend up to 120 fm/c, it is possible that a two-step process takes place: the double break of a massive neck stretched between the receding nuclei, in which the neck first separates from TLF, and then breaks away from PLF. In this scenario, one can suppose that to form heavy IMFs more matter is required in the neck region, that is, the neck must be considerably stretched, so the second break of the neck must happen after a longer time. Sometimes, instead, the breaking of the neck can take place at its waist leaving most of the neck matter on one of the participating nuclei. This deformation could be absorbed with consequent statistical cooling, or, in others cases its relaxation could happen via a fragments emission. In this latter case heavy IMFs could be emitted by the fast splitting of a higly excited and deformed nucleus, a process that can be associated with the scenario of "Dynamical fission" reactions [19, 10]. In fact, the term "Dynamical Fission" indicates the process in which the projectile-like fragment (or target-like fragment), after interaction with the target (or the projectile), fissions so fast that angular distribution of fission fragments is not forward/backward symmetric. In both processes, dynamical fission and neck fission, a clear enhanced emission localized in the mid-rapidity region, intermediate between PLF and TLF rapidity, is obtained, resulting in

a clear anisotropy of the IMFs angular distributions, that indicates a preferential emission direction and an alignment tendency.

1.2 Dynamical and statistical effects in heavy ion collisions

As previously said, in HI collisions the production of light charged particles and Intermediate Mass Fragments (IMFs) is due to different reaction mechanisms and involve different time scales, ranging from fast dynamical processes to statistical emission from equilibrated sources. The statistical aspects are dominant in low energy ractions ($E <\sim 10$ $AMeV$) and, in this case, any memory of the entrance channel is forgotten. Instead, in Fermi energies regime dynamical aspects become more important. In particular, as discussed in the previous paragraph, heavier fragments emission may be associated with a PLF binary-like splitting taking places ideally in dynamical or equilibrated way. These two different decay modes for the PLF break-up, are characterized by peculiar angular distributions: an aligned break-up with the recoil velocity of the PLF source in the dynamical emission and an isotropic (neglecting spin effects) emission of fission-like fragments (in the PLF reference frame) in the sequential statistical decay.
In fact, in the case of sequential break-up both the dynamics of the previous collision and the characteristic equilibration times of various degrees of freedom come into play and the break-up step could give informations about dynamic and temporal aspects of the reaction. Varios experiments [20, 21] have shown that fission of hot nuclei occurs more slowly than as predicted by the standard transition-state theory of Bohr and Wheeler [22]. On the other hand, others obsevations point to opposite effect: a spectacular acceleration of nuclear fission. In order to investigate these effects, peripheral heavy ion collisions with three-four massive fragments in the exit channel were studied. In this respect, the systems $^{86}Kr +^{166} Er$ and $^{129}Xe +^{122} Sn$ were investigated at 12.5 $AMeV$ beam energy [23]. For these reaction it was found that the three body events occur with a large probability with respect to the statistical model predictions. These events are mainly originated by a two-step mechanism and they are compatible with hypothesis of a binary deep-inelastic interaction, followed by the further fission-like decay of one of the primary fragments. Moreover, the magnitude of the modulation of energy released in the second fission step, induced by strong Coulomb proximity effects, depends on the time between first and second scission step. It establishes a clock of the order of 10^{-21} s, that is two order of magnitude smaller than time scale given by statistical framework. Besides, the angular distribution of the fragments was found consistend with an orientation of the fission axis approximately collinear with the axis of the first scission. All these features are consistent

with an intermediate fissioning system not fully equilibrated.
Further non-equilibrium effects were observed for the $^{100}Mo + ^{100}Mo$ and $^{120}Sn + ^{120}Sn$ reactions, studied at 20 $AMeV$ beam energy [9, 24]. Also here it was shown that, for the three-four heavy (with $A \geq 20$) fragments events, the reaction takes place through a two-step mechanism: a first dissipative binary reaction between projectile and target, followed by a sequential fission decay. Considering the in-plane angular distributions (see next section for definition) for products of sequential fission of primary binary fragments (PLF or TLF) for various mass asymmetries ($\eta = \frac{A_{Heavy} - A_{Light}}{A_{Heavy} + A_{Light}}$) of the fission step (fig. 1.6), it's possible to see that, for moderate fission fragments mass asymmetry (panel 1), the angular distribution is quite flat. This indicates that there is not a preferential emission direction

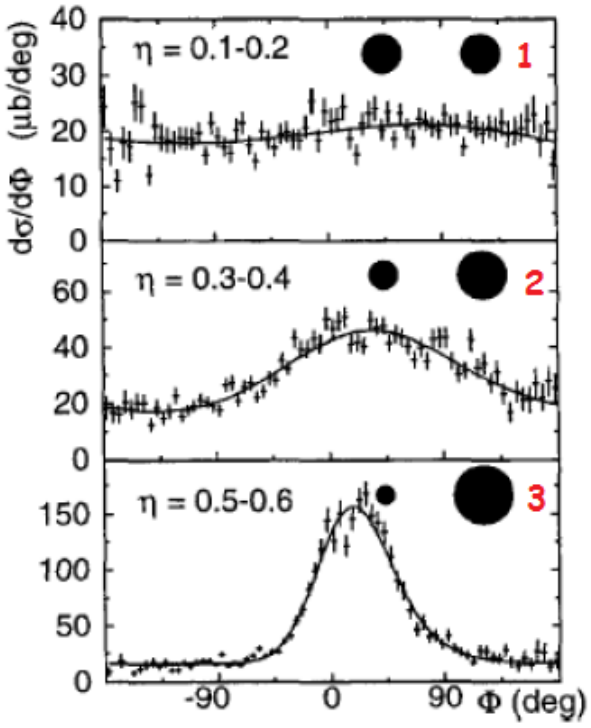

Figure 1.6: In-plane angular distributions of sequential fission of primary binary fragments (PLF or TLF) produced in $^{100}Mo + ^{100}Mo$ reaction for various mass asymmetries, panel 1: $\eta = 0.1 - 0.2$, panel 2: $\eta = 0.3 - 0.4$, panel 3: $\eta = 0.5 - 0.6$, of the fission step [9, 24].

and the memory of the formation of the system is lost (pure sequential fission). Instead, increasing mass asymmetry, the angular distributions are peaked at small positive angles, which corresponds to an aligned configuration of the three nuclei: the non-fissioning primary TLF (or PLF) and the two PLF (or TLF) fission fragments. Moreover, in this case, the smaller of the two fission fragments stays in the middle, demonstrating the persistency of a memory of the preceding deep-inelastic step and of direction of the separation axis between TLF and PLF. The observed forward/backward asymmetry indicates a short time

for the fission, that was there extrapolated following the model below exposed [9, 24]. In the case of asymmetric fission, fitting the angular distribution, the peak at small angles may be associated with an angle φ_m that describes the average rotation of the nucleus from scission to scission. If the fissioning nucleus is characterized by a collective "angular velocity" ω, it's possible to estimate the scission to scission lifetime as $\tau = \varphi_m/\omega$. In particular, as shown in fig. 1.7, while at symmetry the scission to scission lifetimes are compatible with those expected for fission after attainment of global equilibrium, at high asymmetry lifetimes become of the order of $1 - 5 \cdot 10^{-21}$ s (typical of quasi-fission process), at least two order of magnitude smaller with respect to lifetime characteristic of a statistical process [23]. In this case the second scission should happen after only a fraction of full

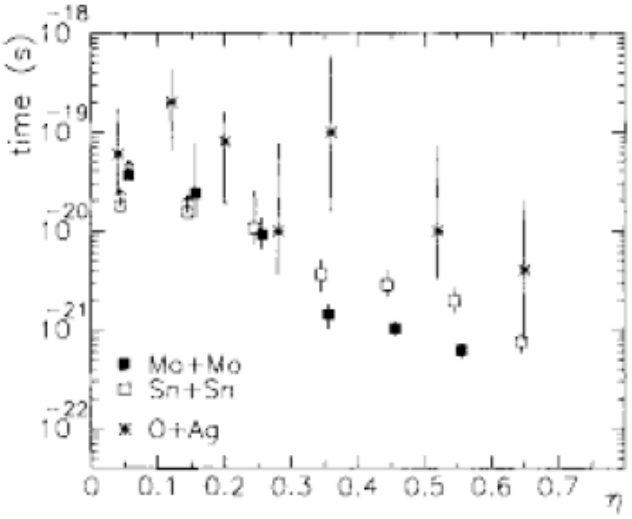

Figure 1.7: Scission to scission lifetime τ, extracted from angular distribution of figure 1.6, as a function of fission fragments mass asymmetry for $^{100}Mo + ^{100}Mo$ and $^{120}Sn + ^{120}Sn$ reactions around 20 $AMeV$. Moreover, statistical fission compatible lifetimes obtained in other studies [25] are reported.

rotation [26], without passing through the stage of a true compound nucleus. Therefore, HI collisions show PLF break-up, not only from statistical fission process, but also from a fast/non equilibrated break-up (dynamical fission).

Other studies on the binary break-up of PLF were made for various reactions (like Pb+Ag and Xe+Sn) and incident energies (20-50 $AMeV$) [13]. For these systems it was found that, while for heavy projectiles impinging on light target (Pb+Al, U+C) the PLF break-up occurs mainly in two approximately equal size fragments (as expected for the statistical fission of a heavy nucleus), in the case of heavy targets (Pb+Au, U+U) the break-up of PLFs shows in addition an important contribution for the highest asymmetries, that increases with the size of the target. So, in this case, the break-up of PLF depends strongly

on the target size. Moreover, while for light targets the angular distributions of fission fragments are forward/backward symmetric in PLF reference system (as expected in standard fission of a rotating nucleus), for heavy targets and greater fission fragments mass asymmetries the break-up axis is preferentially aligned with the separation direction of the two primary fragments (PLF and TLF), with the lighter fragments backward emitted in the PLF reference (aligned break-up). In ref. [13] the relative importance of these mechanisms has also been quantified. In the case of Pb+Ag at 29 $AMeV$, the standard fission represents 85% of the total number of events. Instead, for the Xe+Sn system the standard fission represents only 25% of the total PLF break-up events, whatever is the incident energy (39, 45, 50 $AMeV$) or the impact parameter. The difference between the two reactions is due to different fissility of the two projectiles. There it has been hypothesized that, in the case of dynamical fission, after the collision, the deformation is so large that the projectile-like fragment goes inevitably towards break-up. In this case, the PLF, unlike the case of a standard fission, doesn't return to an equilibrated shape before break-up; its deformation is as large as the deformation of the same nucleus at the saddle point in a standard fission process. In particular, the process is continuous and the relative velocity associated to a saddle point is different from zero. The observed relative velocity is the addition of the Coulomb repulsion and deformation velocity of the PLF.
Other studies about PLF break-up were performed by Colin et al. [12]. They, analyzing the IMF multiple production for the Xe+Sn, U+U, Ni+Ni and Ta+U systems at energies ranging from 24 to 90 $AMeV$, showed the persistency of heavier fragment, originated in binary or multi PLF break-up, to be forward emitted in PLF reference system, suggesting a clear dynamical effect. They also observed a sort of "hierarchy effect", not consistent with the decay of a fully equilibrated nucleus, for which the ranking in bigger charge induces, on average, the ranking in bigger parallel to the beam velocity. According to this effect, the PLF (or TLF) is strongly deformed; this deformation is followed by the break-up of these elongated nuclei in two or more fragments (neck formation and multiple break-up) (fig. 1.8). The fragments emitted by this neck reflect its internal structure: its size, at the centre of mass, is on average thinner than close to the PLF or TLF, and the velocity moduli (in the center of mass reference frame) of the nucleons in the neck are smaller than those of nucleons close to the PLF or to the TLF [12]. The hierarchy effect is stronger when the fissility of the PLF is limited ($Z < 80$), the size of the target is large and the incident energy is high. Also in refs. [7, 27, 28] are presented other observations of aligned break-up of the PLF at Fermi energies. Also there, it's possible to find that binary break-up of PLF follows different decay patterns, from equilibrated emission towards dynamical one. Other importan informations on this item comes from results of the REVERSE experiment.

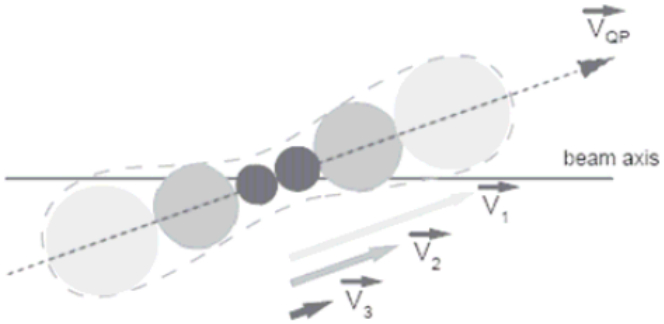

Figure 1.8: Schematic view of the fragmentation scenario leading to the "hierarchy effect" ([12]). The shading darkens according to the charge decreasing of the fragments.

1.2.1 Dynamical fission as seen in the REVERSE experiment.

One of the main focuses of the REVERSE experiment was to study the decay properties of Projectile-Like Fragments in $^{124,112}Sn(35\ AMeV)+^{64,58}Ni$ semi-peripheral collisions [30, 10]. PLF, after scattering from TLF, may undergo splitting into two massive fragments, strongly correlated in charge and in velocity space. These two fragments (named as Heavy (H) and Light (L) according to their atomic number) have values of Z such that their sum is close to the charge of the projectile ($Z_{proj} = 50$), that is $37 \leq Z_{2F}(= Z_H + Z_L) \leq 57$. Moreover, in the selected events, the heavy-to-light-fragment mass ratio was $A_H/A_L < 4.6$, so that the lighter fragment of the two has charge $Z_L \gtrsim 9$.
In order to select semi-peripheral collisions the method of Cavata et al. [29] (explained in Appendix A) was used; it allows to estimate the impact parameter from the total charged-particle multiplicity M_{tot}. Specifically, in this case, the events selected were those with reduced impact parameter $b_{red} \geq 0.7$, that corresponds to $M_{tot} \leq 6$ for the neutron-rich system and $M_{tot} \leq 7$ for neutron-poor one.
The analysis was performed as a function of the fission-like fragments Heavy/Light mass asymmetry (A_H/A_L) and kinetic energy loss [10, 30]. In particular, considering the V_{par} (velocity component along the beam direction) versus V_{per} (velocity component orthogonal to the beam direction) Galilean-invariant plots for Light fragments produced in the $^{124}Sn+^{64}Ni$ reaction for different mass asymmetry and energy dissipation shown in fig. 1.9, it's possible to see in all panels the characteristic Coulomb rings centred slightly below the beam velocity ($V_b \sim 8\ cm/ns$). The presence of these rings points to PLF* (primary exited PLF) as a well-defined decay source and confirms the scenario of two separate reaction steps: first the formation of PLF* and, then, its splitting into two fragments. As it's possible to see in fig. 1.9, for almost symmetric divisions after less dissipative collisions

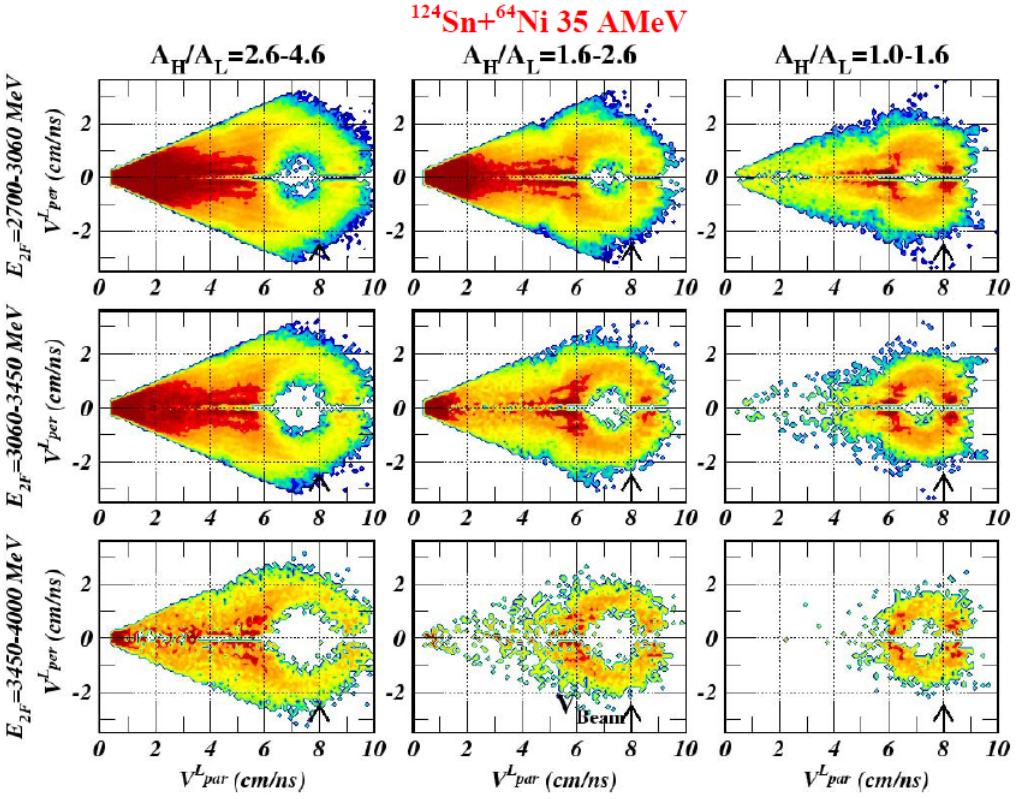

Figure 1.9: V_{par} versus V_{per} Galilean-invariant plots for Light fragments produced in the $^{124}Sn+^{64}Ni$ reaction for three ranges of mass asymmetry A_H/A_L (columns) and for three ranges of the total kinetic energy $E_{2F} = E_H + E_L$ (rows) [30].

(lower right panel of fig. 1.9), Light fragments distribution is forward-backward symmetric, so, in this case Light fragments have equal probability to be emitted forward or backward in the reference frame of PLF* source. This is the statistical fission scenario in which the nucleus is supposed to be completely equilibrated in all its degrees of freedom. Increasing the mass asymmetry of the splitting or the violence of collision also a non-equilibrated contribution is observed. In this case, the population of the Coulomb ring is no longer forward-backward symmetric because Light fragments have the tendency to populate the low-velocity side of the Coulomb ring. This means that they are backward emitted in the PLF* reference frame, that is, toward the TLF*. The observed forward-backward asymmetry indicates that PLF splitting has to be very fast (in comparison to the time scale involved in statistical fission scenario) and it's considered the main signature of the Dynamical Fission. In order to estimate the weight of the two components, dynamical and statistical, the $cos(\theta_{prox})$ distributions were calculated, where θ_{prox} (fig. 1.10) is the "proximity angle", i.e. the angle between the break-up or fission axis

$$\vec{v}_{FIS} = \vec{v}_H - \vec{v}_L, \tag{1.1}$$

oriented from the light L to the heavy fragment H, and the recoil velocity in the center of mass of the PLF (V_{PLF}) reconstructed with the two fission fragments

$$\vec{v}_{PLF} = \frac{A_H \cdot \vec{v}_H + A_L \cdot \vec{v}_L}{A_H + A_L} \tag{1.2}$$

(in CM reference frame). The $cos(\theta_{prox})$ distributions have been evaluated for different

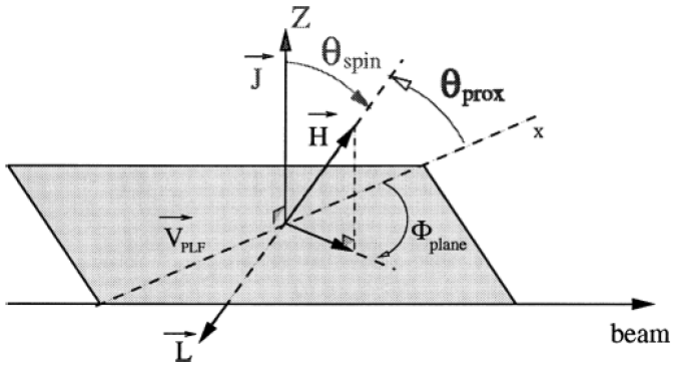

Figure 1.10: Definition of θ_{prox} angle. It's the angle between break-up axis, oriented from the light L to the heavy fragment H, and the recoil velocity in the center of mass of the PLF (V_{PLF}) reconstructed with the two fission fragments.

mass asymmetry and energy dissipation (fig. 1.11). Specifically, in the case of a statistical fission, in which all directions are allowed, a symmetrical distribution with respect to $cos(\theta_{prox}) = 0$ is expected (as the one observed in lower right panel of fig. 1.11). Instead,

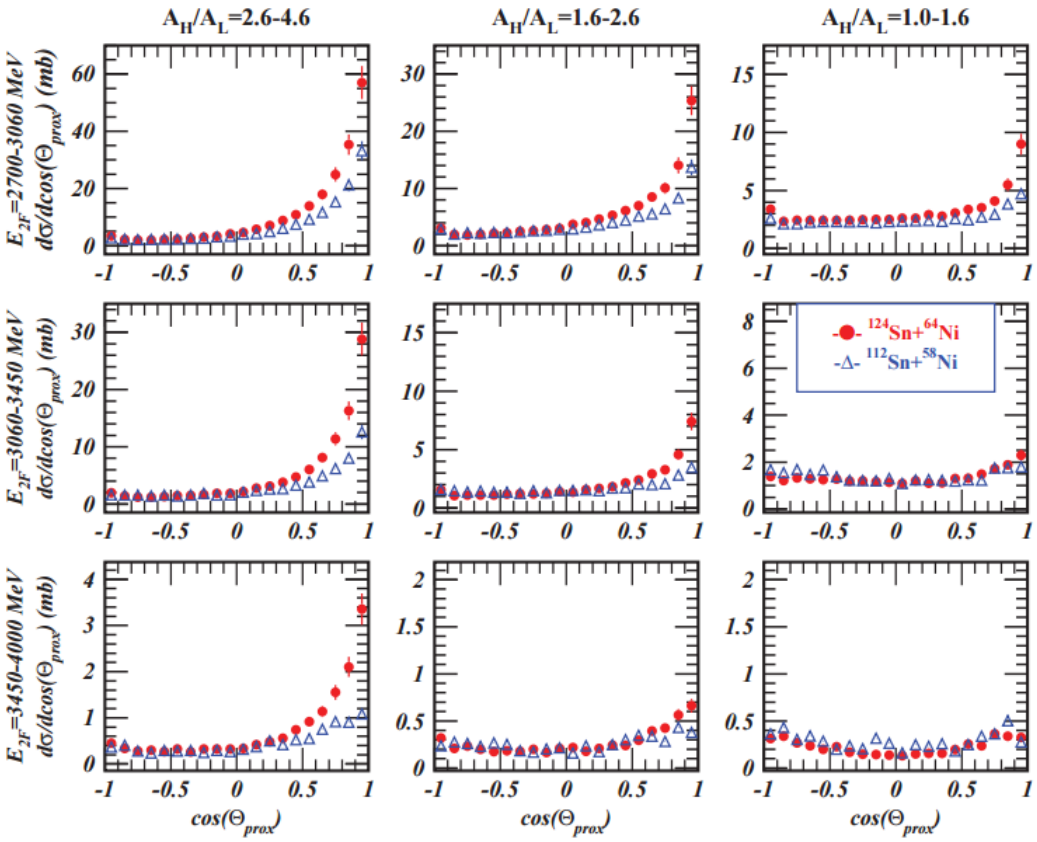

Figure 1.11: $cos(\theta_{prox})$ angular distributions of fission-like fragments for $^{124}Sn(35\ AMeV)+^{64}Ni$ (red cicles) and $^{112}Sn(35\ AMeV)+^{58}Ni$ (blu triangles) reactions. These distribution have been evaluated for different ranges of mass asymmetry A_H/A_L (columns) and different ranges of the total kinetic energy $E_{2F} = E_H + E_L$ (rows) [30].

in the case of dynamical fission the distributions clearly show a peak at $cos(\theta_{prox}) = +1$, that becomes more important with increasing energy dissipation (lower E_{2F}) or mass asymmetry (bigger A_H/A_L). This peak corresponds to a break-up aligned with the PLF recoil axis, with the Heavy fragment faster than Light one. This latter is preferentially located between the Heavy fragment and the TLF; no corresponding peak at $cos(\theta_{prox}) = -1$ is observed. Thus, the $cos(\theta_{prox})$ distributions can be considered as the sum of two component: the first one associated to Statistical Fission (symmetrical with respect to $cos(\theta_{prox}) = 0$) and the second one related to Dynamical Fission (peaked at $cos(\theta_{prox}) = +1$). In order to disentangle these two contributions, a symmetrization around $cos(\theta_{prox}) = 0$ of the backward part of the distribution ($cos(\theta_{prox}) < 0$) was done; in this way, supposing that this part is not influenced by Dynamical Fission, the relative weight of statistical component is obtained. Then, the Dynamical contribution is determined by subtracting the extrapolated Statistical Fission distribution from the total experimental one (fig. 1.12). In this way the relative contribution of the two components, for each selection, could be

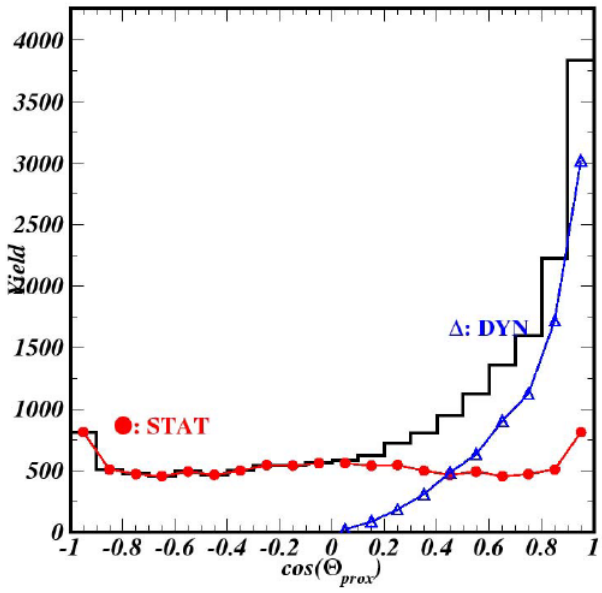

Figure 1.12: A sketch of the procedure used to extrapolate the relative contribution of Dynamical and Statistical Fission in $cos(\theta_{prox})$ distribution. Statistical component (red circles) is obtained doing a symmetrization around $cos(\theta_{prox}) = 0$ of the backward part of the distribution ($cos(\theta_{prox}) < 0$). Instead, Dynamical contribution (blu triangles) is determined by subtracting the extrapolated Statistical Fission distribution from the total experimental one (black line).

estimated:

$$DYN = \frac{N_{Forw} - N_{Back}}{N_{tot}}, \quad STAT = \frac{2 * N_{Back}}{N_{Tot}}, \quad N_{Tot} = N_{Forw} + N_{Back}; \tag{1.3}$$

where, N_{Forw} are counts of the distribution with $cos(\theta_{prox}) > 0$ while N_{Back} are counts of the distribution with $cos(\theta_{prox}) < 0$. In tab. 1.1 the percentages associated to the Dynamical component mechanism for the two systems studied during the REVERSE ($^{124}Sn + ^{64}Ni$ (red values) and $^{112}Sn + ^{58}Ni$ (blue values)) experiment are presented.

Another important angle is the Φ_{plane} angle, defined as the angle between the fission

DYN (%)	^{124}Sn+^{64}Ni ; ^{112}Sn+^{58}Ni		
	A_H/A_L		
E_{2F}(MeV)	2.6-4.6	1.6-2.6	1.6-1.0
2700-3060	75.8 ; 67.3	59.0 ; 45.8	24.1 ; 15.8
3060-3450	71.7 ; 54.6	44.4 ; 21.5	10.7 ; <5.
3450-4000	59.7 ; 40.5	32.8 ; 17.4	<5 ; <5.

Table 1.1: Percentage associated to the Dynamical component mechanism for the systems studied during the REVERSE experiment ($^{124}Sn + ^{64}Ni$ (red values) and $^{112}Sn + ^{58}Ni$ (blue values)). These distribution have been evaluated for ring 1 for different ranges of mass asymmetry A_H/A_L (columns) and different ranges of the total kinetic energy $E_{2F} = E_H + E_L$ (rows) [31].

axis projected on the reaction plane and the recoil velocity of the PLF (fig. 1.13). To

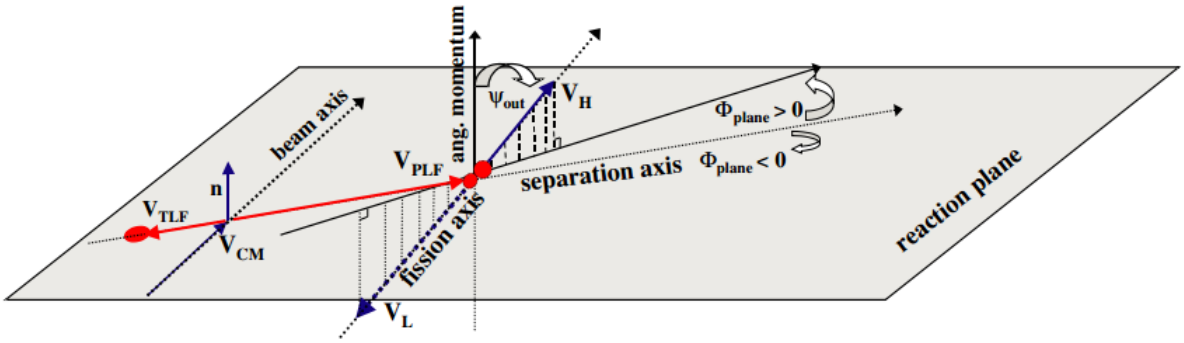

Figure 1.13: Diagram indicating the definiton of the in-plane (Φ_{plane}) and out-of-plane (Ψ_{out}) angles. The orientation of fission axis is given by the heavier fission fragments velocity; $\vec{n}$ is the unit orthogonal vector oriented with respect to the reaction plane.

better understand this angular notation, it's important to introduce the separation axis $\vec{n}_{sep}$, that is parallel and concordant with the PLF-TLF relative velocity:

$$\vec{n}_{sep} = \frac{\vec{v}_{PLF} - \vec{v}_{TLF}}{|\vec{v}_{PLF} - \vec{v}_{TLF}|}, \tag{1.4}$$

where $\vec{v}_{PLF}$, reconstructed from the two selected fragments (Heavy and Light fragments), is given by the formula 1.2. The TLF velocity (if not detected) can be recon-

structed from PLF velocity applying momentum conservation law and it's equal to:

$$\vec{v}_{TLF} = \frac{\vec{p}_{beam} - \vec{p}_{proj}}{A_{targ}}, \tag{1.5}$$

where $\vec{p}_{proj}$ is the momentum of a projectile-like having the mass of projectile, $\vec{p}_{beam}$ is the beam momentum in laboratory reference frame and A_{targ} is the target mass. Then, the reaction plane is defined by the vector orthogonal to both beam axis ($\vec{n}_{Beam}$) and separation axis ($\vec{n}_{sep}$); its normal direction is given by the following cross product:

$$\vec{n} = \frac{\vec{n}_{sep} \times \vec{n}_{Beam}}{|\vec{n}_{sep} \times \vec{n}_{Beam}|}. \tag{1.6}$$

Considering figure 1.13, the out-of-plane angle (Ψ_{out}) specifies the deflection of the fission axis with respect to the normal direction $\vec{n}$ (polar axis), while the in-plane angle Φ_{plane} is the angle between the projection of the fission axis $\vec{v}_{FIS}$ (eq. 1.1) onto the reaction plane and the separation axis $\vec{n}_{sep}$. Specifically, following the convention introduced in ref. [9], Φ_{plane} will be considered positive when both $\vec{n}_{sep}$ x $\vec{v}_{FIS}$ and $\vec{n}$ point in the same half-space; positive Φ_{plane} values mean that the Heavy fragment is deflected toward the beam direction.

The advantage of this angular representation is the elimination of spin effects in angular distributions. In figure 1.14 the "in plane" angular distributions of the PLF break-up fragments for $^{124}Sn+^{64}Ni$ and $^{112}Sn+^{58}Ni$ reactions are shown [2]. For both the investigated systems ($^{124}Sn+^{64}Ni$ and $^{112}Sn+^{58}Ni$), it's possible to see flat angular distributions typical of equilibrated fission for symmetric splitting and low energy dissipation. In fact, the slow equilibrated fission of PLF should result in a flat in-plane distribution [9] because the memory of the entrance-channel direction is lost after a many PLF rotations. However, with increasing mass asymmetry and collision inelasticity, it's possible to observe the rise of the forward-peaked component, with maxima located close to 0^o (related to Dynamical fission), superimposed on the flat statistical distribution. This indicates that the light complementary fragment is emitted backward in the PLF reference frame toward the TLF (aligned break-up). In tables 1.2 and 1.3, dynamical fission contribution (in mb) to fission-like fragments angular cross section of fig. 1.14 for $^{124}Sn+^{64}Ni$ and $^{112}Sn+^{58}Ni$ systems are presented. The values, calculated for different ranges of mass asymmetry A_H/A_L (columns) and different ranges of the total kinetic energy $E_{2F} = E_H + E_L$ (rows), were obtained using the method reported in Sec. III.c.1 of ref. [10]. In the same way, equilibrated contribution to cross section was estimated (tables 1.4 and 1.5). In all cases, the statistical contribution to cross section is almost the same for the two systems. Instead, the dynamical contribution is greater in the neutron rich system and it increases with the mass asymmetry and the violence of the collision.

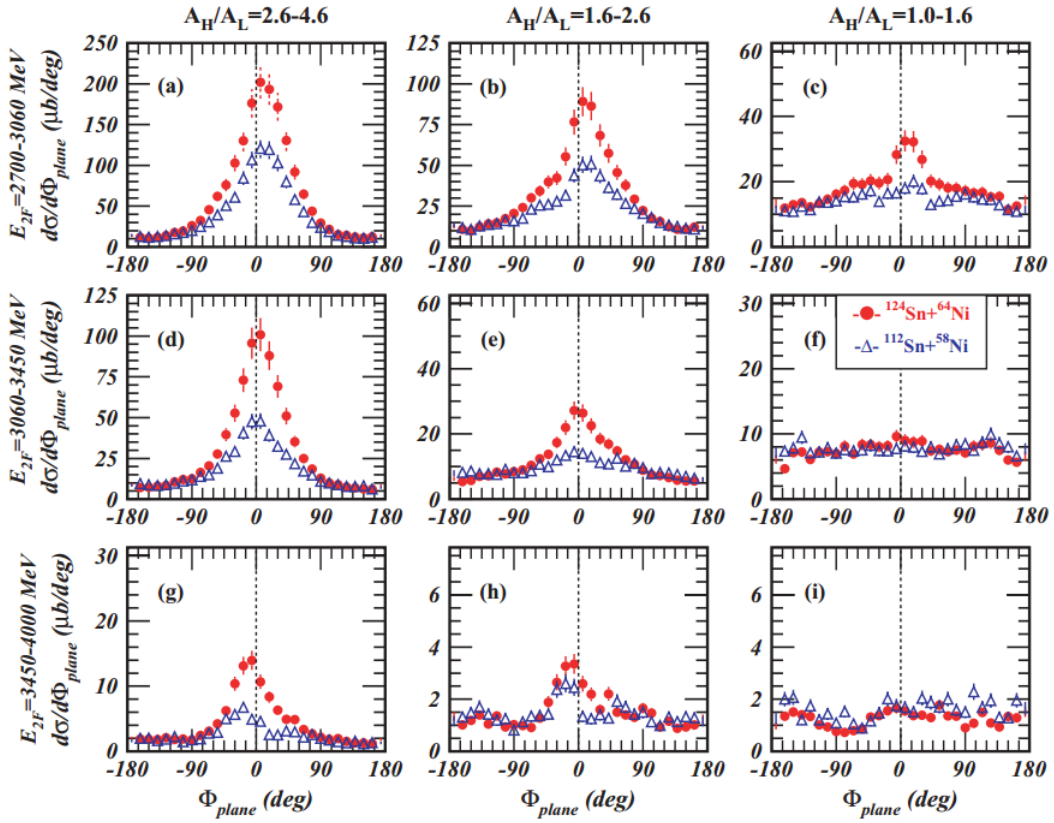

Figure 1.14: Comparison of Φ_{plane} fission-like fragments angular distributions for $^{124}Sn + ^{64}Ni$ (red values) and $^{112}Sn + ^{58}Ni$ (blue values) reactions at 35 $AMeV$, for different ranges of mass asymmetry A_H/A_L (columns) and different ranges of the total kinetic energy $E_{2F} = E_H + E_L$ (rows). $\Phi_{plane} = 0^o$ indicates that heavier of the two fragments is forward emitted in the PLF reference system, strictly along PLF flight direction in the laboratory system [2].

E_{2F} (MeV)	A_H/A_L		
	2.6–4.6	1.6–2.6	1.0–1.6
2700–3060	15.9 ± 1.6	6.5 ± 0.6	1.4 ± 0.1
3060–3450	7.2 ± 0.7	1.7 ± 0.2	0.2 ± 0.3
3450–4000	0.8 ± 0.1	0.1 ± 0.1	<0.1

Table 1.2: Cross section σ_{dyn} in mb of dynamical fission component in the $^{124}Sn + ^{64}Ni$ reaction at 35 $AMeV$ [2].

E_{2F} (MeV)	A_H/A_L		
	2.6–4.6	1.6–2.6	1.0–1.6
2700–3060	9.2 ± 0.9	3.3 ± 0.3	0.6 ± 0.1
3060–3450	3.3 ± 0.3	0.6 ± 0.1	<0.1
3450–4000	0.3 ± 0.1	<0.1	<1

Table 1.3: Cross section σ_{dyn} in mb of dynamical fission component in the $^{112}Sn + ^{58}Ni$ reaction at 35 $AMeV$ [2].

E_{2F} (MeV)	A_H/A_L		
	2.6–4.6	1.6–2.6	1.0–1.6
2700–3060	5.4 ± 0.5	4.9 ± 0.5	5.1 ± 0.5
3060–3450	3.1 ± 0.3	2.4 ± 0.3	2.5 ± 0.3
3450–4000	0.6 ± 0.1	0.4 ± 0.1	0.5 ± 0.1

Table 1.4: Cross section σ_{equil} in mb of equilibrium fission component in the $^{124}Sn + ^{64}Ni$ reaction at 35 $AMeV$ [2].

E_{2F} (MeV)	A_H/A_L		
	2.6–4.6	1.6–2.6	1.0–1.6
2700–3060	5.1 ± 0.5	4.9 ± 0.5	4.6 ± 0.5
3060–3450	3.1 ± 0.3	2.8 ± 0.3	2.8 ± 0.3
3450–4000	0.6 ± 0.1	0.5 ± 0.1	0.6 ± 0.1

Table 1.5: Cross section σ_{equil} in mb of equilibrium fission component in the $^{112}Sn + ^{58}Ni$ reaction at 35 $AMeV$ [2].

The $^{124}Sn + ^{64}Ni$ and $^{112}Sn + ^{58}Ni$ reactions were also analyzed in [3]. In this work, in which the IMFs production cross sections in semi-peripheral reactions were evaluated for dynamical and statistical emission, the previous analysis of [2] was extended by enlarging by about a factor 2 the impact parameter window of the collision toward more dissipative collisions, evaluating cross sections of the observed IMFs from atomic number $Z = 3$ up to $Z = 22$. In this case, the events were selected by requiring a PLF residue having atomic number $Z >\sim 20$ and parallel velocity with respect to the beam axis (in laboratory reference frame) $V_{par} >\sim 6$ cm/ns. In most of the selected events, that have reduced impact parameter $b_{red} > 0.4$, PLF has $Z \sim 45$ and $V_{par} \sim 7.5$ cm/ns, slightly below the beam velocity of ~ 8 cm/ns.

In figure 1.15 the probability (panel a)) and the cross section (panel b)) associated to the multiplicity of IMF detected in coincidence with the PLF for the two reactions ($^{124}Sn + ^{64}Ni$ and $^{112}Sn + ^{58}Ni$) are shown (TLF residues have been excluded following the method described in Sec. II of [3]). Specifically, events with IMF multiplicity

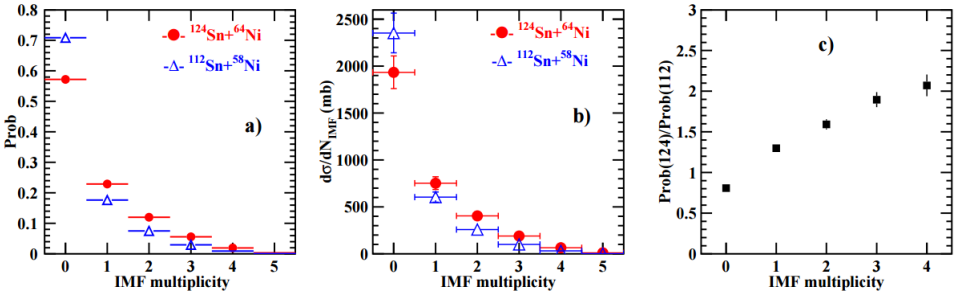

Figure 1.15: Probality associated to multiplicity of IMF detected in coincidence with the PLF for the two reactions ($^{124}Sn + ^{64}Ni$ (full circles) and $^{112}Sn + ^{58}Ni$ (empty triangles)), normalized to the number of selected events, (panel a)); cross section associated to IMF multiplicity for the same systems (panel b)); ratio of the probabilies given in panel a) (panel c)) [3]. All the plots have been obtained by taking into account the detection efficiency of the experimental apparatus, using the HIPSE code [32] as event generator and a software replica of CHIMERA multi-detector [33].

equal to zero correspond to "binary events" in which, in addition to PLF-TLF binary partners, only Light Charged Particles (LCP) ($Z \leq 2$) have been produced. These events are more probable in the neutron poor systems than in the neutron rich one.
Instead, in panel c) of figure 1.15 the ratio of the two probabilities (given in panel a)) as a function of IMF multiplicity is presented. This panels clearly shows that the relative probability ($\frac{neutron\ rich}{neutron\ poor}$) increases with the IMF multiplicity. Thus, in order to investigate the origin of the difference in IMF emission probability between the two systems, the contribution of both statistical and dynamical emission mechanisms were evaluated, limiting the study to the class of events with IMF multiplicity equal to one [3]. In particular, in figure 1.16 $V_{par} - V_{per}$ Galilean-invariant cross-section plots for PLF (panel a)) and one IMF of Z=10 (panel b)) for $^{124}Sn + ^{64}Ni$ are shown. Considering $V_{par} - V_{per}$ plot of IMF,

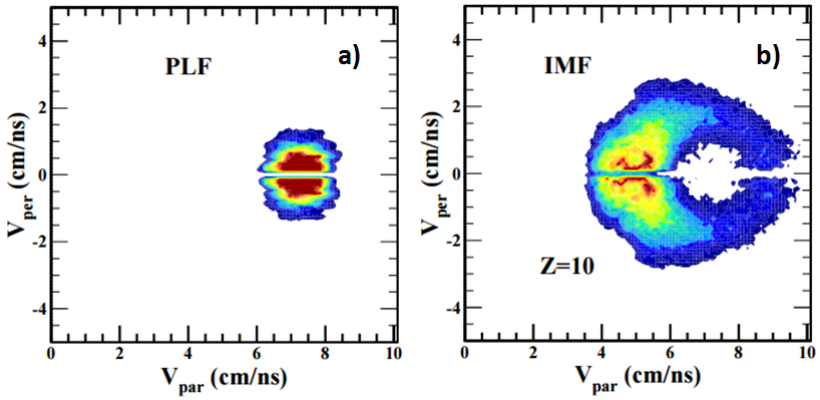

Figure 1.16: $V_{par} - V_{per}$ Galilean-invariant cross-section plots for PLF (panel a)) and one IMF of Z=10 (panel b)) for $^{124}Sn + ^{64}Ni$ reaction at 35 $AMeV$ [3].

it's possible to see that IMF populate preferentially the low velocity side of the Coulomb ring, which means that they are backward emitted in the primary PLF* (PLF+IMF center of mass) reference system; this is typical of dinamical emission. Moreover, a structure reminiscent of Coulomb ring, centred around the centroid of PLF parallel velocity is also present (statistical decay). To estimate the weight of the two components, also here the $cos(\theta_{prox})$ distributions have been calculated. In particular, in figure 1.17, the dynamical (panel a)) and statistical (panel b)) contributions to the cross section as a function of IMF atomic number for the two systems ($^{124}Sn + ^{64}Ni$ and $^{112}Sn + ^{58}Ni$) are shown. It results that, while statistical emission has the same probability in both systems, the dynamical fission probability is enhanced up to a factor 1.5-2 in the neutron rich system [3]. The origin of this enhancement could be related to the entrance channel Isospin difference between the two systems; but, also the different sizes of studied systems can play an important role.

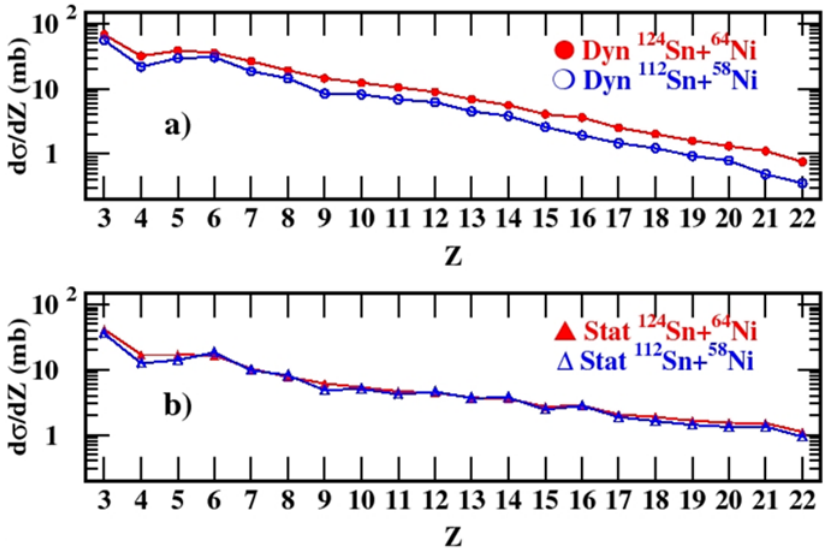

Figure 1.17: Cross section associated to dynamical (upper panel) and statistical (lower panel) emission mechanism for neutron rich system $^{124}Sn(35\ AMeV)+^{64}Ni$ (full symbols) and neutron poor one $^{112}Sn(35\ AMeV)+^{58}Ni$ (empty symbols) [3].

1.3 Theoretical models

These studies have also motivated calculations in the framework of CoMD-II model [5] and BNV codes [34]. These models allow to describe the main features of dynamical emission and neck fragmentation.

1.3.1 CoMD-II model

The Constrained Molecular Dynamics-II (CoMD-II) model is a molecular dynamics model [5, 35] which allows to reproduce some characteristic features of the dynamical fission process. Its main feature is a self-consistent N-body approach that overcomes the main problems typically related to semiclassical many-body dynamics by solving the equations of motion using constraining procedures to satisfy the Pauli principle (event by event) and to respect the conservation rule regarding total angular momentum. This last feature plays a crucial role in producing dynamical processes with different time characteristics. In particular, the $^{124}Sn(35\ AMeV)+^{64}Ni$ system was investigated generating several tens of thousands of events with the CoMD-II model up to a maximum time of 800 fm/c and for impact parameters b ranging from 0 to $0.85b_{max}$ ($b_{max} \approx 10.5\ fm$). Comparing the results of CoMD-II calculations with experimental data for the distribution of fragments as a function of their atomic number Z and their longitudinal velocity, it's possible to see that these quantities are very similar (fig. 1.18). Specifically, in the upper panel of fig. 1.18 the experimental charges and velocities of the three biggest fragments with $Z \geq 3$ for $^{124}Sn+^{64}$

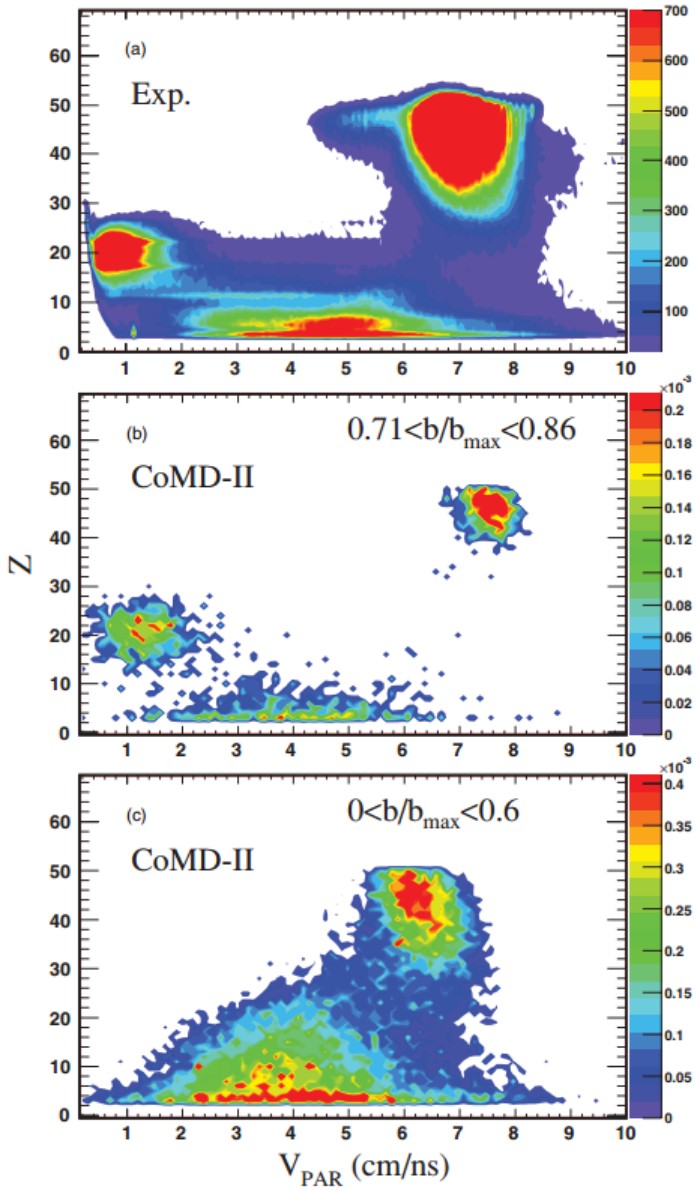

Figure 1.18: Experimental charge Z vs parallel velocity V_{par} plot for the three biggest fragments with $Z \geq 3$ for $^{124}Sn + ^{64}Ni$ system (upper panel). The analogous plots evaluated with the CoMD-II model for $0.71 < b/b_{max} < 0.86$ (panel b)) and for $0 < b/b_{max} < 0.6$ (panel c)) [5].

Ni system is presented; while, the panels b) and c) show the same distributions obtained with CoMd-II calculations for $0.71 < b/b_{max} < 0.86$ and for $0 < b/b_{max} < 0.6$ respectively. Calculations indicate that the shape of such a correlation plot sensitively depends on the selected b window. In the case of smaller impact parameters (panel c) of fig. 1.18), the PLF fragment has a lower velocity, while target residue shows the charge considerably reduced and velocity increased. Thus, there is the tendency of TLF to populate a region that is usually filled by the IMFs of intermediate velocity produced by more peripheral reactions. In this case the so-called *neck formation process* can merge with the TLF multi-break-up. Moreover, CoMD-II calculations can reproduce the reduced relative velocity of the IMF with respect to the TLF fragment (V_{red}^{IT}) as a function of its reduced velocity with respect to the PLF (V_{red}^{IP}) (fig. 1.19)(V_{red}^{IT} and V_{red}^{IP} represent the relative velocities of IMF with respect to TLF and PLF divided by the corresponding value obtained from the Viola systematics). In fig. 1.19 the comparison between experimental and theoretical

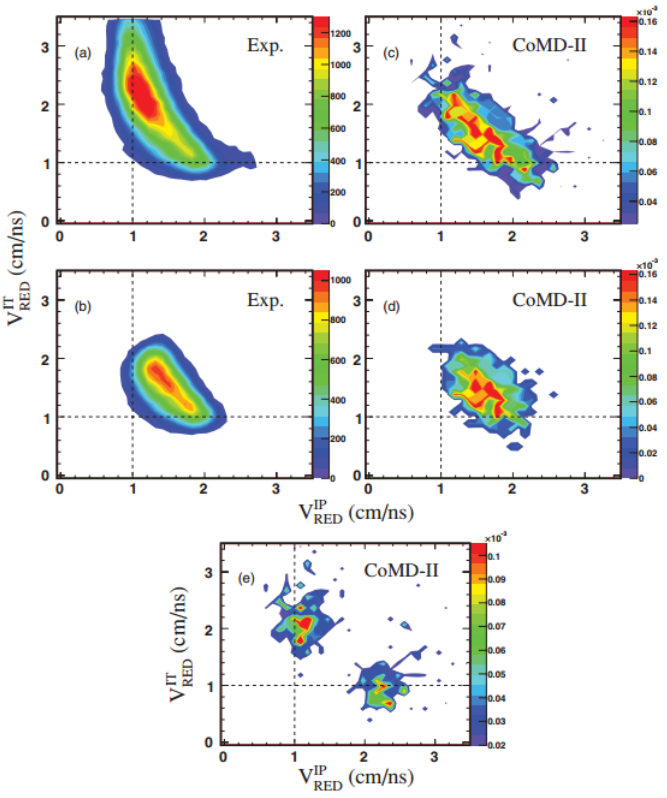

Figure 1.19: In panels a) and b) the experimental $V_{red}^{IT}-V_{red}^{IP}$ plots for ternary events are presented (in panel b) only IMFs having a parallel velocity range of 2.5-5 cm/ns have been considered). Panels c) and d) show the analogous plots obtained from CoMD-II calculations. The calculation results obtained for IMFs velocities outside the range 2.5-5 cm/ns are shown in panel e) [5].

data is shown. Specifically, panel d) shows that the experimental correlations close to the mid-rapidity IMF velocities are well reproduced from CoMD-II calculation. However,

perhaps due to the finite time of the calculations, the greater yield seen in panel a) along the $V_{red}^{IP} = 1$ axis (corresponding to a longer time scale toward the PLF fission) is not reproduced in panel c). Nevertheless, the region along the $V_{red}^{IP} = 1$ axis is not empty, as it's possible to see in panel e) of fig. 1.19 where the calculated $V_{red}^{IT} - V_{red}^{IP}$ plot for the IMF parallel velocities outside of the range 2.5-5 cm/ns is shown. Specifically, the simulated events of this region include the PLF fission evolving with an average decay time of about 300 fm/c and producing an IMF with an average mass of about 35 units. About that, fig. 1.20 shows time evolution of the average mass numbers of the three biggest fragments according to the CoMD-II model for ternary (full dots) and dynamical fission events (open circles). This evolution is characterized by a "time delay" of about 130 fm/c. The TLF

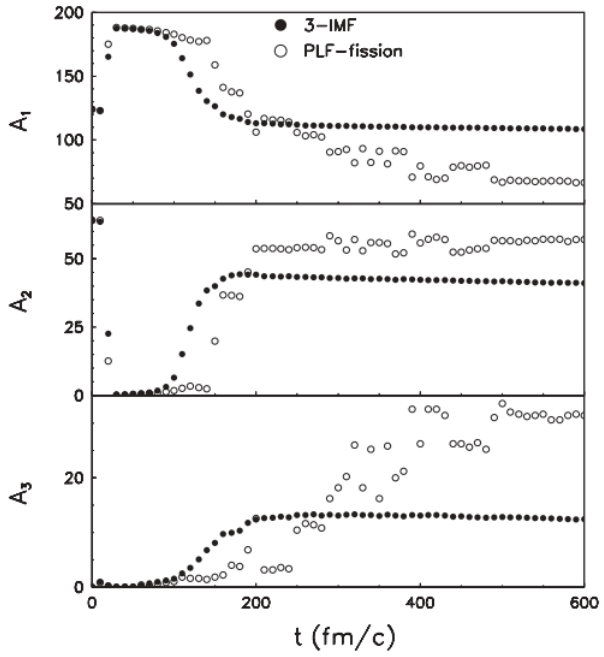

Figure 1.20: Time evolution of the average mass numbers of the three biggest fragments according to the CoMD-II model for ternary (full dots) and dynamical fission event (open circles). A_1, A_2, A_3 indicate PLF, TLF and IMF respectively [5].

(A_2) is formed after about 50 fm/c and the PLF (A_1) undergoes a binary splitting in the subsequent time interval of about 300 fm/c. According to this study and also to the result obtained in Ref.[10], in ternary events, for moderate asymmetry between the masses of PLF and IMF produced at mid-rapidity, a large contribution is given from a dynamical sequential breaking of the hot PLF. These events also show a Φ_{plane} distribution strongly peaked at forward angle. In particular, the average value of Φ_{plane} ($\overline{\Phi_{plane}}$) allows to have information related to the characteristic time of the process. In fig. 1.21 a comparison between the experimental Φ_{plane} distribution for $^{124}Sn + ^{64}Ni$ system (open circles) and calculated (full circles) Φ_{plane} distribution is reported. Model calculations

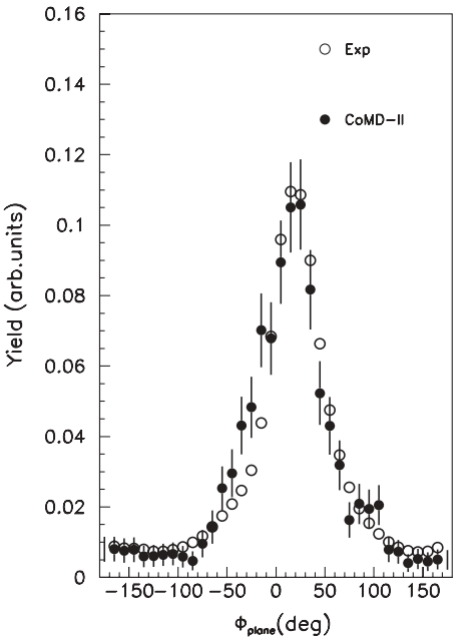

Figure 1.21: A comparison between the experimental (open circles) and calculated (full circles) Φ_{plane} distribution for events with $A_H/A_L < 5$ and $V_{par}^L > 3\ cm/ns$ [5].

reproduce the experimental Φ_{plane} distribution well, including the background associated with the primary PLF splitting processes with longer emission times; this almost flat contribution is related to the statistical emission. CoMD-II calculations was also used to investigate the difference in dynamical fission strenght between the neutron rich and the neutron poor system seen in the REVERSE experiment. As said previously, during this process the PLF breaks in two main fragments, A_H (the heavy one) and A_L (the light one), whose ratio is named A_{HL}. Experimental data obtained during the REVERSE experiment show that the yield of processes related to the dynamical PLF fission is higher for the neutron-rich system with respect to the case of the neutron-poor one. This difference could be related to the entrance channel Isospin difference between the two systems; but, it could also be due to their different sizes. In order to disentangle these two effects, the A_{HL} (A_H/A_L) distributions predicted by CoMD-II model for the two systems ($^{124}Sn(35\ AMeV)+^{64}Ni$ (red line) and $^{112}Sn(35AMeV)+^{58}Ni$ (blu line)) were compared with those of the $^{124}Cs(35\ AMeV)+^{64}Ga$ system [4]. This system has the same mass of neutron-rich system ($^{124}Sn+^{64}Ni$) and N/Z ratio equal to the neutron-poor one ($^{112}Sn+^{58}Ni$). As it's possible to see in fig. 1.22, where the A_{HL} distributions for the three systems are shown, the $^{124}Cs\ +^{64}Ga$ system (light blue line) present a A_{HL} distribution similar to the one measured for the neutron rich reaction ($^{124}Sn\ +^{64}Ni$). So, CoMD-II model suggests that the origin of the observed difference is related to the entrance channel mass difference of the two systems.

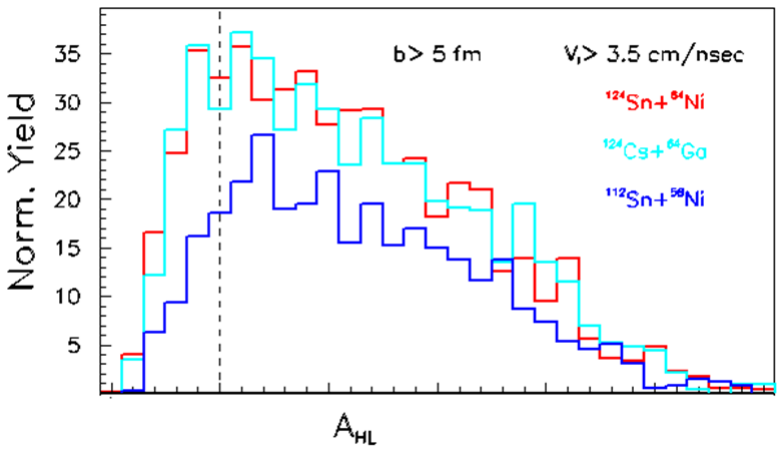

Figure 1.22: A_{HL} distributions for three systems: $^{124}Sn +^{64} Ni$ (red line), $^{112}Sn +^{58} Ni$ (blu line) and $^{124}Cs +^{64} Ga$ (light blue line) [4].

1.3.2 BNV stochastic transport model

The Boltzmann-Nordheim-Vlasov stochastic transport model is a stochastic mean field microscopic apporach that describes via a transport equation the time evolution of the nucleon one-body distribution function in phase space $f(\vec{r}, \vec{p}, t)$ [36, 37]. It provides a generally good average description of the dissipative mechanisms occurring all along the interaction between the two colliding nuclei. According to entrance channel properties, different out-coming channels, from the formation of only one composite nuclear source (in the case of central collisions) up to deep-inelastic-like processes (in the case of peripheral reactions), are observed [36, 37]. In particular, Baran et al. [34] investigated fast fragments production mechanism from semi-central to peripheral collisions ($b_{red} = b/b_{max} \geq 0.37$) for the $^{124}Sn(35AMeV)+^{64}Ni$ and $^{112}Sn(35AMeV)+^{58}Ni$ systems. They used a BNV [34] approach to mean field with a stochastic fluctuating term that takes into account dynamics of fluctuations. The transport equations are solved following a test particle on lattice. In the collision term, a parametrization of free nucleon-nucleon (NN) cross section is used, with energy and angular dependence. Moreover, the isospin effects on the nucleon cross section and Pauli blocking are consistently evaluated. Events observed in the calculation were divided in three classes:

1. binary events with excited TLF* and PLF* that, having small deformation, remain so for long times. Their sequential decay can be described by statistical models;

2. binary events in which especially PLF* have large quadrupole or octupole deformation;

3. ternary events, in which, in addition to PLF* and TLF* generally less deformed,

there is an IMF directly emitted in less than $\sim 250\ fm/c$ from the reaction beginning.

Fig. 1.23 shows the scatter plot of freeze-out quadrupole versus octupole moment for all fragments of events of the first two classes for different impact parameter values. In this figure it's possible to distinguish two branches that can be associated to deformed PLF* (left branch) and TLF* (right branch). The large dynamically induced deforma-

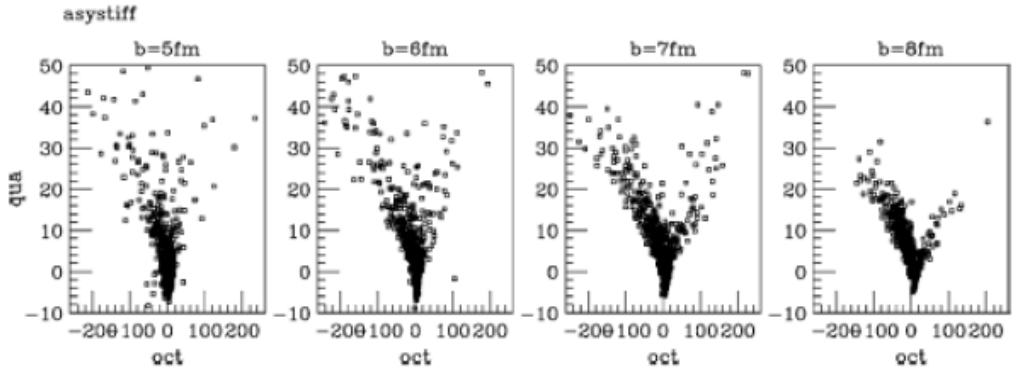

Figure 1.23: Scatter plot of freeze-out quadrupole versus octupole moment for all fragments of the events of the classes (1) and (2) for different impact parameter values [34].

tions can drive especially the PLF* towards a fast asymmetric fission. The corresponding signs suggest pear-shaped fragments oriented with the smaller deformation towards the separation point. The last two classes of events can contribute to the "dynamical" production of IMFs. Instead, in fig. 1.24 typical evolution of the density contour plot for a ternary event (event of class (3)) at $b = 6\ fm$ for the system $^{124}Sn(35AMeV)+^{64}Ni$ is shown. Initially, for the first 20-60 fm/c the two participants deeply interact and at this time some compression takes place. The system heats up and a relative expansion follows. Despite its compact form, the system still behaves as a "two-center object" with an effective superimposed separate motion of the PLF and TLF pre-fragments. This motion induces the formation of a neck-like structure that, between 40 fm/c and 140-160 fm/c, rapidly changes geometry, depending on the impact parameter. After about 150 fm/c, this neck-instability dynamic favors the emission of IMFs. Their production probability depends on the impact parameter, as shown in fig. 1.25; it's maximal (around 25%) for semiperipheral collisions (b=6-7 fm), while it strongly decreases for semicentral (b=4-5 fm) collisions and at larger impact parameter, where this mechanism is suppressed by a less overlapping and a faster separation. Moreover, fig. 1.26 presents the asymptotic fragment velocity distributions in the laboratory frame for all impact parameters and for all the events (binary (classes (1) and (2)) and ternary (class (3)) events) of the three classes; in this plot "vpar" is the velocity component along the beam direction while "vtran" is the orthogonal part. The IMFs are found in relatively wide midrapidity region, in strong

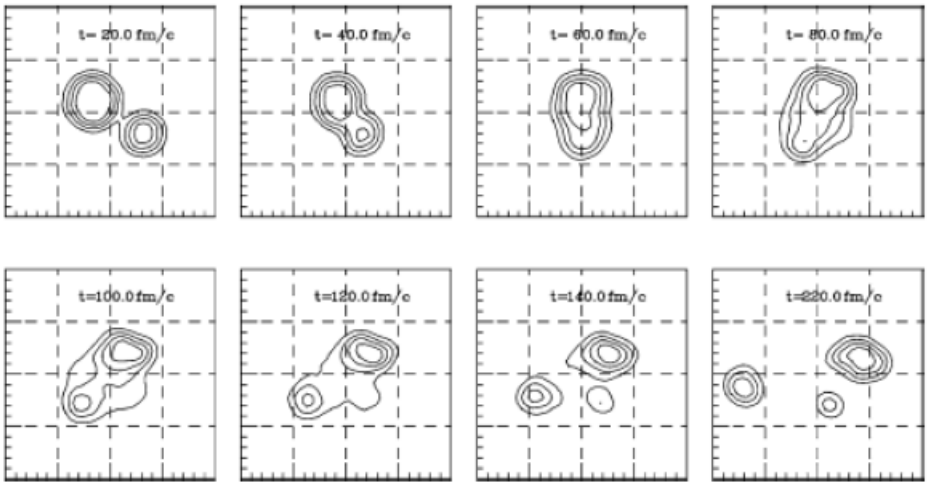

Figure 1.24: Typical evolution of the density contour plot for a ternary event (event of class (3)) at $b = 6\ fm$ for the system $^{124}Sn(35AMeV)+^{64}Ni$ [34].

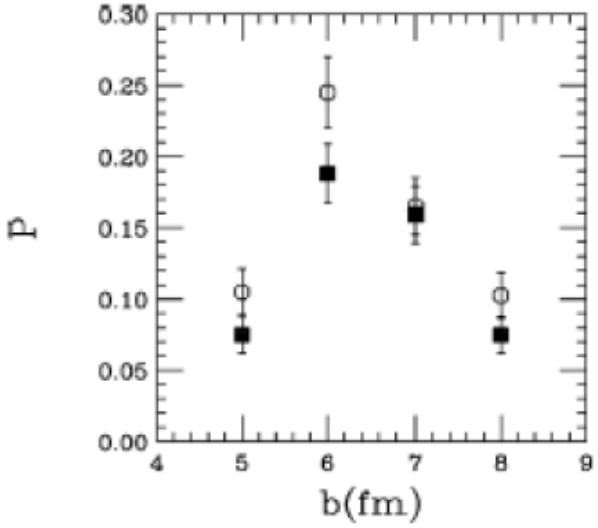

Figure 1.25: The impact parameter dependence of the probability for ternary events in neutron-rich (white circles) and neutron-poor (black squares) reaction [34].

agreement with experimental vpar velocity distribution of fig. 1.2. Finally, in fig. 1.27 the

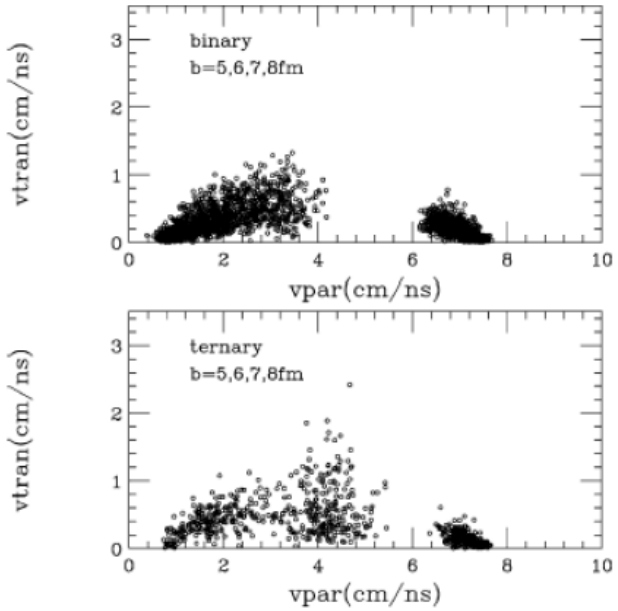

Figure 1.26: The asymptotic fragment velocity distributions in the laboratory frame for all impact parameters and for all fragments observed in binary events (upper panel) and ternary events (bottom panel) [34].

correlation between relative velocities V_{rel}/V_{Viola}(IMF,PLF) (r) and V_{rel}/V_{Viola}(IMF,TLF) (r 1) obtained in BNV simulation for all IMFs is shown. Comparing these results with the experimental relative velocities correlation and V_{par} plots (fig. 1.5 and fig. 1.2), it's possible to see a strong qualitative agreement expecially for lighter IMFs ($Z_{IMFs} = 4, 8$). Also this analysis supports a fast neck break-up mechanism triggering the formation of a light IMF ($Z <\sim 10$), localized in the mid velocity region. Moreover, in BNV simulation, IMFs formation is observed mainly between 140 and 260 fm/c in agreement with the results obtained with the relative correlation method (sect. 1.1). In fact this method demonstrates that light IMFs emission takes place at 40-80 fm/c after the system starts to re-separate that corresponds to about 140-180 fm/c in BNV calculation (in this case re-separation between PLF and TLF takes place around 100 fm/c). The relative correlation method also predicts heavy IMF emission at times of about 120 fm/c or longer after the beginning of reseparation (sect. 1.1). But, unlike the light IMFs, these events are not predicted by BNV calculation; it can't reproduce this delayed mechanism because of a problem of instability with increasing time. However, with the events of class (2) also BNV model supports the idea of a fast neck induced fission in competition with statistical decay of primary fragments.

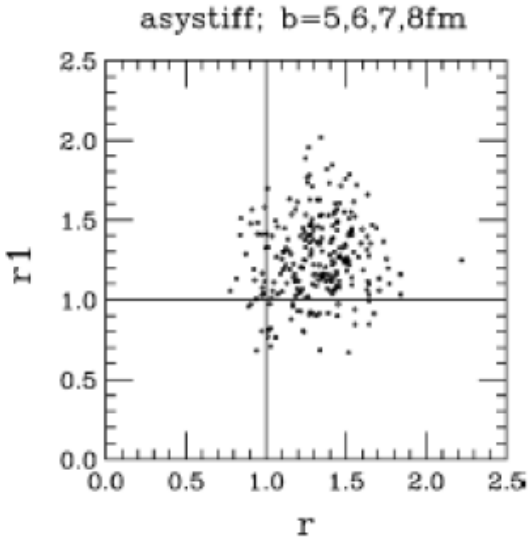

Figure 1.27: Relative velocity correlation plot obtained in BNV simulation for $^{124}Sn(35AMeV)+^{64}Ni$ reaction [34].

1.4 InKiIsSy experiment: open question

The InKiIsSy experiment was carried out at Laboratori Nazionali del Sud in April 2013 in order to disentangle entrance channel isospin effects from the possible dependence of these results upon the initial different mass of the two systems. During this experiment the $^{124}Xe +^{64} Zn$ reaction was studied at 35 $AMeV$ beam energy, it has the same mass of the neutron rich system ($^{124}Sn +^{64} Ni$) and a N/Z ratio close to the value of the neutron poor one ($^{112}Sn +^{58} Ni$). During the InKiIsSy experiment also the $^{124}Xe +^{64} Ni$ system was analyzed, in order to compare two systems ($^{124}Xe +^{64} Zn$ and $^{124}Xe +^{64} Ni$) with same mass and beam but with different N/Z ratio for the target.

Table 1.6: Isospin values of the systems analyzed during the REVERSE ($^{124}Sn +^{64} Ni$ and $^{112}Sn +^{58} Ni$) and the INKIISSY ($^{124}Xe +^{64} Zn$, $^{124}Xe +^{64} Ni$) experiments.

System	N/Z **projectile**	N/Z **target**	N/Z **compound**
$^{124}Sn +^{64} Ni$	1.48	1.29	1.41
$^{124}Xe +^{64} Ni$	1.30	1.29	1.29
$^{124}Xe +^{64} Zn$	1.30	1.13	1.24
$^{112}Sn +^{58} Ni$	1.24	1.07	1.18

In tab.1.6 the value of Isospin of the four systems (REVERSE + InKiIsSy) are reported. This last measurement was performed using the multi-detector CHIMERA coupled for the first time with 4 telescopes of FARCOS array [38].

Chapter 2

Experimental setup

In this second chapter the experimental setup used during the InKiIsSy experiment will be described. This experiment has been performed on April 2013 at the INFN-LNS in Catania by using the 4π CHIMERA multi-detector, coupled to a prototypes of the correlator FARCOS.

2.1 CHIMERA multidetector

CHIMERA (Charged Heavy Ion Mass and Energy Resolving Array) is a multidetector with high granularity and large covering of the total solid angle (94%), designed to study heavy-ion collisions in the Fermi and low energy regimes [15]. It can be schematically described as a set of 1192 detection cells arranged in 35 rings following a cylindrical geometry along the beam axis. The whole apparatus, schematized in fig. 2.1, has a total length of about 4 m and it operates under vacuum. The mechanical structure can be essentially divided into two differently shaped blocks. The forward one, covering polar angles between 1^o and 30^o, is made of 688 modules assembled in 18 rings, grouped in couples, and supported by 9 wheels centred on the beam axis (fig. 2.2). Each wheel is divided into 16, 24, 32, 40 or 48 trapezoidal cells, depending on its polar coordinate, containing each one a detection module, or telescope, that will be described afterwards. The rings of telescopes are placed at different distance from the target: the first ring is placed at a distance of 350 cm, while the last ring is placed at a distance of 100 cm from the target. Thus, placing telescopes at distance that increases with decreasing polar angle, it's possible to obtain a precise measure of time-of-flight also for forward emitted fragments, that are the faster ones, being mainly emitted by the PLF. The second block, instead, is made of 504 modules grouped in 17 rings and covers the remaining angular range, between 30^o and 176^o. These 17 rings are assembled in a sphere of 40 cm in radius as shown in figure 2.3. Specifically, 15 of the 17 rings are segmented into 32 cells while the 2 backward ones are

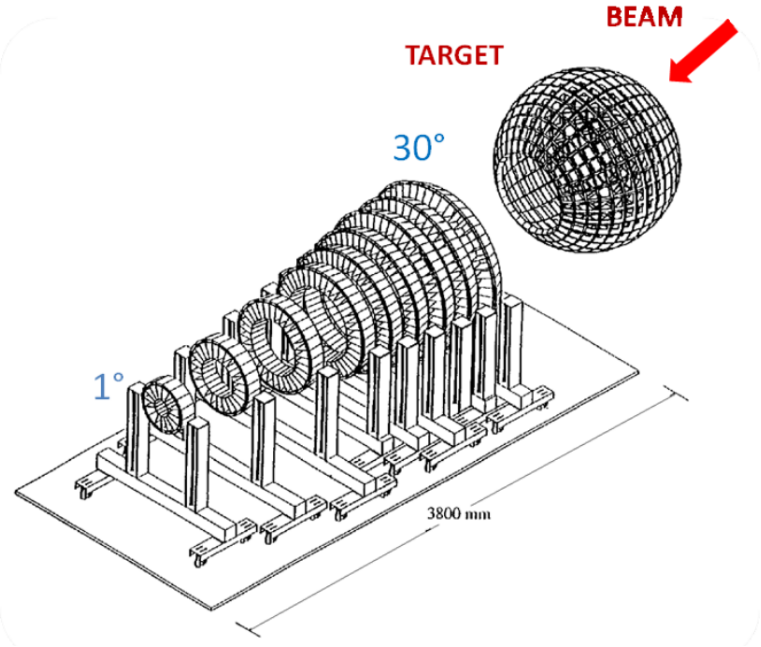

Figure 2.1: Schematic picture of the CHIMERA apparatus.

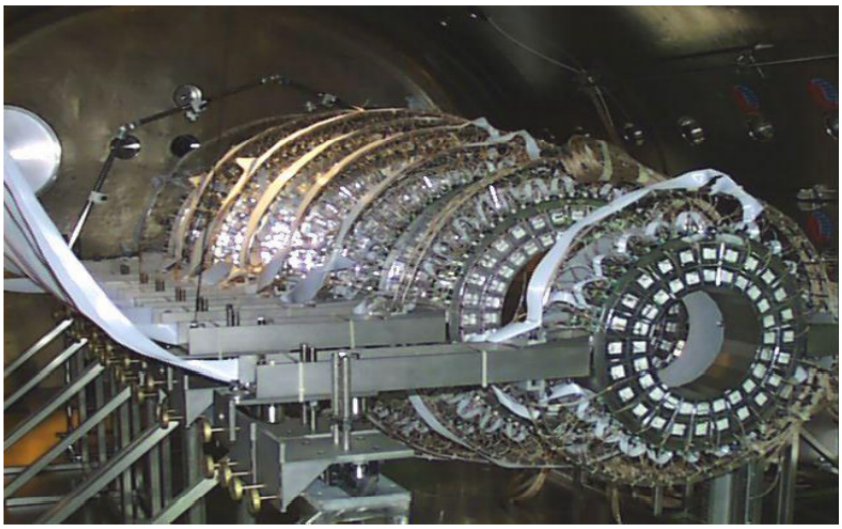

Figure 2.2: A photo of the nine wheels of CHIMERA multidetector.

segmented into 16 and 8 cells respectively. Each module of this spherical structure consists in a steel box containing the Caesium Iodide crystal with the silicon detector placed at the side facing the target. In table 2.1 the main geometrical characteristics of CHIMERA

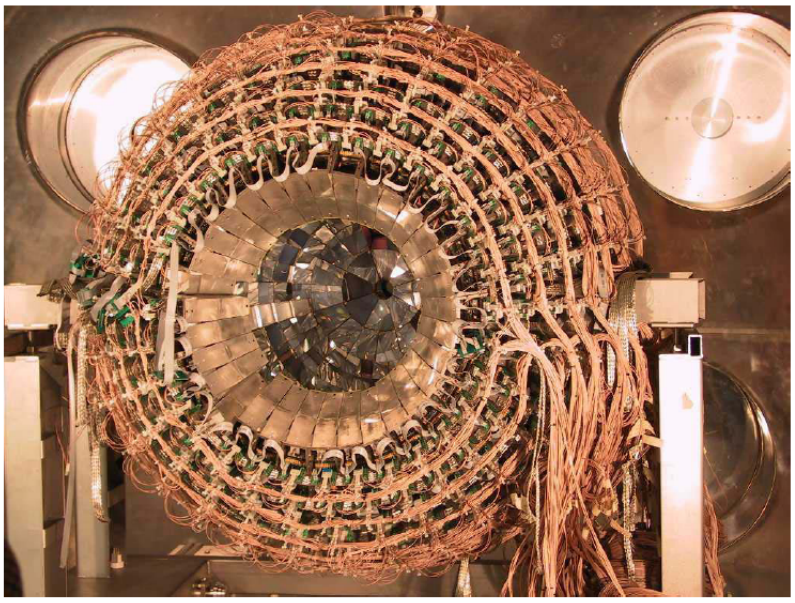

Figure 2.3: A photo of the sphere of CHIMERA multidetector.

array are given. The large number of telescopes and the geometrical configuration give to CHIMERA a high granularity, thus reducing the multi-hit probability, and a high solid angle coverage, about 94% of 4π; these features, in addiction to low energy detection threshold, allow to obtain a complete event recostruction.

2.1.1 The telecopes of CHIMERA array

The basic detection module of CHIMERA array is a telescope composed by two detection stages: a Silicon detector (Si) with a thickness of about 300 μm, followed by a Caesium Iodide Thallium activated scintillation detector (CsI(Tl)) (fig. 2.4), coupled to a photodiode [15]. As well known, silicon is a very widely used material for nuclear physics detectors because of good energy resolution, high density (2.33 g/cm^3), low energy needed to create an electron-hole pair (3.6 eV with respect to 30 eV in gases), fast signal collection (10 ns in 300 μm of thickness) and good time resolution. The silicon detectors used in CHIMERA have a trapezoidal shape and were made by using the planar technology [39]. This tecnique allows to have well defined detector thickness, very sharp active zones, extremely thin (500 $\AA$) and homogeneous junction. Moreover, a 300 $\AA$ aluminium layer covers front and rear face of the silicon slice in order to ensure a good electrical contact. This characteristic slightly decreases the energy resolution because introduces a

Wheels	Ring	Dist. (cm)	Θmin (deg)	Θmax (deg)	Modules	ΔΦ(deg)	Surface (cm^2)	ΔΩ (mSr)/(singlemodule)
1	1 2	350	1.0 1.8	1.8 2.6	16	22.5	16.3 25.6	0.13 0.21
2	3 4	300	2.6 3.6	3.6 4.6	24	15	22.2 29.3	0.25 0.33
3	5 6	250	4.6 5.8	5.8 7.0	32	11.25	23.3 28.6	0.37 0.46
4	7 8	210	7.0 8.5	8.5 10	40	9	24.2 29.1	0.55 0.66
5	9 10	180	10 11.5	11.5 13	40	9	24.8 28.2	0.77 0.87
6	11 12	160	13 14.5	14.5 16	48	7.5	20.8 23.1	0.81 0.90
7	13 14	140	16 18	18 20	48	7.5	26.2 29.1	1.34 1.49
8	15 16	120	20 22	22 24	48	7.5	23.6 25.7	1.64 1.78
9	17 18	100	24 27	27 30.0	48	7.5	29.5 32.7	2.95 3.27
10	19	40	30.0	38.0	32	11.25	24.5	15.33
11	20	40	38.0	46.0	32	11.25	29.3	18.34
12	21	40	46.0	54.0	32	11.25	33.6	21.0
13	22	40	54.0	62.0	32	11.25	37.2	23.25
14	23	40	62.0	70.0	32	11.25	40.1	25.05
15	24	40	70.0	78.0	32	11.25	42.2	26.35
16	25	40	78.0	86.0	32	11.25	43.4	27.15
17	26	40	86.0	94.0	32	11.25	43.9	27.42
18	27	40	94.0	102.0	32	11.25	43.4	27.15
19	28	40	102.0	110.0	32	11.25	42.2	26.35
20	29	40	110.0	118.0	32	11.25	40.1	25.05
21	30	40	118.0	126.0	32	11.25	37.2	23.25
22	31	40	126.0	134.0	32	11.25	33.6	21.0
23	32	40	134.0	142.0	32	11.25	29.3	18.34
24	33	40	142.0	150.0	32	11.25	24.5	15.33
25	34	40	150.0	163.0	16	22.50	56.7	35.45
26	35	40	163.0	176.0	8	45.00	50.9	31.79

Table 2.1: Geometrical characteristics of the CHIMERA array. For each detector of a ring, the distance from target, minimum and maximum polar angle, number of modules, azimuthal angle range and covered solid angle are specified.

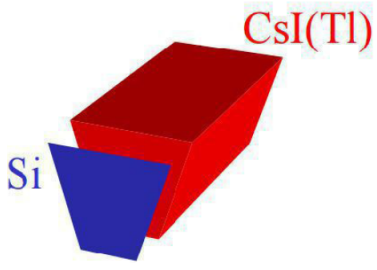

Figure 2.4: The basic detection module (telescope) of the CHIMERA apparatus

dead layer; however, it gives a better overall timing performance [40] because the rise time becomes nearly independent of the impact point of the detected particles. These silicon detectors have a geometry that changes according to the position in the device while the thickness is the same (except for the Silicon detectors of first wheel that have an average thickness of 220 μm) and chosen to optimize the combined ΔE-E+ΔE-TOF techniques, that will be explained afterwards. In the wheels, the forward part of the apparatus, each cell contains two telescopes, and thus two silicon detectors (internal and external detectors) that are characterized by the presence of two active zones in the same Silicon pad, working independently of each other. In figure 2.5, presenting a schematic rapresentation (a) and a photo (b) of wheels silicon detector, it's possible to distinguish the two active zones and the 500 μm wide dead zone of the edge of the detector; moreover, a guard ring is placed in this dead zone around the two pads at a distance of 50 μm from the edges of the active area. The 504 Si detectors of the sphere (figure 2.6), are simple pad detector;

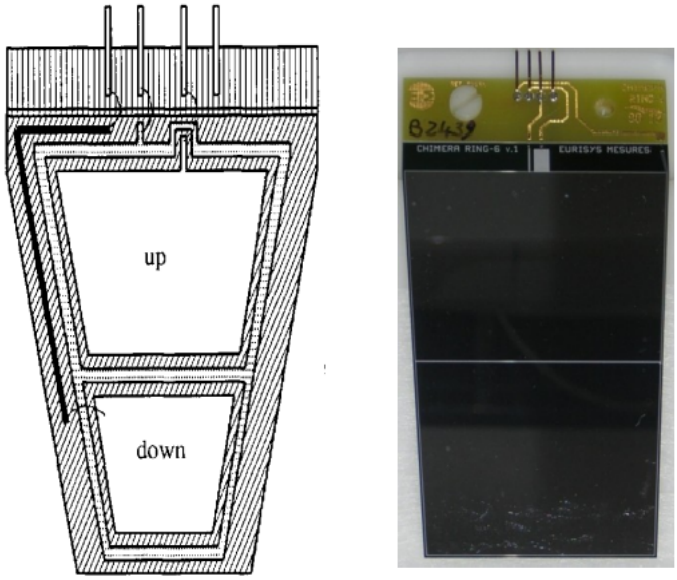

Figure 2.5: A schematic view (a) and a photo (b) of a wheels silicon detector.

even in this case a 500 μm dead zone, in which a guard ring is placed, surrounds the active area. The second stage of CHIMERA's basic module consists of Caesium Iodide Thallium activated crystals CsI(Tl). These scintillators are used to measure the residual energy of particles that punch through the silicon detector [41]. The shape of CHIMERA's crystals is a truncated pyramid with a trapezoidal base; the dimensions of front surfaces are the same of the silicon detector ones and depend on the position in the device. The backward surface is bigger than the front one, depending on the thickness of the crystal that ranges from 3 (at backward angles) to 12 (at forward angles) cm.

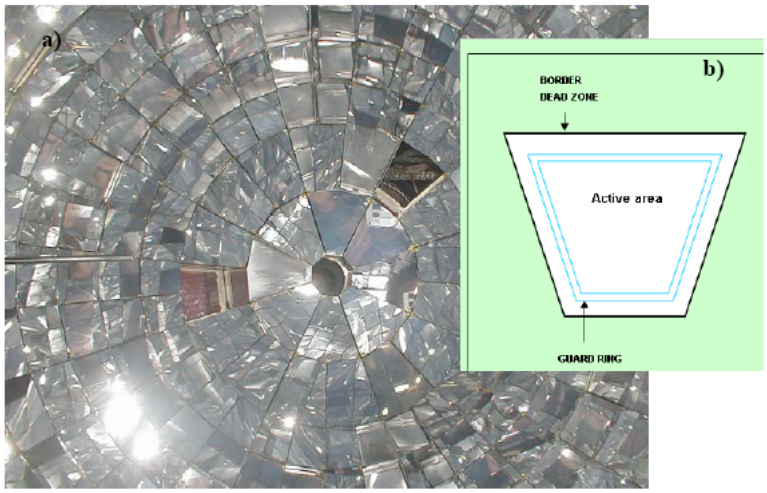

Figure 2.6: A photo (a) and a schematic view (b) of the sphere silicon detectors.

This kind of crystal is chosen as second stage detectors because of its high density, since the high stopping power allows to reduce the thickness needed to stop high energetic light charged particles. Furthermore, they are characterized by relatively low cost, simple handling, a good resistance to radiation damage, good light output performance when coupled with a photodiode or a photomultiplier, and offer the ability to get an isotopic identification through the Pulse Shape Discrimination (PSD) technique, which will be described afterwards. A disadvantage of these scintillators is the non-linearity (at low energies) in light response, that is, light output is therefore not directly proportional to the deposited energy, depending on the ionizing power of the fragment. The CsI(Tl) crystals, in the case of CHIMERA array, are coupled with photodiodes (PD) [42, 43] that, with respect to photomultipliers, are favourites for their low operating voltage (low power dissipation), simple handling and compact assembly under vacuum. The photodiodes, manufactured by Hamamatsu Photonics, are 300 μm thick with an active surface of 18×18 mm^2 and are encapsulated in a ceramic support with the front side (corresponding to the light entrance surface) protected by a thin window of transparent epoxy resin.

2.2 Electronic chain

The signals from Silicon detectors and CsI photodiodes are handled by two different electronic chains that process and digitize the signals so that they can be read by the acquisition system. These electronic chains were designed to satisfy some important requirements: a large dynamic range (from MeV to GeV), a good timing in order to reach a resolution better than 5% (the exact time resolution depends on velocity and base of flight) in velocity measurements through the TOF technique, a low power dissipation under vac-

uum, a high level of flexibility in coupling the detector with other experimental devices and a good energy resolution. The preamplifiers (PA) of silicon detectors and photodiodes are placed on motherboards inside the vacuum chamber in order to reduce electronic noise and signal losses in parasitic circuits, that strongly affect the energy resolution. The number of the preamplifiers placed on a motherboard is not equal for the wheels and the sphere. In fact, in the forward part, each motherboards contains four preamplifiers, two for the internal telescope and two for the external one (each telescope needs two PACs, one for the silicon and one for the photodiode). In this case the motherboards are located on the external surface of the wheels. Instead, the motherboards in the sphere have only two preamplifiers, corresponding to only one telescope, and are located on the top of the metallic baskets containing the telescopes (fig. 2.7). All the motherboards are cooled, using a refrigerating liquid circulation, in order to assures the stability of the electronic against the power dissipation. The voltage generators for detectors and preamplifiers with the rest of the electronic chain are placed outside the vacuum chamber.

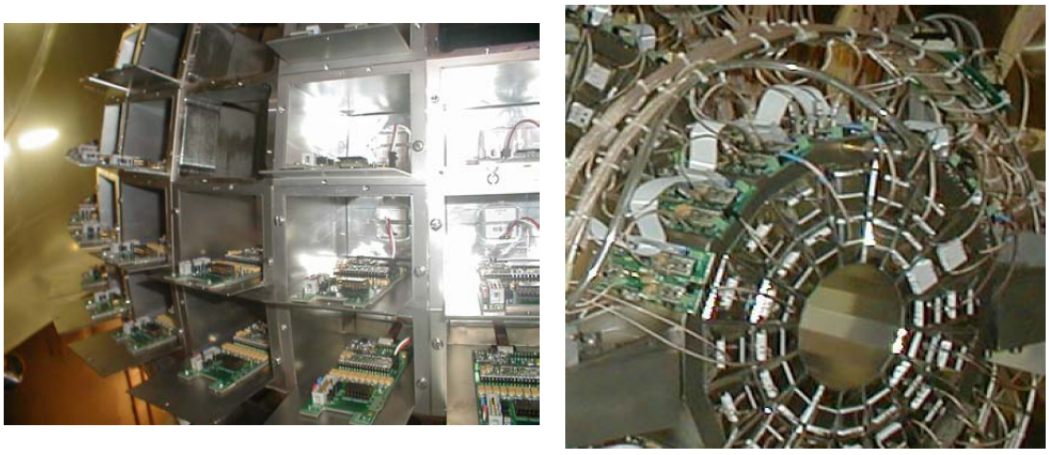

Figure 2.7: Photos of the motherboards for sphere detectors (a) and for wheels detectors (b).

2.2.1 The electronic chain of silicon detectors

The first stage of the electronic chain of silicon detectors is a charge preamplifier designed to perform good timing measurements coupled to high capacitance detector, providing a first amplification of signal. It integrates the detector signal giving an output independent of detector capacity and proportional to the charge produced by the detected particles. Each preamplifier has a test input which accepts signals coming from a pulse generator in order to control the electronic stability. The output is a single negative fast signal carrying time and energy information, with a rise time of $\approx$ 50 - 200 ns and a decay time of $\approx$ 200 μs. The preamplifier sensitivity changes with changing of the polar angle: in

the most forward rings (θ=$1^o \div 10^o$), where the more energetic particles are expected, the sensitivity is 2 mV/MeV, while in the rest (θ=$10^o \div 176^o$) it is 4.5 mV/MeV. In the first period of CHIMERA operation (before 2008), the second stage of the electronic chain was a CAMAC 16 channels bipolar amplifier. Each channel of amplifier produced a negative front bipolar signal (with the positive side 'cutted') as energy output and an unipolar timing output differentiated to 100 ns and integrated to 20 ns. It was also possible to use the multiplex output to observe the signals. Then, the energy signal is coded by a Charge-to-Digital Converter (QDC). Specifically, the conversion of the signal can be "High Gain" (HG) or "Low Gain" (LG). In the first case an amplification factor 8× is applied for low energy signals. Instead, timing logical signals for the silicon detectors are generated by a high resolution Constant Fraction Discriminator (CFD). Each discriminator presents:

- an input signal with 50 Ω impedance and maximum amplitude of 5 V;
- a delay of 20 ns;
- a typical fraction of 30 %;
- a variable discriminator threshold from 1 to 256 mV in step of 1 mV;
- an automatic set of the walk.

In particular, the discriminator provides two output analogical signals: a prompt output used as a start signal for a VME 9U Time-to-Digital Converter (TDC), and a delayed one that, together with an OR output signal, is sent to the trigger control system. The stop signal is then provided by Radio Frequency (RF) of the Cyclotron and sent to the same TDC that gives a 12 bit value proportional to the temporal distance between the start and the stop signals. In figure 2.8 a sketch of the basic electronic chain of silicon detectors is shown. In the last years, substantial changes have been introduced in the electronic chain in order to allow the application of the pulse shape tecnique also to the silicon detectors (described in section 2.4.4). In fact, from ring 4 to ring 13, the old CAMAC electronics has been replaced by new compact modules particularly studied to measure also the rise time of the silicon signal; in this way it's possible to get the charge of particles stopped in the silicon detectors [44, 45]. In particular, in order to measure the rise time of the Silicon signal, a new compact NIM module, coupling an amplifier with two different discriminators characterized by different fraction, 30% and 80%, has been adopted. Two copies of the PA signal are differentiated by 50 and 500 ns and sent, respectively to two CFD with 30% fraction-30 ns delay and 80% fraction-150 ns delay. The CFD outputs are used as start signals of two TDC channels, both receiving as stop signal a delayed copy of the RF signal. By means of the difference between the two TDCs' outputs, $T_{30\%}$ and $T_{80\%}$

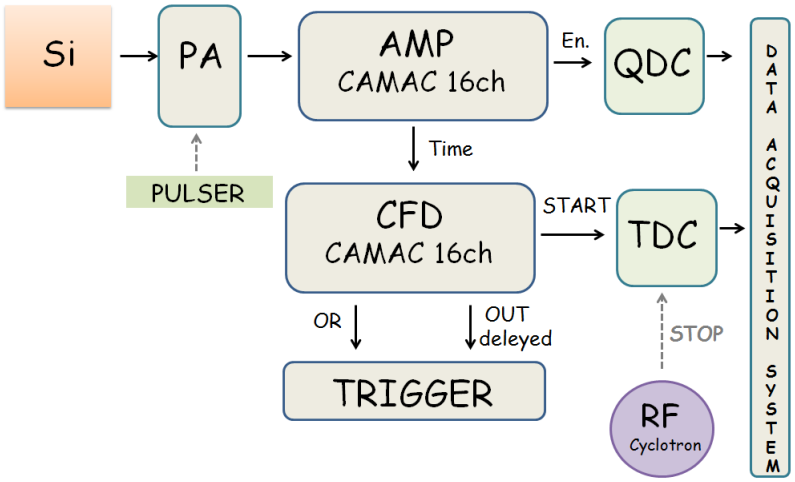

Figure 2.8: Block diagram of the basic front-end electronics of silicon detectors.

respectively, it's possible to obtain the rise time of the signal. Specifically, considering that true values of $T_{30\%}$ and $T_{80\%}$ are equal to:

$$T_{30\%}^{True} = T_{stop} - T_{30\%}^{Measured} \tag{2.1}$$

$$T_{80\%}^{True} = T_{stop} - T_{80\%}^{Measured}, \tag{2.2}$$

the rise time of the signal will be:

$$T_{rise} = T_{80\%}^{True} - T_{30\%}^{True} = T_{stop} - T_{80\%}^{Measured} - (T_{stop} - T_{30\%}^{Measured}) = T_{30\%}^{Measured} - T_{80\%}^{Measured}. \tag{2.3}$$

In figure 2.9 the new configuration with the amplifier and the two different discriminators is schematized (red box).

2.2.2 The electronic chain of CsI(Tl) crystals

The signal from the CsI(Tl) detector firstly is processed by a charge preamplifier that presents the same characteristics of those used for Si detectors, except for the sensitivity that is of the order of $50 \div 100\ mV/MeV$ (Si-equivalent). The rise time of output signals is significantly longer than 50 ns and can reach values of 1-2 microseconds. The output signal is sent to a unipolar amplifier that amplifies and shapes it with variable shaping time (0.5, 1, 2, 3 μs). These amplifiers, assembled in a 16 channel NIM module, have a double output in energy for each channel, with different gains (the higher one is 10 times the lower one) but equal shaping time ($\sim 2\ \mu s$) and a fast timing output with gain 15. The two well shaped energy amplifier outputs follow two separate lines (see fig. 2.14): the higher

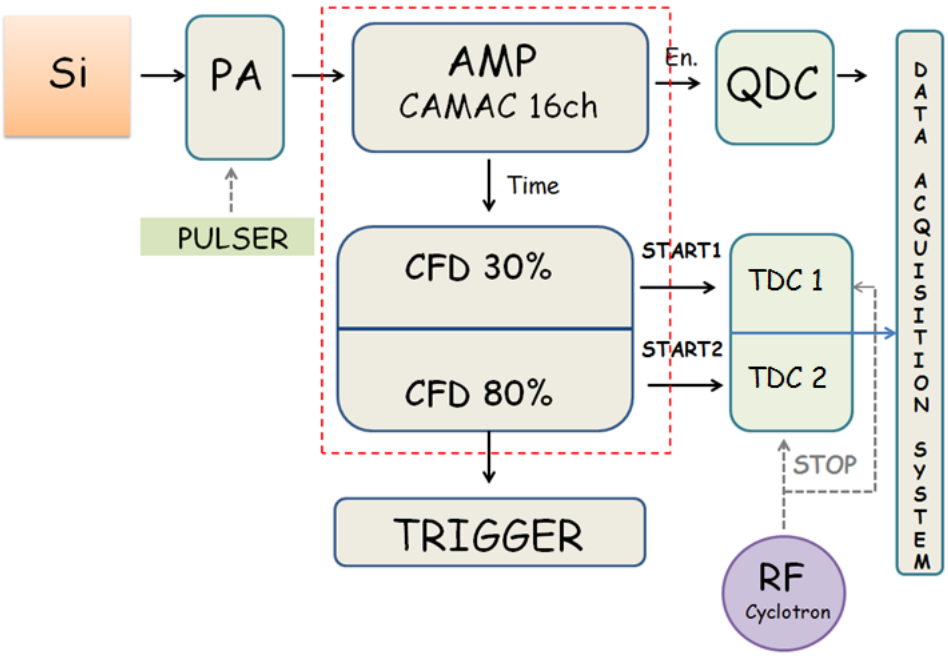

Figure 2.9: Upgrade of the silicon detectors' electronic chain (in dashed box) for the pulse shape technique.

one is sent to a QDC for the integration of the so called slow CsI(Tl) signal component, while the lower one is stretched by a 48 channel module and then sent to another QDC for the integration of the fast signal component (see section 2.4.2). In particular,a stetcher is used in order to avoid the insertion of delays and the effects of jitter in the integration of signals with respect to the common gate.
Figure 2.10 shows a schematic view of the electronic chain of CsI(Tl) coupled with a photodiode (PD). Then, a Data Acquisition System ([46, 47, 48, 49, 50, 51]) is needed that allow a fast overview of growing physical results, in order to collect and store data coming from both Silicon and CsI(Tl) electronic chains.

2.3 FARCOS array

During the InKiIsSy experiment, for the first time, CHIMERA was coupled with 4 telescopes of FARCOS (Femtoscope ARray for COrrelations and Spectroscopy) array [38]. Its main peculiarities are the good energy and angular resolution and the high modularity. Specifically, during this experiment, 4 FARCOS telescopes were placed at 25 cm from the target, subtending the polar angles $15^o \leq \theta_{lab} \leq 45^o$ and an azimuthal interval $\Delta\phi \approx 90^o$. They were used to measure, with better angular resolution than in CHIMERA, IMF and Light Charged Particles.

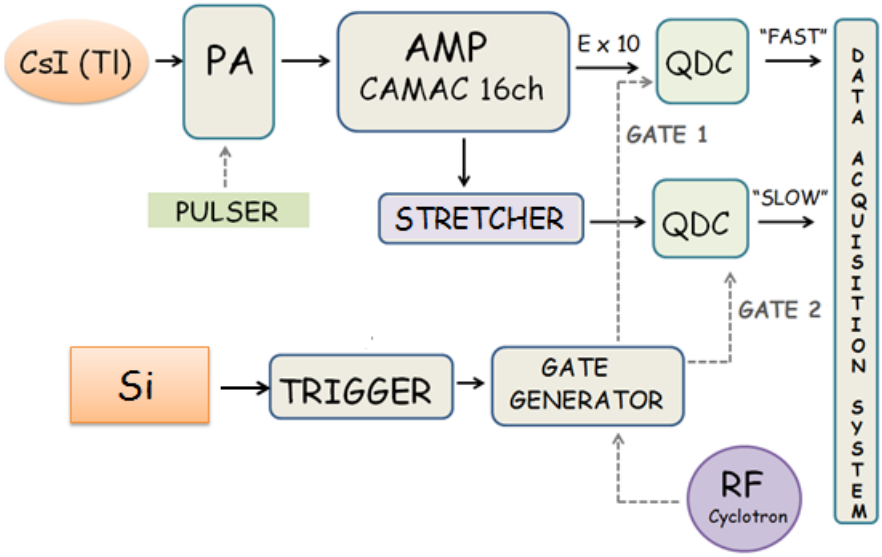

Figure 2.10: The front-end electronics of CsI scintillator.

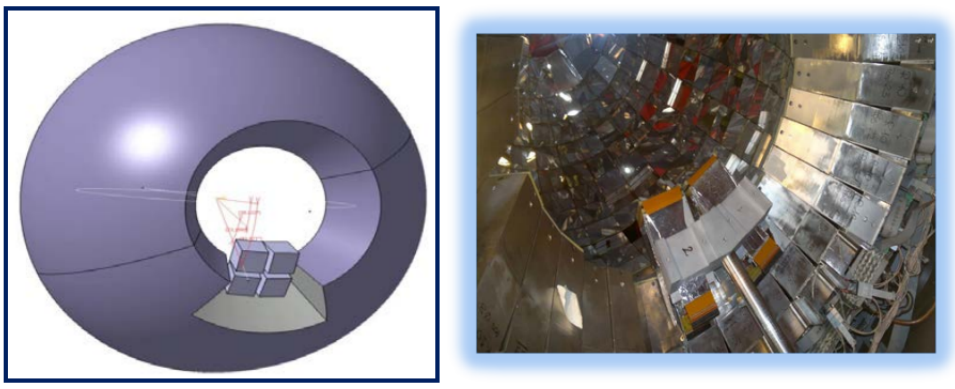

Figure 2.11: A sketch view (left panel) and a photo (right panel) of the 4 telescopes of FARCOS array placed at 25 *cm* from the target ($15^o \leq \theta_{lab} \leq 45^o$, $\Delta\phi \approx 90^o$) inside CHIMERA sphere.

Figure 2.11 presents a sketch view (left panel) and a photo (right panel) of the 4 telescopes of FARCOS array inside CHIMERA sphere, as used during InKiIsSy experiment. In the next subsection the main characteristics of FARCOS array will be presented.

2.3.1 Basic characteristics of FARCOS array

FARCOS is a modular array of telescopes, each telescope can be schematically divided into three stages. Specifically, the first two stages are two double-sided silicon strip detectors (DSSD) with a thickness of 300 μm and 1500 μm respectively, with 32 vertical strips in the front side and 32 horizontal strips in the back side. The third stage is constitued by 4 CsI(Tl) crystals, each of them has a length of 60 mm and a sensitive front area of 32×32 mm^2; the 4 CsI are arranged in a square 2×2 configuration. Each crystal produces a scintillation light which is collected by silicon photodiodes 300 μm-thick with an active area of 18×18 mm^2. The total detection area of silicon detectors is 64×64 mm^2, adapted to cover the total area of the four CsI(Tl) crystals placed behind. Each cluster of FARCOS multi-detector is equipped with 132 independent read-out electronics channels: 128 for silicon strips and 4 for CsI photodiodes. In figure 2.12 the scheme (a) and a photo (b) of a FARCOS telescope is shown. The segmentation in 32 horizontal and 32 vertical strips,

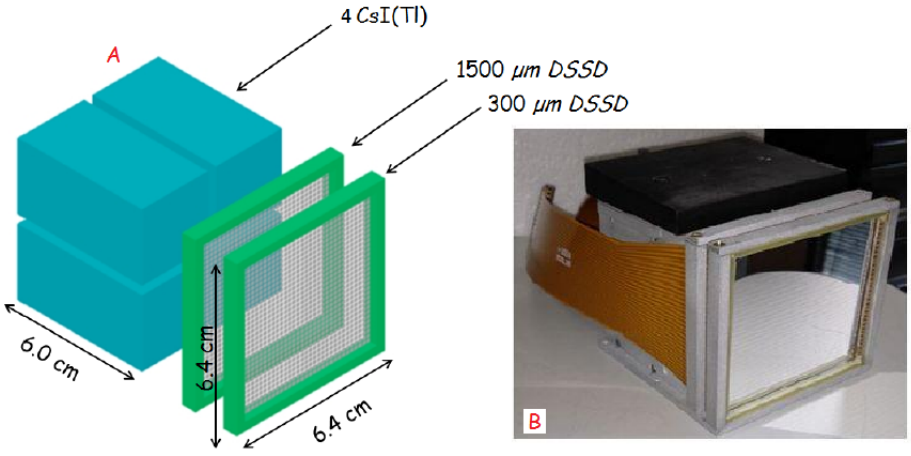

Figure 2.12: Schematic representation (a) and photo (b) of a FARCOS telescope.

determining the presence of 1024 equivalent pixels of 2×2 mm^2, allows to reconstruct with high accuracy the impact position of detected particles, hence their emission angles, with high resolution. High angular resolution combined with high energy resolution provide a good measurement of relative energy and momentum vector between couple of particles, i.e. correlations. Particle discrimination in FARCOS are performed by applying ΔE-E technique to Silicon(300 μm)-Silicon(1500 μm) and Silicon(1500 μm)-CsI stage, and with Pulse Shaping Discrimination of the CsI signal. Moreover, also the Energy-Rise time tech-

nique can be used for particles stopped in the first Silicon stage. With longer base of flight, with respect to the one of InKiIsSy configuration, also ToF measurement is possible. In table 2.2 energies of several ions punching through the three detection stages of a FARCOS telescope are reported; this table shows that FARCOS array, if equipped with very large dynamic range electronics could be able to identify light particles and heavy ions.

Table 2.2: Energy of several ions punching through the three detection stages of a FARCOS telescope calculated with LISE++ software [52].

Ions	**Punch-Through energy** (MeV/A)		
	Si 300 μm	Si 1500 μm	CsI(Tl) 6 cm
p	6	15.5	146.8
α	6.1	15.5	146
^{12}C	11.2	28.5	283
^{16}O	13	33.3	339
^{28}Si	17.1	44.8	486
^{58}Ni	22.6	62.2	765
^{118}Sn	24.8	74.3	1075

Another important feature of FARCOS telescopes is the high flexibility and portability that will permit to couple it to different detector systems in other laboratories, as already done with 4π CHIMERA multi-detector, during the InKiIsSy experiment. The availability of powerful 4π detectors, allows to get a unique tool to characterize the whole collision event in terms of impact parameter, reaction plane, collective motion and to extract important information about the dynamic and time-scale of fragments emission. Since the reduction of data collected with FARCOS array is on-going during the preparation of this thesis, the results presented in this work are limited to the particles identified with CHIMERA multi-detector.

2.4 Identification techniques

In this section the identification methods used by CHIMERA multidetector and FARCOS array will be presented. These detectors measure energy and velocity of the detected particles and identify them in charge and/or mass using different techniques [53, 15]. The energy measurement is based on the physical process by which a charged particle loses part of its (or the whole) energy when crosses a material, while the velocity measurement is performed by the time of flight technique. Specifically, the particles identification for the InKiIsSy experiment was obtained using four different identification methods: **ΔE-E**

technique, **Pulse Shape Discrimination (PSD)** in CsI(Tl) scintillators, **ΔE-Time Of Flight (ΔE-TOF)** technique and **PSD** in Si detectors. The first is employed for charge identification of heavier ions, and charge and mass identification of the lighter ones; Pulse Shape Discrimination technique, using the fast and slow component of CsI(Tl) signals, is used to identify in charge and mass very energetic light charged particles with $Z \leq 4$ stopped in the CsI(Tl) scintillator; ΔE-TOF method, using time of flight and the signal coming from the Silicon, permits to get mass identification of particles stopped in the Si detector; finally, Pulse Shape Discrimination on Silicon signal gives access to charge of light fragments stopped in Si detector, using the energy and the measure of the rise time of the Si signal. The calculation of exact identification limits is quite complicated because they depend on atomic number, mass and energy of detected particle, and on the position of the detector, which changes the base of flight and thus the time of flight. In a simple approximation, imposing that the fragment passes through 280 μm Silicon detector, charge identification energy threshold for ΔE-E ranges from 6 $AMeV$ (^{7}Li) to 12 $AMeV$ (^{16}O). In the case of particle stopped in Si detector charge idetification threshold is $\sim 3-4$ $AMeV$ [45]. The velocity measurements instead, since the first stage of each telescope consists of a Silicon detector with a detection threshold of about 4 MeV, are possible for all charged particles whose energy loss in the Silicon stage is above such energy. Since the velocity measurement is determined by time and distance measurements, its resolution varies with changing of detector position in the device: in particular it goes from 2-3% for the most energetic fragments detected in the first ring up to 10% for the less energetic ones detected in the sphere. Typical time resolution is ~ 1 ns, mainly given by the resolution of the stop (RF) signal. Below, a detailed description of each of the four techniques used will be reported.

2.4.1 ΔE-E technique

In order to identify charged particles through this technique, a ΔE-E$_{res}$ telescope, constituted by a transmission and a stop detector, is necessary. This method is based on the Bethe-Block formula [54]:

$$-\frac{dE}{dx} = \frac{4\pi z^2 e^4}{m_0 v^2}\rho Z[ln\frac{2m_0 v^2}{I} - ln(1-\frac{v^2}{c^2}) - \frac{v^2}{c^2}], \tag{2.4}$$

where v and z are the velocity and the charge of incident particle, ρ and Z are the density and the atomic number of absorber material, m_0 and e are the mass and the charge of the electron, while I is the average ionization energy for the absorbing material. Thus, the average energy lost per unit path, called "stopping power" (indicated by the symbol $-\frac{dE}{dx}$), depends on the characteristics of the incident particle as charge, mass and energy,

and those of the absorbing medium, as density and atomic number. Therefore, the ΔE signal, for non-relativistic charged particles, has an amplitude proportional to:

$$\Delta E \propto \frac{m_p z^2}{E} \Delta x, \tag{2.5}$$

where Δx is the Silicon detector thickness ($\sim 280\ \mu m$) punched through by the incident ion of mass m_p. Moreover, if the incident particle is stopped in the scintillator, the fast component output signal from this last stage of the telescope is proportional to the residual energy just released in Caesium, E_{res}. The sum of these two terms, ΔE and E_{res}, gives the total kinetic energy of the particle:

$$E = \Delta E_{Si} + E_{Res} \approx E_{CsI} \tag{2.6}$$

if $\Delta E_{Si} \ll E_{Res}$.

So, combining the two quantities in Eq. 2.5 and Eq. 2.6 several groups of hyperbole's branches are noticeable in a ΔE-E_{res} bidimensional correlation plot: each group corresponds to a Z value and, inside it, each branch corresponds to a different isotope of the same element (see left panel of fig. 2.13). In the left panel of fig. 2.13 a ΔE-E_{res} matrix

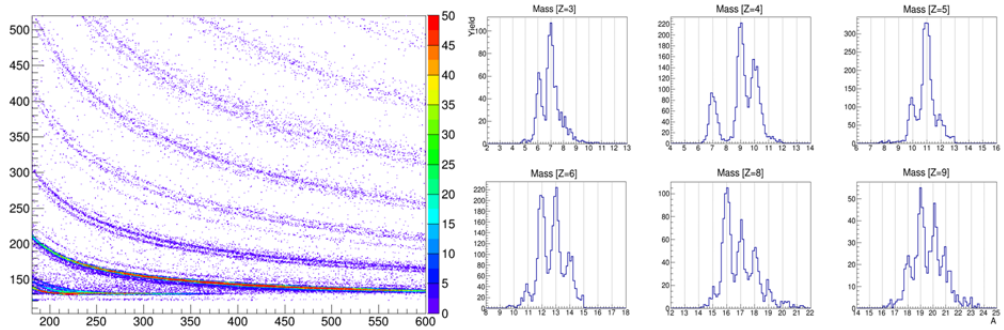

Figure 2.13: ΔE-E_{res} bidimensional correlation plot (left panel) and deduced mass spectra for light ions (right panel) produced in the reaction $^{124}Xe(35AMeV) + ^{64}Zn$ for a detector placed at θ_{lab} =23^o (Ring 8 int).

obtained, for a given detector, during the InKiIsSy experiment for $^{124}Xe(35AMeV) + ^{64}Zn$ reaction is shown, while the right panel presents the deduced mass spectra for light ions: a good identification of the atomic number is obtained and for $3 \leq Z \leq 8$ different isotopes are clearly separated.

This method allows the identification of the particles only in a determined range of Z and E. In fact, in the case of light ions of high energy ΔE signal becomes very small and do not allow the identification. However, it's possible to extend the identification range using a telescope constitued by three detector (ΔE_1-ΔE_2-E_3). Thus, for light ions of high

energy the two quantities (ΔE and E_{res}) will be equal to:

$$\begin{cases} \Delta E = \Delta E_1 + \Delta E_2 \\ E_{res} = E_3. \end{cases} \tag{2.7}$$

In this way FARCOS array, constituted by three stage, allows the particle identification via ΔE-E technique in a larger range of Z and E.

2.4.2 The Pulse Shape Discrimination (PSD) in CsI(Tl) scintillators

The PSD in CsI(Tl) scintillators is an identification technique that allows to identify light charged particles using one of the main the property of CsI(Tl) crystals, the variation of light emitted's shape (in time) with type of incident radiation. In fact, the CsI(Tl) crystal, when excited by an incident particle, produces light mainly through two different types of physical processes, resulting in two distinct light output components. Specifically, the light output of CsI(Tl) can be described by the combination of two exponential components:

$$L(t) = L_1 e^{-\frac{t}{\tau_f}} + L_2 e^{-\frac{t}{\tau_s}}; \tag{2.8}$$

where, $L(t)$ is the the light pulse amplitude at time t, L_1 and L_2 are the light amplitudes for the two components, commonly named *fast* and *slow*, at time t=0. These quantities reflect energy deposited by the particle in the crystal and also the particle species. The fast and slow components are characterized by two different decay constants, τ_f and τ_s, that govern the temporal evolution of the emission process and in the case of CsI have values of about 0.4 μs - 0.7 μs and 3.2 μs, respectively. In particular, for the same energy released in the detector, the distribution of light between the two components, *fast* and *slow*, depends on the specific energy loss of the particles dE/dx, hence on energy charge and mass of incident particle; thus, correlating the intensities of the two components it is possible to identify the particles. This discrimination technique is based on the two gates method [41] adapted to photodiode readout [55]. This method consists in processing the two components of the signal using two QDC with two different gates shifted in time(fig. 2.14 a). In fact, when the signal passes through the amplifier the information relative to the fast component L_1 is maintained unchanged, while the slow component L_2 of the signal, with a characteristic time longer than the amplifier formation time, is cut off and so contributes just to the tail of the total signal. In this way, it's possible to obtain two separated signals proportional to the fast and the slow component produced by the CsI(Tl) amplifier. In the CHIMERA multidetector the signal from amplifier is splitted

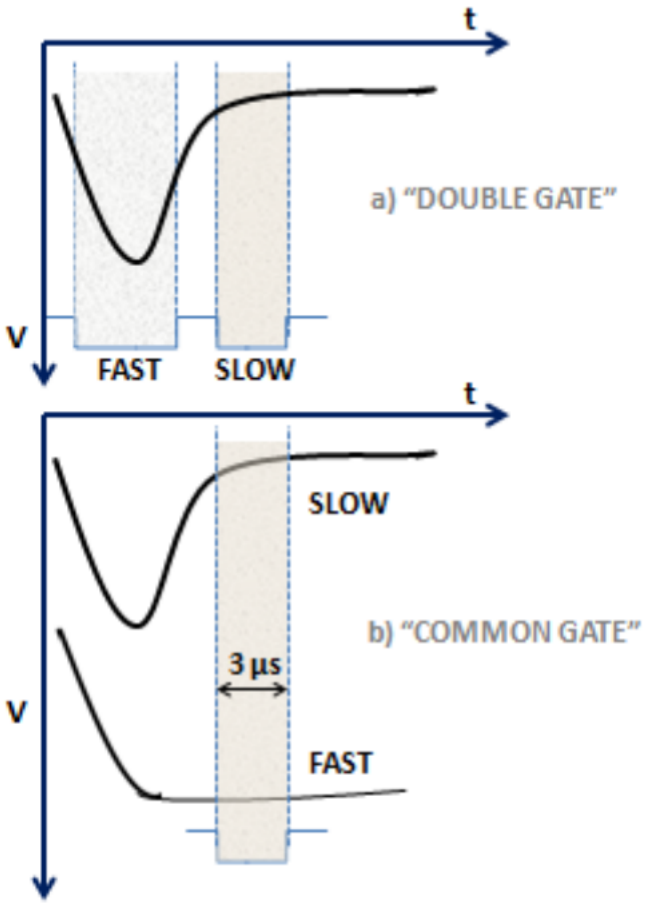

Figure 2.14: Integration of fast and slow components of amplified signals using double gate (a) and the common gate method (b).

in two copies so to work with a common gate integration system. Specifically, one signal is stretched when it reaches its maximum amplitude, while the other remains unchanged. As shown in figure 2.14 b, in this way it's possible to use a single common gate of 3 μs that integrates the tail of the signal, proportional to the slow component, and a part of the stretched signal, proportional to the fast component. The gate is generated using as reference time the RF signal of cyclotron [56]. In figure 2.15 a $fast - slow$ matrix obtained, for a given detector, during the InKiIsSy experiment for $^{124}Xe +^{64} Zn$ reaction at $35AMeV$ is reported; here it's possible to distinguish several lines corresponding to different light elements and their isotopes (p, d, t, ^{3}He, ^{4}He, ^{6}He).

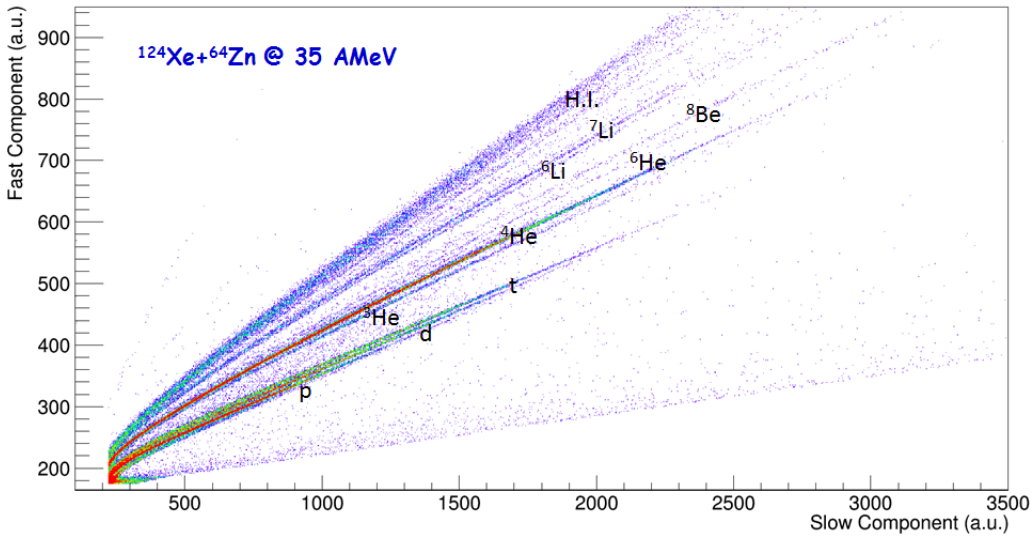

Figure 2.15: Fast-Slow matrix for a detector placed at θ_{lab} =19^o (Ring 7 ext) for the $^{124}Xe+^{64}Zn$ reaction at $35AMeV$.

2.4.3 Time Of Flight (TOF) technique

The TOF measurement is a powerful tool to determine the velocity of the fragments produced in nuclear reactions [57]. In addition, the combination of ΔE and TOF measurement (ΔE-TOF technique) allows to identify in mass the fragments stopped in the first detection stage of our telescopes [53, 58]. In CHIMERA the stored timing information is the time difference between arrival of the particle in the Silicon detector (start), given by the Constant Fraction Discriminator (CFD) acting on Silicon signal, and delayed RF signal (common stop). Given a linear response function of the Time to Digital Converter (TDC) processing the start and stop signals, the measured time t_{ch} can converted into ns by the following formla:

$$t = \alpha(t_{ch})\ ns, \tag{2.9}$$

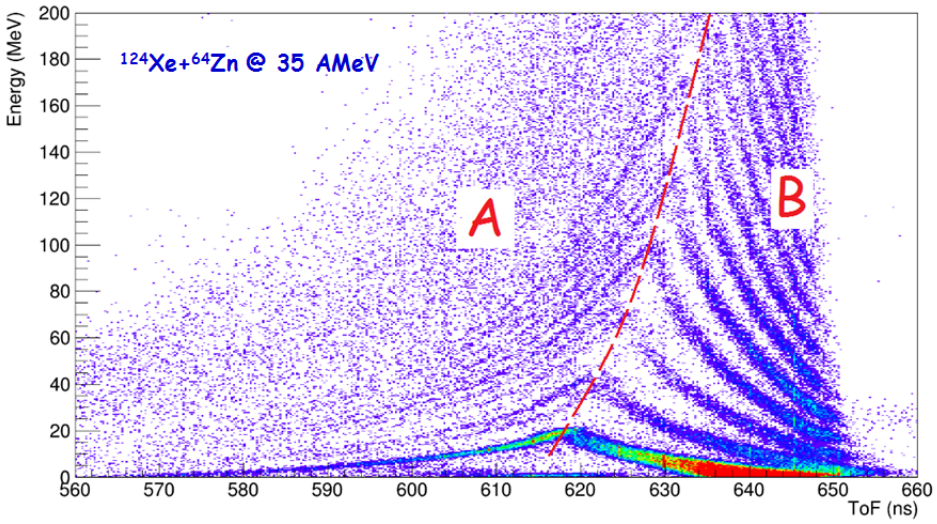

Figure 2.16: Correlation between energy measured in the Silicon detector ΔE and measured time t; see the text for details.

where α is the channels to time conversion, about 0.25 ns/ch in this case. The Time-Of-Flight (TOF) can be simply calculated as:

$$TOF = (t_0 - t)\ ns, \tag{2.10}$$

where t_0 is given in ns. Ideally, the t_0 should be a constant value that takes into account (only) the time delays associated with cables and cyclotron phase; however, as will be seen below, other effects like the pulse delay in the silicon signal and the Constant Fraction Discriminator (CFD) walk effects can affect the t_0; it results that the t_0 will not be a constant but will show a dependence on particle species and energy. Once the TOF is obtained, velocity can be calculated from

$$v = \frac{l}{TOF} = \frac{l}{(t_0 - t)}\ cm/ns \tag{2.11}$$

where l is the base length in cm. Figure 2.16 shows correlation between energy lost in the Silicon detector ΔE and measured t in ns. Specifically, energy calibration of Si detectors was obtained using elastic scattering of two light beams: ^{16}O and ^{12}C at 10 $AMeV$ on Au target.

Before describing the techniques used for the determination of the t_0 parameter, it is necessary to distinguish two cases:

a) The particle punches through the Silicon detectors and is stopped in the CsI scintillator. In that case only a portion of the particle incident energy is measured by the Silicon detector ΔE, and it results:

$$\Delta E \propto \frac{Z^2}{v^2} = \frac{Z^2(t_0 - t)^2}{l^2}. \tag{2.12}$$

Combining ΔE and TOF atomic number (Z) identification could be obtained. This is the case of particles populating the region (B) of fig. 2.16, where the Z lines can be easily recognized. In this case, an ideal behavior for the t_0 parameter has been found, i.e. the t_0 can be assumed to be constant and no dependence on particle species and energy is found [58]. That's the reason why the t_0 used in that region is called t_0^{sat}, i.e. saturated. Probable reason is that for particles punching thorough the Silicon detector, the specific ionization is small (no Bragg peak) and the plasma delay effects are negligible; moreover, signals are large enough to be not affected by CFD walk effects taking place for small signals [59]. In that case the t_0^{sat} is calculated by using Z and A given by $\Delta E - E$ technique, and total incident energy, reconstructed from measured ΔE in a given Silicon thickness, for lighter ions.

b) The particle is stopped in the Silicon detector. In that case the particle incident energy is measured by the Silicon detector, E, and it results:

$$E = \frac{1}{2}Mv^2 = \frac{1}{2}\frac{Ml^2}{(t_0 - t)^2}. \tag{2.13}$$

Combining E and TOF a mass (M) identification could be obtained, since

$$M = \frac{2(t_0 - t)^2 E}{l^2}. \tag{2.14}$$

This is the case of the region (A) of fig. 2.16, where the M lines can be easily recognized. Unfortunately, for particles stopped in the Silicon detectors a dependence of the t_0 on particle species and energy is found. Here specific energy loss can be very high, especially for heavier particles, and plasma delay effect becomes non negligible. Moreover, for low energy particles, CFD walk effects becomes important and non linear effects in the CFD time response occur. To overcome these problems and identify in mass those particles stopped in the Silicon detector, we have developed the following procedure. Loci of well identified (and separated) masses are selected in the correlation plot of fig. 2.16 by means of graphical cuts, as shown in figure 2.17, where selection of atomic mass number A $\approx$ 7, 9, 11, 13, 15 is shown. Assuming these masses, it's possible to calculate the t_0 needed in eq. 2.13 to get the energy measured by the Silicon detector. The correlation between the t_0 needed and particle energy is shown in figure 2.18 (points).

Such a dependence has been parametrized using the following empirical-formula:

$$t_0 = \begin{cases} P_0 + P_1 * \sqrt{\frac{A}{E-P_2}} - P_3 * (S - R(A,Z,E)) * (1 - \exp\frac{-A}{P_4}) & \text{if } (E - P_2) >= 0 \\ t_0^{sat} & \text{if } (E - P_2) < 0 \end{cases} \tag{2.15}$$

where P_0, P_1, P_2, P_3, P_4 are 5 free parameters, to be determined, for each detector, by a fitting procedure. S is the detector thickness, A is the atomic mass number and R(A,Z,E)

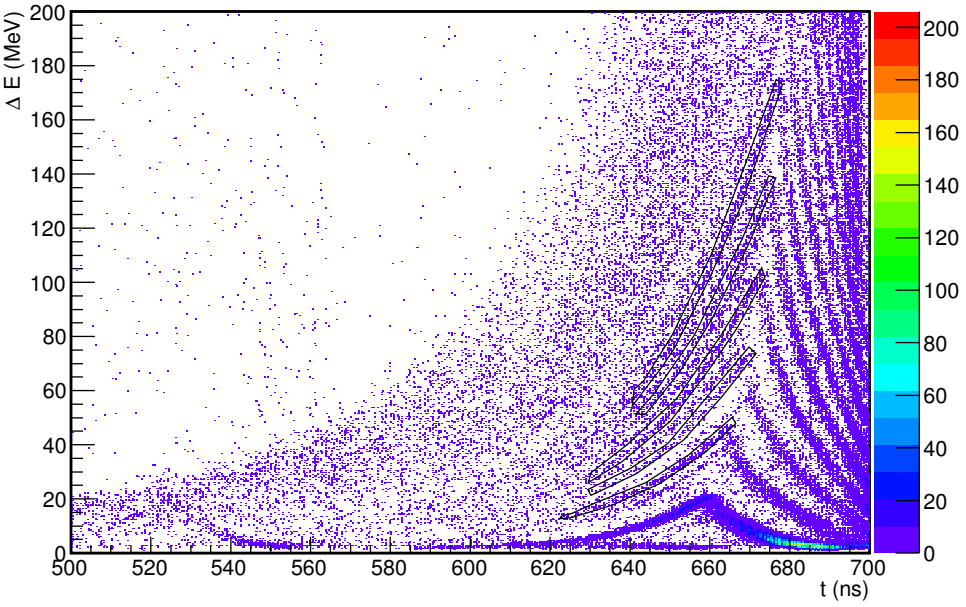

Figure 2.17: Same as fig. 2.16, but with graphical cuts used to select particles with given masses; see the text for details.

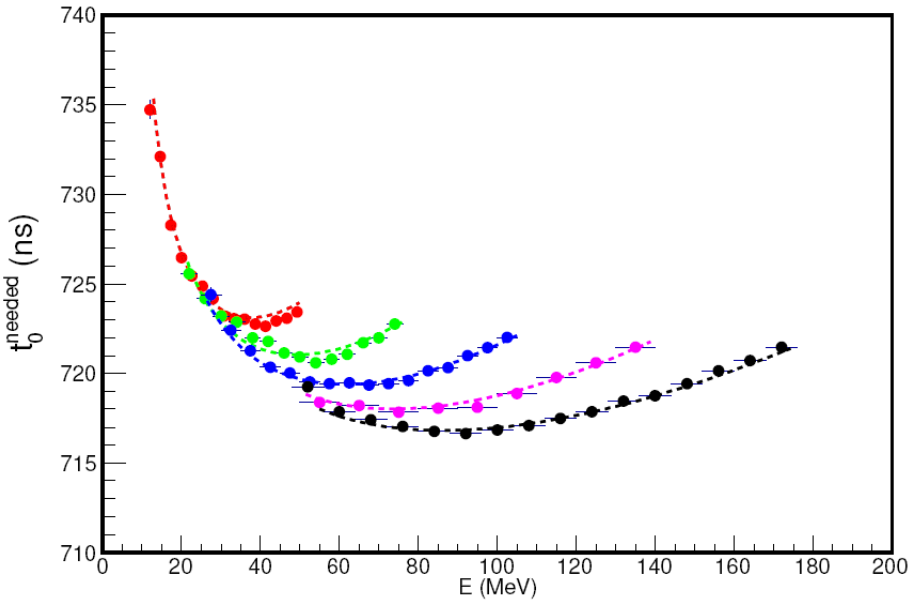

Figure 2.18: Correlation between t_0 needed and energy for the particles selected in fig. 2.17 (points); lines are result of fit using eq. 2.15.

represents the range of the particle in silicon. For a given A, since isotones can not be separated, the more probable Z (according to expected abundance given by EPAX parametrization [EPAX]) is assumed, i.e. Z=3 for A=7, Z=4 for A=9. Usually P_2 is ~ 7 MeV; it follows that for E<7 MeV formula 2.15 is not able to follow the t_0 vs E behavior and a fixed t_0 is adopted, that results in an approximate/wrong mass and velocity estimation. The result of the fit procedure is given by the lines of figure 2.18. Once the five free parameters have been fixed, it's possible to insert eq. 2.15 in eq. 2.14 and calculate masses for the selected particles. The results of the correlation between obtained M and energy is shown in the 1st panel of figure 2.19. It's possible to clearly see that M values are well reproduced and, apart for some small effects, obtained M are independent from particle energy. Obtained M distribution is then shown in the 2nd panel of figure 2.19. Velocity is then obtained by using eq. 2.11.

The general problem is more difficult; drawing graphical cuts for every M value will be very time consuming; moreover with increasing M, M lines cannot be distinguished and mass estimation in that region will not be possible.

In order to asign masses in the whole region (A) of figure 2.16 and to get particles velocity, the following algorithm has been developed. At first it is necessary to consider a trial t_0 value called t_0^{start}, obtained by averaging t_0 value of the selected particles around the Punching Through (PT) region. Such t_0^{start} value is inserted in eq. 2.14 obtaining a starting M value, M^0, and corresponding Z^0, following the expected abundance, and a starting v^0 value from eq. 2.11. Given these values, labeled as ^{0} it's possible to calculate a new t_0^1 from eq. 2.15 and, from that, new values for mass, charge and velocity, that is M^1, Z^1 e v^1. The procedure then follows iteratively, until mass convergence is achieved, i.e.

$$\mid M^{i+1} - M^i \mid < 0.5 \tag{2.16}$$

for two consecutive iterations. In that case iteration is interrupted and M^{i+1}, Z^{i+1} e v^{i+1} values are assumed. The result of the procedure is shown in figure 2.20, where the particles identified with A=7, 9, 11, 13, 15 are superimposed on raw $\Delta E - t$ correlation plot, but with different colors. If after 20 iterations the convergence will not be reached (in about 5% of the case), we have adopted the mean of the values of the first 2 ($\frac{M^0+M^1}{2}$) iterations as that to be adopted.

2.4.4 The Pulse Shape Discrimination (PSD) in Si detectors

The Pulse Shape Discrimination (PSD) in Si detectors is an identification technique that uses the dependence of the shape of the signal from depth of the track, ionization density, electric field profile, and thus from mass, charge and energy of detected particle.

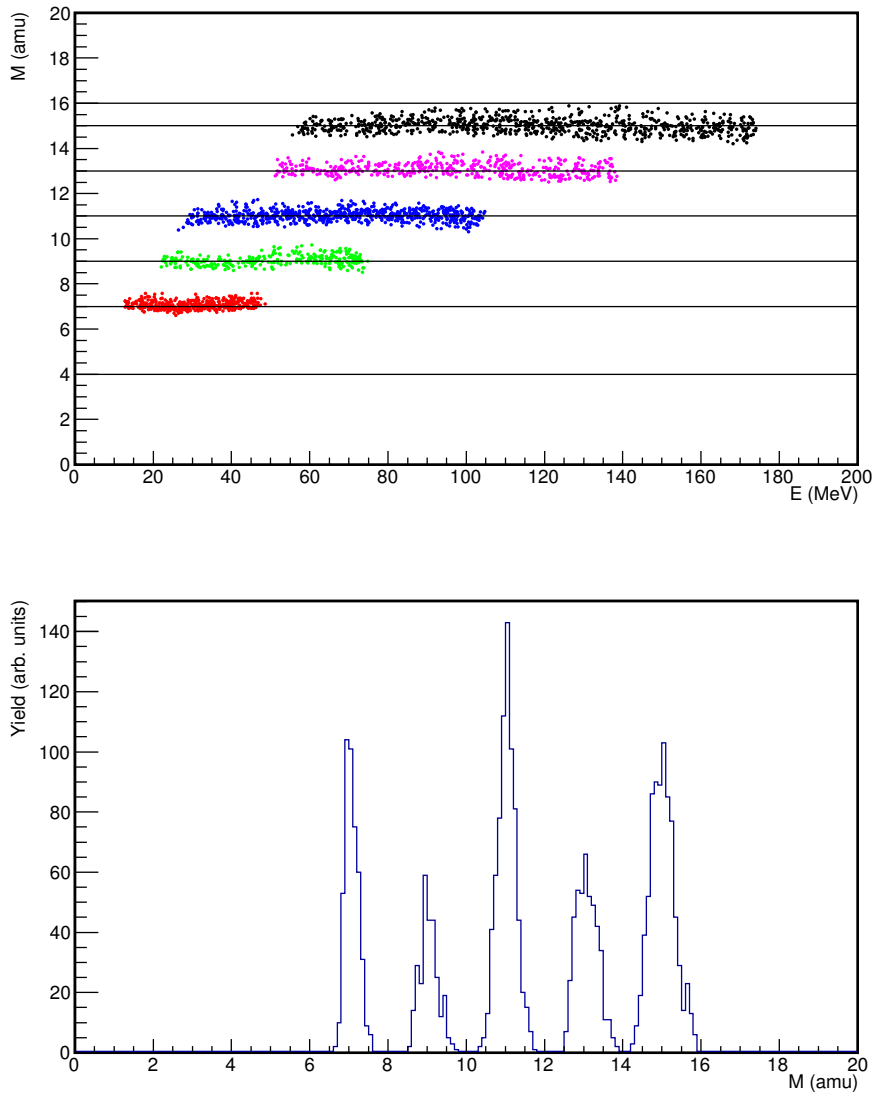

Figure 2.19: Top panel, obtained masses versus energy for the particles selected in fig. 2.17 and, bottom panel, obtained mass spectrum.

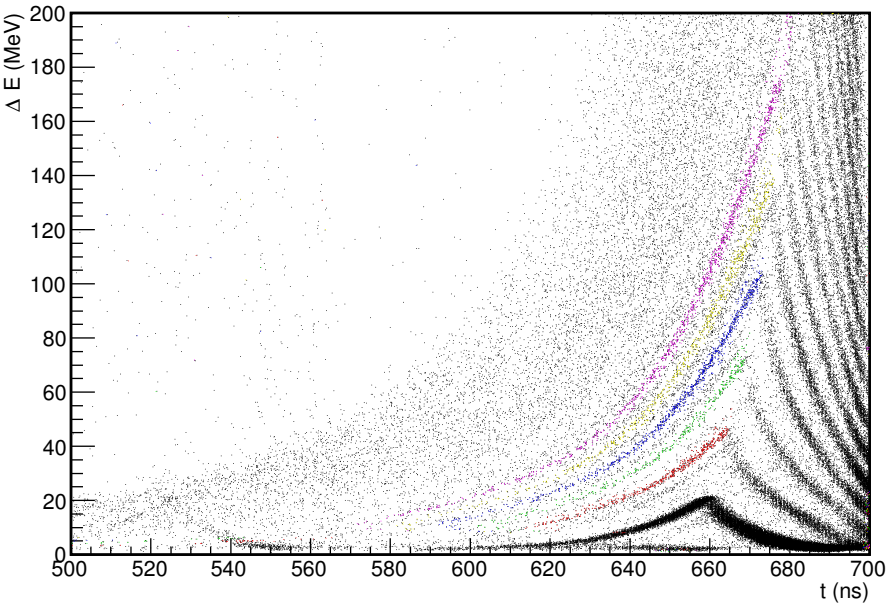

Figure 2.20: Same as fig. 2.16, but with results (colored points) of particles identification applying the procedure described in the text.

This sensitivity is essentially due to the two following effects.

- The high density of charge carriers along the ionization track produces a zone of high conductance, named *"plasma column"*, which expands radially due to diffusion of charge carriers. The time needed for total disintegration of this plasma region, called plasma-erosion time τ_{pl}, depends on initial density and radius of the plasma zone, on the diffusion constant for charge carriers, and on the internal electric field strength.

- The charge carriers which escape from the plasma zone move along the electric field lines towards the corresponding electrode. The drift times depend on the drift paths and drift velocities which are different for electrons and holes.

Both effects are responsible for finite charge-collection time. In particular, if fast high band width charge-sensitive preamplifiers [60, 61] are used, the total charge-collection time is reflected by the rise time of output signal, and consequently rise-time discrimination may be used as a method for particle identification [62, 63]. The plasma-erosion time (τ_{pl}) can be expressed as follows [58]:

$$\tau_{pl} \sim a\sqrt{MZ^2} \cdot \frac{\sqrt{B(\frac{1}{E} ln \frac{4m_e E}{MI})}}{F} \tag{2.17}$$

where a is a normalization constant, M, Z and E are mass, charge and energy of the incident particle respectively, B is the Bethe-Bloch constant ($B = \frac{2\pi e^4 N_0 Z}{m_0 A}$), I is the

average ionization energy for the absorbing material (silicon in this case), m_e is the mass of the electron and F is the applied reverse bias field. Instead, the carrier transit time τ_{tr} is given by the following expression:

$$\tau_{tr} \sim \frac{(S - \frac{R}{2})}{v} \tag{2.18}$$

where S represents the detector thickness, R is the particle range in silicon and v the constant velocity of carrier electrons. These two terms, τ_{tr} and τ_{pl}, are not independent quantities, so in deriving the characteristic charge collection time, which is proportional to the signal rise time, they must be added linearly:

$$\tau_{cc} = \tau_{pl} + \tau_{tr}. \tag{2.19}$$

This simple expression gives a reasonable account of the measured risetime of the signal for incident particles whose range in silicon is long compared to the diameter of their plasma column [64].
In figure 2.21 a deposited energy vs *risetime* (calculated as $T_{80\%} - T_{30\%}$) correlation plot obtained during the InKiIsSy experiment, for a given detector, for $^{124}Xe+^{64}Zn$ reaction at $35AMeV$ is reported. It shows that the obtained separation in Z is very good. Specifically,

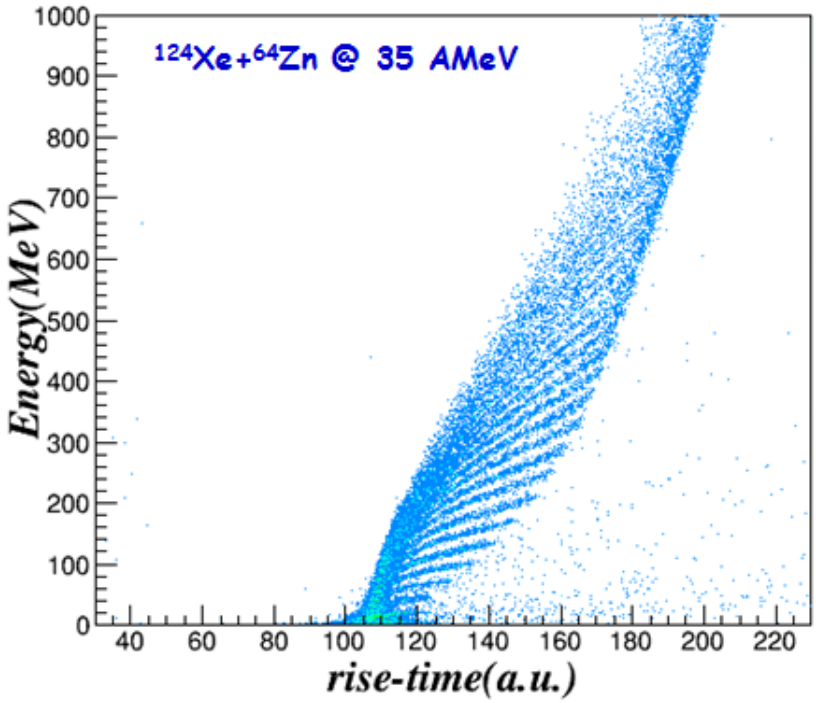

Figure 2.21: Identification scatter plot obtained with one detector of CHIMERA array placed at θ_{lab} =10.75^o (Ring 5 int) for the $^{124}Xe +^{64} Zn$ system at $35AMeV$.

the pulse shape discrimination in Si detectors is realized using a NIM module (already

described in section 2.2.1) that incorporates a linear amplifier for the energy signal, a stretcher for this signal and two Constant Fraction Discriminators: one with fraction fixed at 30 % of the signal and the other with fraction fixed at 80 % of the signal. The pulse shape analysis is performed using a program named *"Psdfit"* [65]. Specifically, at first some reference points are placed on the lines corresponding to various Z, in order to allow the identification in charge.

Then, a fit is performed for these lines using a formula (a parameterization) that takes into account the drift motion of the electrons and holes within the silicon detector under the effect of the electric field. In this way, it's possible to obtain an identification function that allows to identify in charge light fragments stopped in Si detector. Figure 2.22 shows Z distribution for $^{124}Xe(35AMeV) + ^{64}Zn$ system obtained, in a given detector, by applying the described analysis.

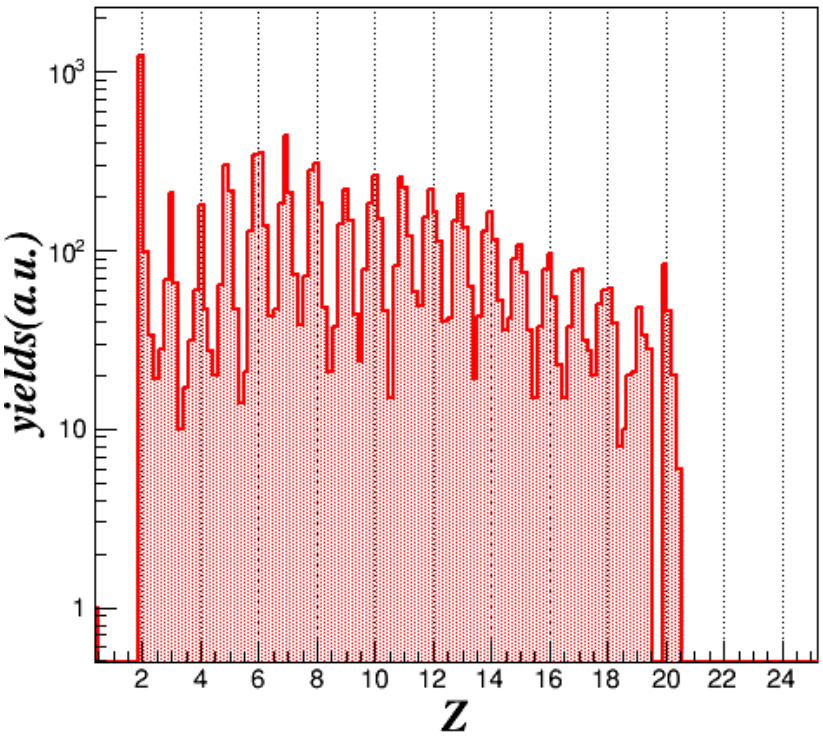

Figure 2.22: Z distribution for $^{124}Xe(35AMeV) + ^{64}Zn$ system obtained by pulse shape analysis for a detector of CHIMERA array placed at θ_{lab} =10.75^o (Ring 5 int).

Chapter 3

Telescopes response classification

3.1 Classification method

Before starting the physical analysis of the experimental data, a check of energy/velocity calibration and particles identification is useful in order to improve the quality of data analysis. In fact, working with a complex apparatus as CHIMERA multi-detector, it's important to review and select the data in order to identify part of data affected by systematic errors or distortions; in this way, the physical analysis may be carried out on good data that guarantees a better reliability. Thus, it is necessary to examine the data provided by each telescope and compare them with those of the telescopes of the same ring; in fact, the azimuthal symmetry of the reaction should ensure a given uniformity in the values of various measured physical quantities. This analysis should be performed separately for different types of fragments, since different charges (and relative energies) correspond to the use of different signals and identification techniques. In particular, the analysis has been restricted to three significant charge intervals: $40 \leq Z \leq 45$, $22 \leq Z \leq 27$ and $5 \leq Z \leq 10$. The physical quantities used to evaluate the behavior of each telescope are: the number of counts, the energy and the velocity of the particles. Figure 3.1 shows mean energy and number of counts for the telescopes of the ring 2 int, for the $^{124}Xe(35\ AMeV)+^{64}Zn$ system and the $5 \leq Z \leq 10$ charge interval. Specifically, considering the number of particles detected in each telescope, it's possible to verify the uniform response of the telescopes of each ring: compared to the average value of the same ring, the lower number of counts may be due to the lack of identification of some particles or to non-functioning telescopes, instead, the greater number of counts could be due to problems in the read-out system (e.g. noise). The average value of the energy of particles detected in each telescope ($< E_{tel} >$) and the relative error ($\Delta < E_{tel} >$) are calculated according to the following formulas:

$$< E_{tel} >= \sum_{i=1}^{N_p} \frac{E_i}{N_p} \tag{3.1}$$

$$\Delta < E_{tel} >= \frac{\sqrt{\sum_{i=1}^{N_p}(E_i - < E_{tel} >)^2}}{N_p} \tag{3.2}$$

where N_p is the total number of particles detected in the telescope in the specific charge range, while E_i is the energy of the i-th particle. The telescopes that have a small (< 60 % of the mean of the ring) number of identified particles are classified as non-functioning. They must be removed from the total statistic in order to evaluate the actual angular coverage during the experiment and therefore the quality of the available data. Then, there are those telescopes for which some identification techniques could not be used. For example, when the time signal of the silicon detector is missing, the TOF technique can not be utilized and the particles stopped in the Si detector can not be identified. Therefore, in the case of light fragments, only more energetic fragments, that pass through the first element (Si), may be identified. In this case, the number of counts in the telescope is lower while the average value of the energy is higher than that of other telescopes of the same ring. The non-availability of the TOF technique becomes irrelevant with increasing charge of the fragments, because, due to the kinematics of the reaction, the heavy PLFs have enough energy to not be stopped in the silicon detector; in fact they are mainly identified through ΔE-E technique. Their energy is well measured but velocity info is missing.
Instead, in the case in which the ΔE-E method can not be used, only the identification of the fragments stopped in silicon is allowed; in this case the telescope doesn't work for PLFs; while, for light fragments, it results that the number of counts and the average value of the energy are lower than those of the others telescopes of the ring. Comparing the average value of the energy and the number of counts of each telescope inside a ring, it's possible to recognize these two cases. Another case observed is that of telescopes with average energy and number of counts that are "strange" compared to those of neighboring telescopes; in this case the reasons can be various: problems related to electronic chain, errors in the procedure of the identification or calibration, or even problems related to malfunctioning of the detector.
From this first analysis, large differences between the two reactions have been not found: this is to be expected because the two measurements were performed almost at the same time, so the operation of the detectors was about the same. Thus, the analysis has been continued by taking into account only the $^{124}Xe(35AMeV) + ^{64}Zn$ system.
One of the main observed cases is that of the telescopes for which TOF technique or ΔE-E method can not be used. For example, in figure 3.2, that shows mean energy and number of counts for the detectors of ring 4 ext in $22 \leq Z \leq 27$ charge interval, some telescopes

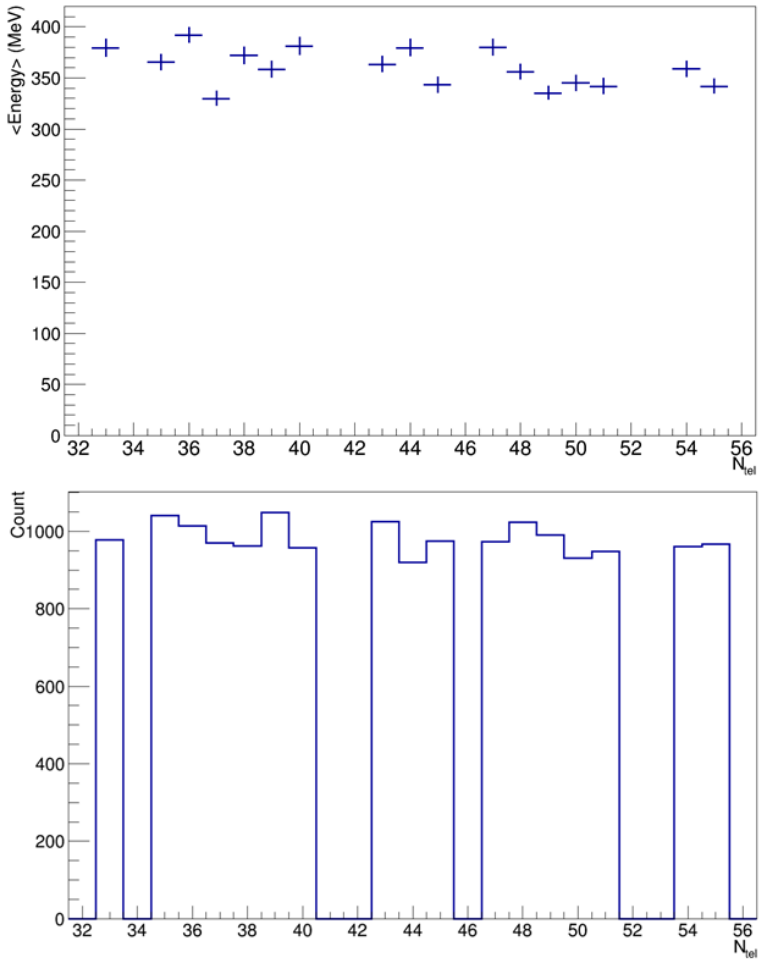

Figure 3.1: Distributions of average energy (upper panel) and number of counts (bottom panel) for the telescopes of the ring 2 int, for the $^{124}Xe(35\ AMeV)+^{64}Zn$ system and the $5 \leq Z \leq 10$ charge interval.

(as 192-199) are not present because ΔE-E technique could not be used. Instead, in the case of telescope 219, that has a value of energy higher than those of other telescopes of the same ring, TOF technique is missing.

Another problem observed is that of telescopes with average energy much different than

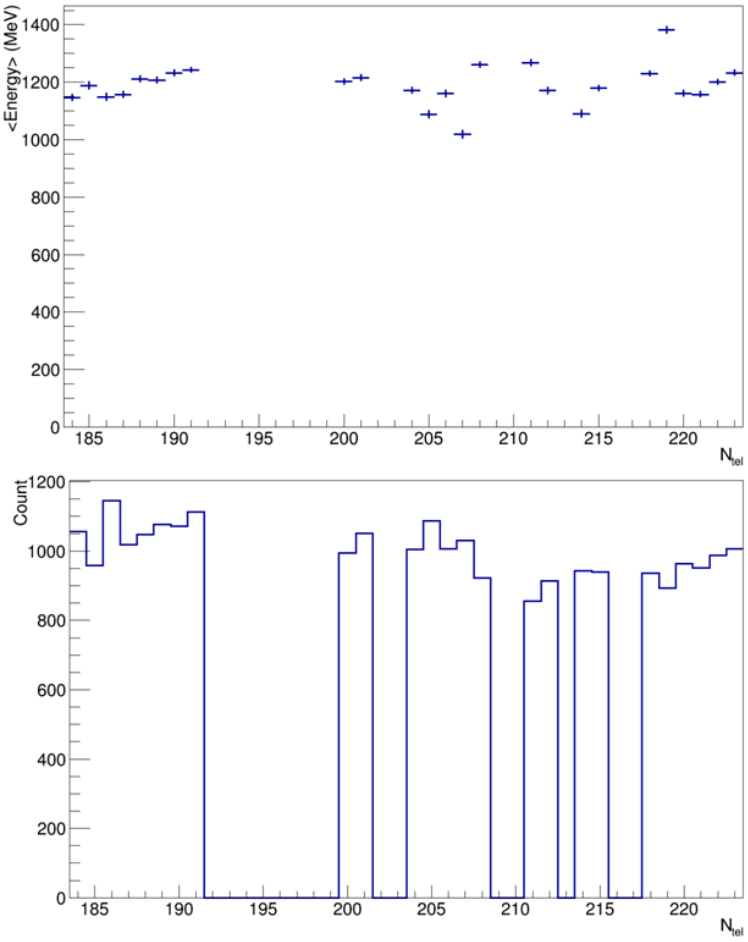

Figure 3.2: Mean energy (upper panel) and number of counts (bottom panel) of the telescopes of ring 4 ext, for the $^{124}Xe(35AMeV) +^{64} Zn$ reaction for the $22 \leq Z \leq 27$ charge interval.

that of neighboring telescopes. An example is given in figure 3.3, in which distributions of average energy and number of counts for the detectors of ring 5 ext in $5 \leq Z \leq 10$ charge interval are shown. In this range, telescope 295 presents a value of energy lower respect to that of other detectors. In this case, the cause of the deviation is due to a wrong energy calibration. Moreover, some telescopes present a mean energy value much different than that of neighboring telescopes: this deviation could be due to some noise occured during data taking.

In order to evaluate quantitatively the various problems, the average value of energy, velocity and number of counts of each telescope are normalized with respect to the average for the corresponding ring, according to the following formulas:

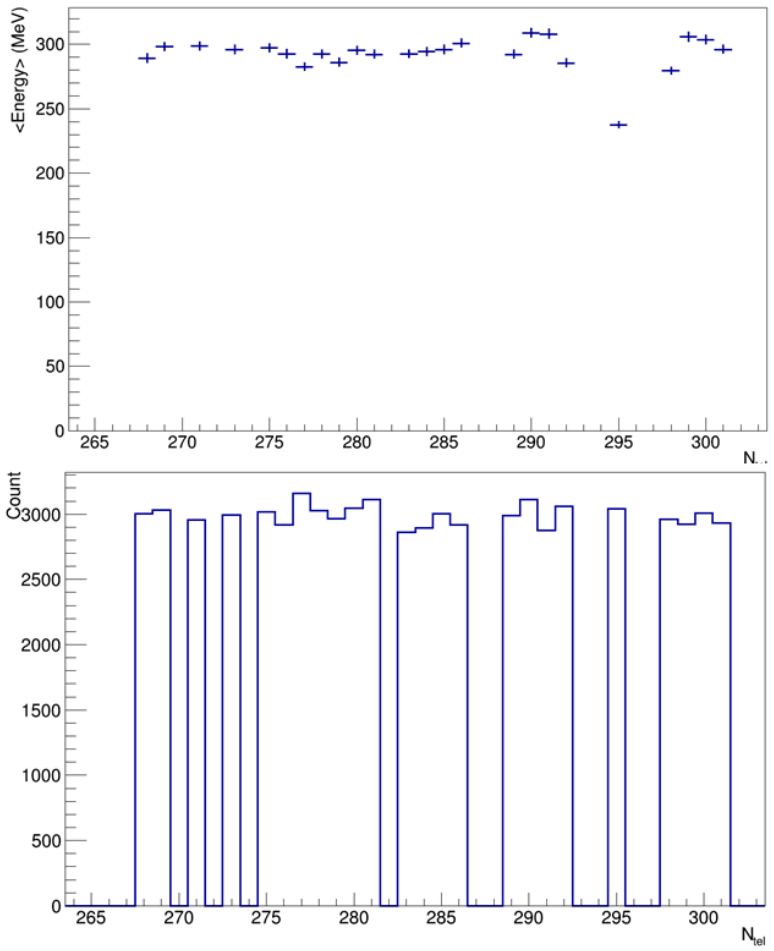

Figure 3.3: Mean energy (upper panel) and number of counts (bottom panel) of the telescopes of ring 5 ext, for the $^{124}Xe(35AMeV) + ^{64}Zn$ reaction for the $5 \leq Z \leq 10$ charge interval.

$$< E_{tel} >_{norm} = \frac{< E_{tel} >}{<< E_{tel} >> |_{ring}} \tag{3.3}$$

$$< v_{tel} >_{norm} = \frac{< v_{tel} >}{<< v_{tel} >> |_{ring}} \tag{3.4}$$

$$< Count_{tel} >_{norm} = \frac{< Count_{tel} >}{<< Count_{tel} >> |_{ring}} \tag{3.5}$$

where $<< E_{tel} >> |_{ring}$, $<< v_{tel} >> |_{ring}$ and $<< Count_{tel} >> |_{ring}$ are calculated using the following relations:

$$<< E_{tel} >> |_{ring} = \frac{\sum_{ring} < E_{tel} >}{N_{tel}} \tag{3.6}$$

$$<< v_{tel} >> |_{ring} = \frac{\sum_{ring} < v_{tel} >}{N_{tel}} \tag{3.7}$$

$$<< Count_{tel} >> |_{ring} = \frac{\sum_{ring} < Count_{tel} >}{N_{tel}}, \tag{3.8}$$

N_{tel} is the number of the telescopes of the ring, excluding those considered "bad". In particular, the parameters used to classify the telescopes is given by the following relations:

$$Q_{telE} =< E_{tel} >_{norm} -1 \quad Q_{telV} =< v_{tel} >_{norm} -1 \quad Q_{telC} =< Count_{tel} >_{norm} -1. \tag{3.9}$$

Plotting these values (calculated in %) for each telescope, a graph in which the various points are located around the value "0" is obtained (fig. 3.4). In this way, after trying to fix those telescopes "recoverable", one can remove those detectors that deviate much from the "0" value and reject bad telescopes in order to avoid "distortions" of the observables used in the analysis.
Specifically, for each charge interval ($40 \leq Z \leq 45$, $22 \leq Z \leq 27$ and $5 \leq Z \leq 10$), the "well working" detectors have been quantitatively selected considering a certain range of Q_{telE}, Q_{telV} and Q_{telC}. In particular, the range chosen, in %, are:
- for $5 \leq Z \leq 10$, $-20 < Q < 20$,
- for $22 \leq Z \leq 27$, $-25 < Q < 25$,
- for $40 \leq Z \leq 45$, $-33 < Q < 33$.

Figure 3.5 shows Q_{telV} distributions for the three charge intervals: the yellow lines indicate the ranges chosen to include the detector data into the analysis. As a conseguence of the selection procedure, the percentage of telescopes excluded from the data analysis is about 10% (telescopes covered by FARCOS detector are not included in this percentage).

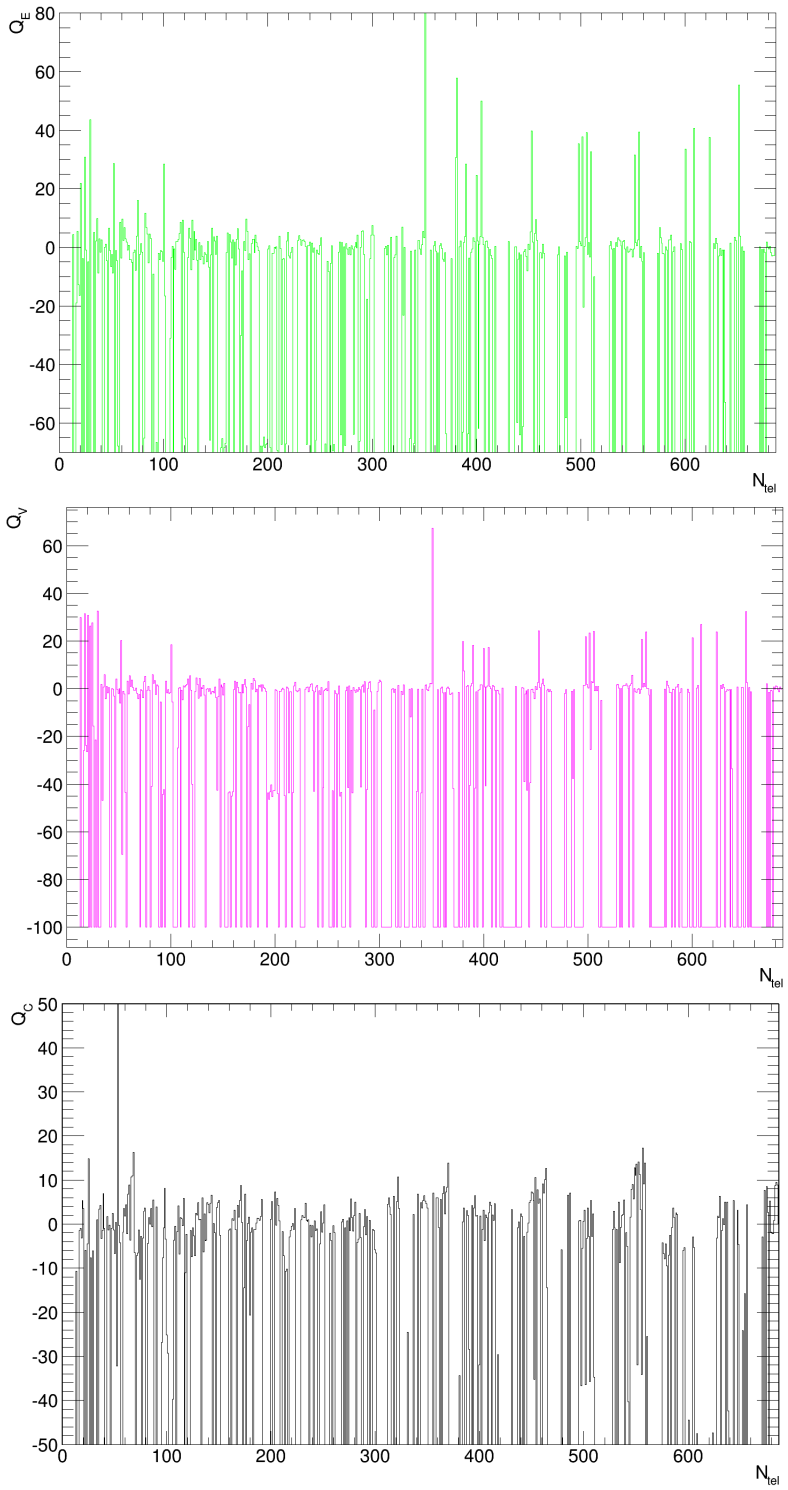

Figure 3.4: Distributions of Q_{telE}, Q_{telV} and Q_{telC} for the telescopes of the nine wheels of the CHIMERA multidetector. They are relative to the $^{124}Xe(35\ AMeV)+^{64}Zn$ system for the $5 \leq Z \leq 10$ charge interval.

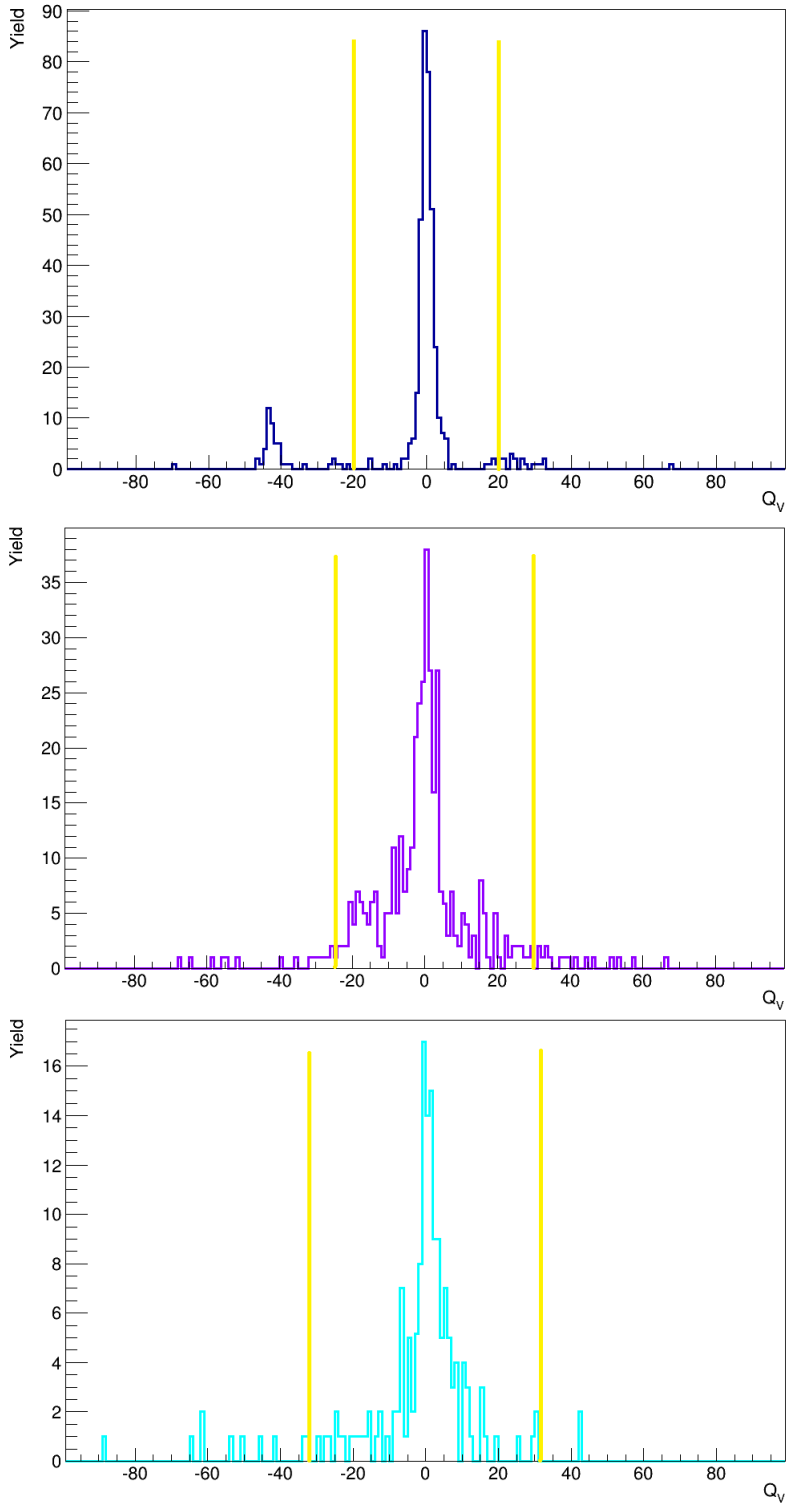

Figure 3.5: Distributions of Q_{telV} for the telescopes of the nine wheels of the CHIMERA multi-detector for each charge interval, $40 \leq Z \leq 45$ (upper panel), $22 \leq Z \leq 27$ (second panel) and $5 \leq Z \leq 10$ (bottom panel), for the $^{124}Xe(35\ AMeV)+^{64}Zn$ system.

Chapter 4

Analysis and experimental results

In this chapter the experimental results of the InKiIsSy experiment will be shown. As already said, during this experiment, performed at the LNS cyclotron facility in Catania, by using CHIMERA and FARCOS detectors, the two isobaric systems $^{124}Xe +^{64} Zn,^{64} Ni$ were studied at 35 $AMeV$ beam energy, in order to distinguish entrance channel isospin effects from the ones related to initial different mass between systems, as seen in the results of the REVERSE experiment. Infact, the obtained results will be compared also with the ones of REVERSE experiment.

4.1 Global variables

The reaction pattern, such as dissipation, IMFs production, etc., is strongly dependent on the impact parameter b of the collision. B can be related to the violence of the collision but it isn't a measurable quantity. However there is a way to evaluate it; in fact, in HI reactions at intermediate and relativistic energies, total charge particles multiplicity (total number of particles detected in each event) is correlated with the violence of the collision and, thus, to the impact parameter. More precisely, multiplicity mean value decreases monotonously as a function of b. Thus, the total multiplicity of detected particles can be used as centrality selector, in both Fermi energy and relativistic nucleus-nucleus collisions [29].

Figure 4.1 shows the total multiplicity (M_c) in CHIMERA for the two systems (^{124}Xe(35 $AMeV$)+^{64}Zn and ^{124}Xe(35 $AMeV$)+^{64}Ni). Specifically, highest values of multiplicity can be associated to central collisions, in which many particles are expected to be produced in a single event, while the lower values of multiplicity can be associated to semi-peripheral collisions. As a matter of fact, it's possible to observe that the system with the neutron rich target tends to produce more charged fragments than the system with the neutron poor target. This small difference observed in raw (unsorted) data deserves further work.

It could be related to difference in the grazing angle (see below) between the two systems or to some other target effects. Using the method of Cavata et al. [29] (explained in Appendix

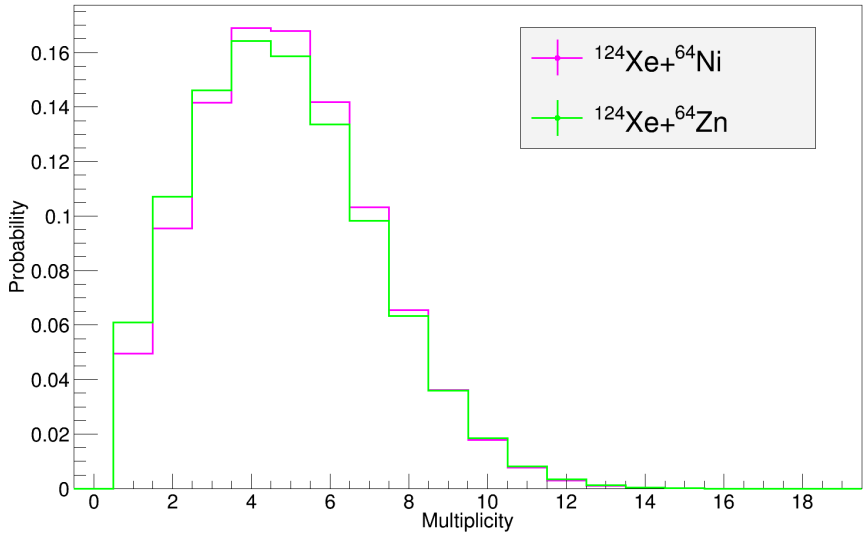

Figure 4.1: Distribution of total charged particle multiplicity for $^{124}Xe +^{64} Zn$ (green line) and $^{124}Xe +^{64} Ni$ (pink line) systems at 35 $AMeV$.

A), it's possible to extract a quantitative relation between detected multiplicity and impact parameter. This correlation is shown in figure 4.2, in which reduced impact parameter ($b_{red} = b/b_{max}$, where b_{max} is the maximum geometrical impact parameter and it's equal to $R_p + R_t$, with R_p and R_t radius of projectile and target respectively) is considered. The same condition of the REVERSE experiment (see section 1.2.1), in which the events selected were those with reduced impact parameter $b_{red} \geq 0.7$ (corresponding to $M_c \leq 6$ for the REVERSE neutron-rich system and $M_c \leq 7$ for neutron-poor one), is obtained with the condition $M_c \leq 6$ for both systems. These selections were carefully evaluated through some simulations performed with HIPSE [32] as event generator and CHIMERA filter [33], used to estimate detection efficiency for both experiments. In this case M_c is lower because the number of used telescopes during InKiIsSy experiment was lower with respect to those used in REVERSE. Infact, during InKiIsSy experiment CHIMERA array was coupled with four telescopes of FARCOS array that covered some telescopes of the 4π multi-detector and, as said before, FARCOS data are not used in this analysis. Moreover, in order to reproduce the same condition of REVERSE experiment, only the first 687 telescopes with $\theta_{lab} \leq 30^o$ are used for this analysis.

Other importan global variables used to characterize the events are the total charge of all particles identified in a single event, Z_{tot}=$\sum_i Z_i$, and the correlation between Z_{tot} and the total longitudinal impulse P_{tot}=$\sum_i P_i^{long}$. Specifically, the distributions of Z_{tot} for $^{124}Xe +^{64} Zn$ (green line) and $^{124}Xe +^{64} Ni$ (pink line) systems at 35 $AMeV$ are presented

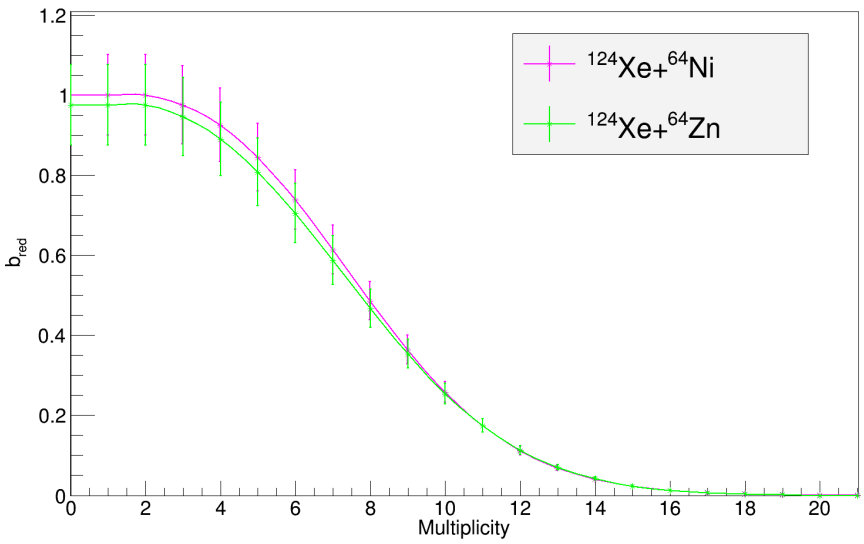

Figure 4.2: Estimated reduced impact parameter $b_{red} = b/b_{max}$ versus multiplicity for $^{124}Xe+^{64}Zn$ (green line) and $^{124}Xe+^{64}Ni$ (pink line) systems at 35 $AMeV$.

in figure 4.3. These distributions give an indication of the geometric efficiency of detection

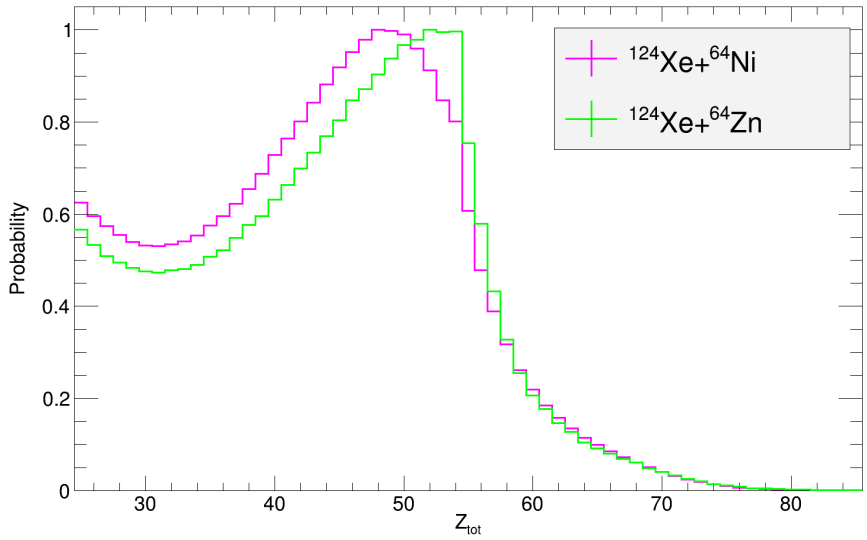

Figure 4.3: Distributions of Z_{tot} for $^{124}Xe(35\ AMeV)+^{64}Ni$ (pink line) and $^{124}Xe(35\ AMeV)+^{64}Zn$ (green line).

configuration. In particular, the distributions result highly concentrated around $Z \approx 50$ (slight below the charge of projectile) and only in some cases a total reconstruction of the event is obtained ($Z \approx 75$). The difference between the two systems could be related to the tendency of the system with neutron poor target to produce more elastic events with respect to $^{124}Xe+^{64}Ni$ system, due to the different grazing angle ($\theta_{Grazing}(Zn) = 2.55$ and $\theta_{Grazing}(Ni) = 2.37$); also this plot refers to raw (unsorted) data. Figure 4.4 shows the

correlation between Z_{tot} and total longitudinal impulse P_{tot} for $^{124}Xe(35\ AMeV)+^{64}Ni$ reaction: in events with $Z_{tot} \gtrsim 40$ and $P_{tot} \gtrsim 0.7$ the PLF has been well detected, while events with $Z_{tot} \gtrsim 70$ and $P_{tot} \approx 1$ are the so-called complete events in which also the TLF has been well detected. Figure 4.5 shows the $Z - V_{par}$ two-dimensional plot for

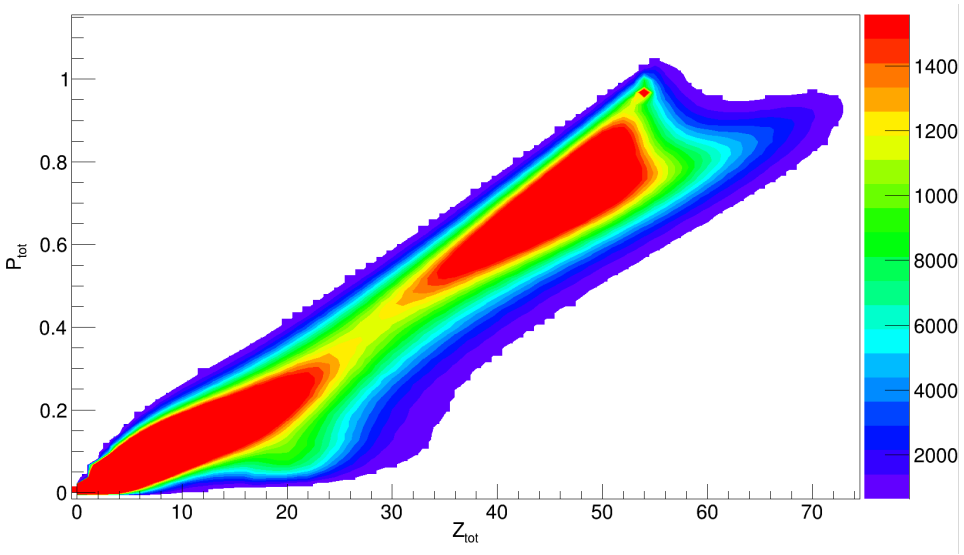

Figure 4.4: Correlation between Z_{tot} and total longitudinal impulse P_{tot} for $^{124}Xe(35\ AMeV)+^{64}Ni$ reaction.

the reactions $^{124}Xe +^{64} Ni$. In this plot it's possible to distinguish the so-called ternary events, semiperipheral reactions in which one can observe a production of IMF in almost ideal condition, since the final-state configuration involves mainly one IMF accompanying PLF and TLF. Specifically, selected events are those in which the three heaviest fragments satisfy the following conditions:

$$Z(1) + Z(2) + Z(3) > 60, \tag{4.1}$$

$$P_{long}(1) + P_{long}(2) + P_{long}(3) > 0.6 P_{beam}. \tag{4.2}$$

In the plot 4.5, it's possible to distinguish three strongly populated regions, recognized as PLF, TLF and IMFs regions. For both systems, those events, with a "heavy" PLF residue detected, have been selected, requiring V_{par}^{PLF} >6.5 cm/ns and $Z^{PLF} > 22$. The $Z - V_{par}$ plots of selected PLFs are shown in figure 4.6, for the Ni (upper panel) and Zn (lower panel) targets, respectively. Associated to this selection it's possible to consider another global variable, IMF multiplicity. In particular, figure 4.7 presents the total charged particle multiplicity for events in which an as above defined PLF is detected, for $^{124}Xe(35\ AMeV)+^{64}Ni$ (pink line) and $^{124}Xe(35\ AMeV)+^{64}Zn$ (green line) reactions, without any distinction between PLF IMF and TLF. Instead, figure 4.8 shows multiplicity distributions

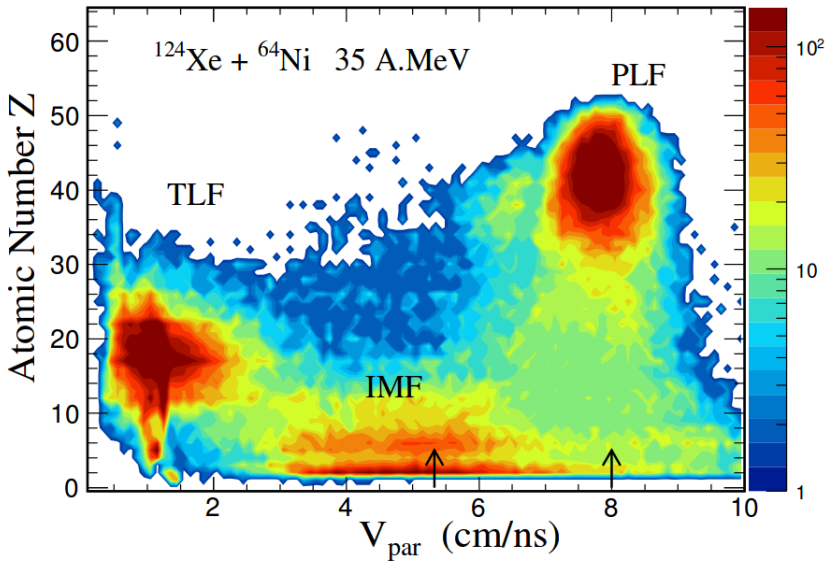

Figure 4.5: Distribution of fragments for the $^{124}Xe(35\ AMeV)+^{64}Ni$ system as a function of their atomic number Z and their longitudinal velocity for ternary events.

of IMFs ($Z \geq 3$) associated to one as above defined PLF detection excluding eventually detected target-like fragments (fragments with $Z > 10$ and $V_{par} < 3\ cm/ns$). As in ref. [3], also in this case, an higher IMFs multiplcity in coincidence with PLF is found for the system with neutron rich target. This confirms a dependence of IMF emission probability on the isospin content of the reaction channel; infact in this case the two systems have same mass and only different Z (and N/Z) for the target.

4.2 Dynamical fission

In order to select peripheral collisions, in which scattering of PLF is followed by its fission-like splitting into two massive fragments, the events with almost complete PLF detection ($30 \leq Z_{tot} \leq 85$) and $M_c \leq 6$ (which corresponds to $b_{red} \geq 0.7$) are selected. Then, among selected events, the two heaviest fragments (bigger atomic number) of each event are considered; they will be referred as, according to their charge, Heavy (Z_H) and Light (Z_L) fragment. The charge distributions of these fragments are shown in figures 4.9 and 4.10. Being interested in investigating heavier IMFs emission coming from PLF splitting, the events corresponding to the mass ratio of the two heaviest selected fragments $A_{Heavy}/A_{Light} < 4.6$ are chosen (fig. 4.11); in this way, after putting a lower limit on $Z_{2F} = Z_H + Z_L$ (see after), the lighter fragment of the two has mostly charge $Z_L \gtrsim 9$. Z_H and Z_L distributions, corresponding to this selection, are shown with a red lines in figures

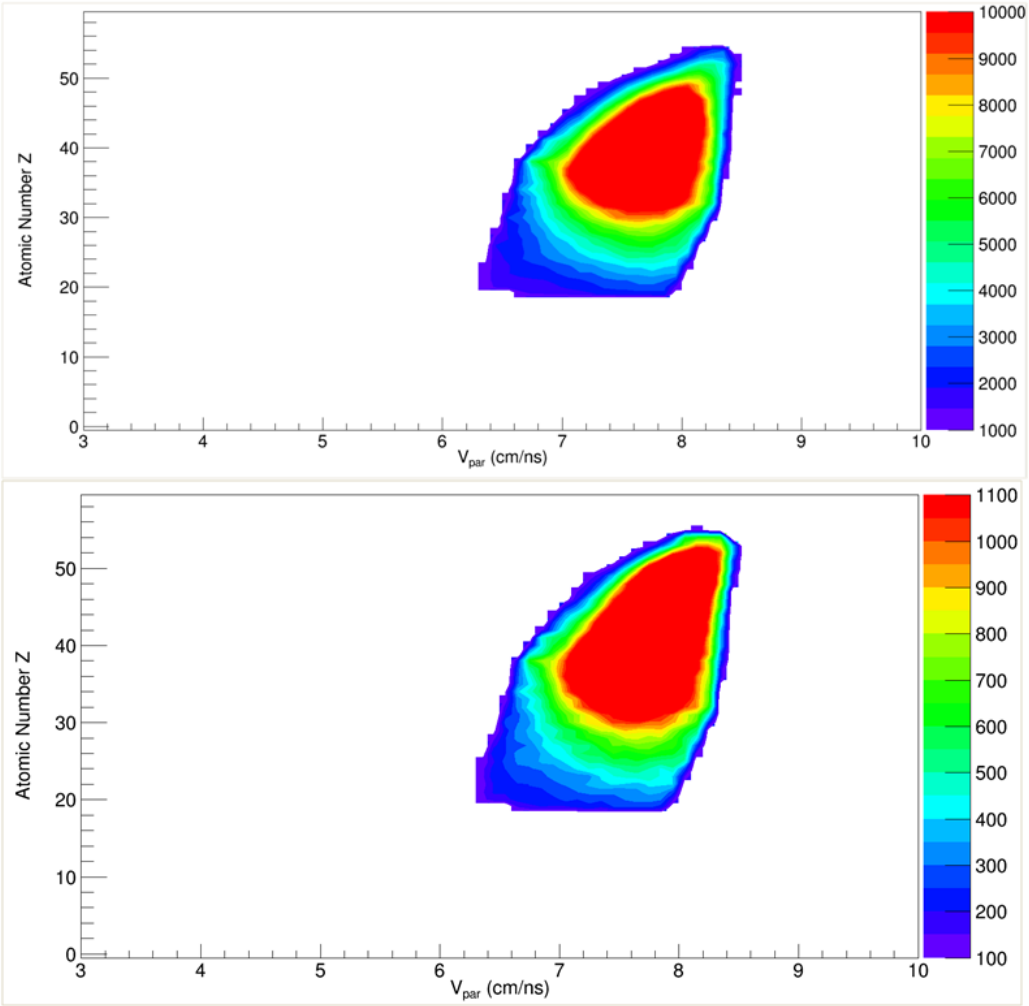

Figure 4.6: Atomic number Z vs parallel to the beam component velocity of PLF selected for the $^{124}Xe(35\ AMeV)+^{64}Ni$ (upper panel) and $^{124}Xe(35\ AMeV)+^{64}Zn$ (lower panel) reactions.

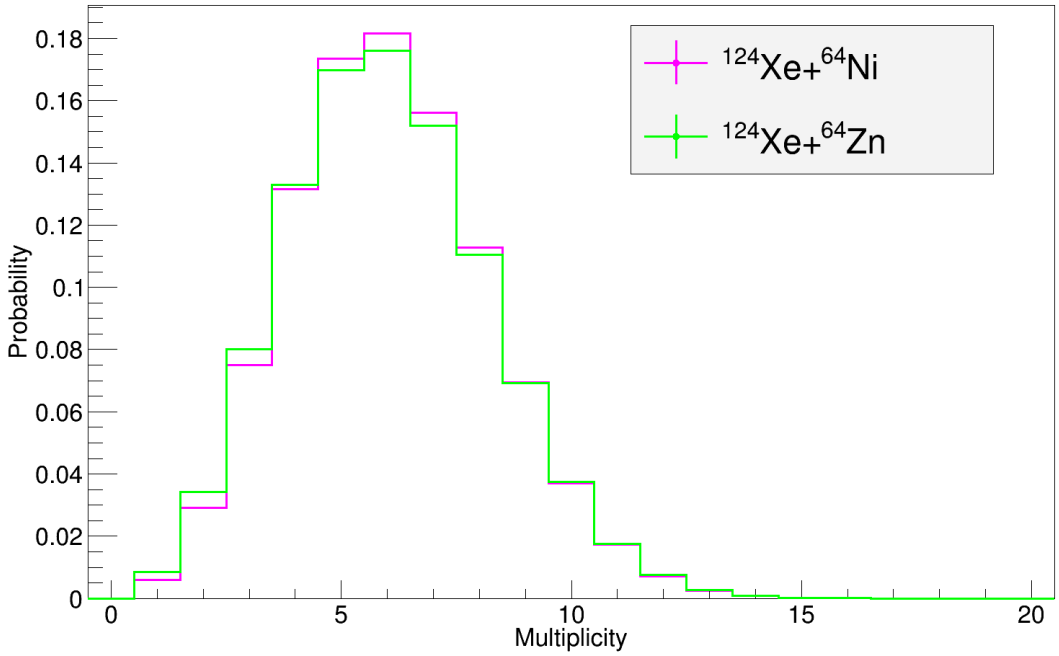

Figure 4.7: Total charged particle multiplicity for events in which a PLF (see figure 4.6) is detected, for $^{124}Xe(35\ AMeV)+^{64}Ni$ (pink line) and $^{124}Xe(35\ AMeV)+^{64}Zn$ (green line).

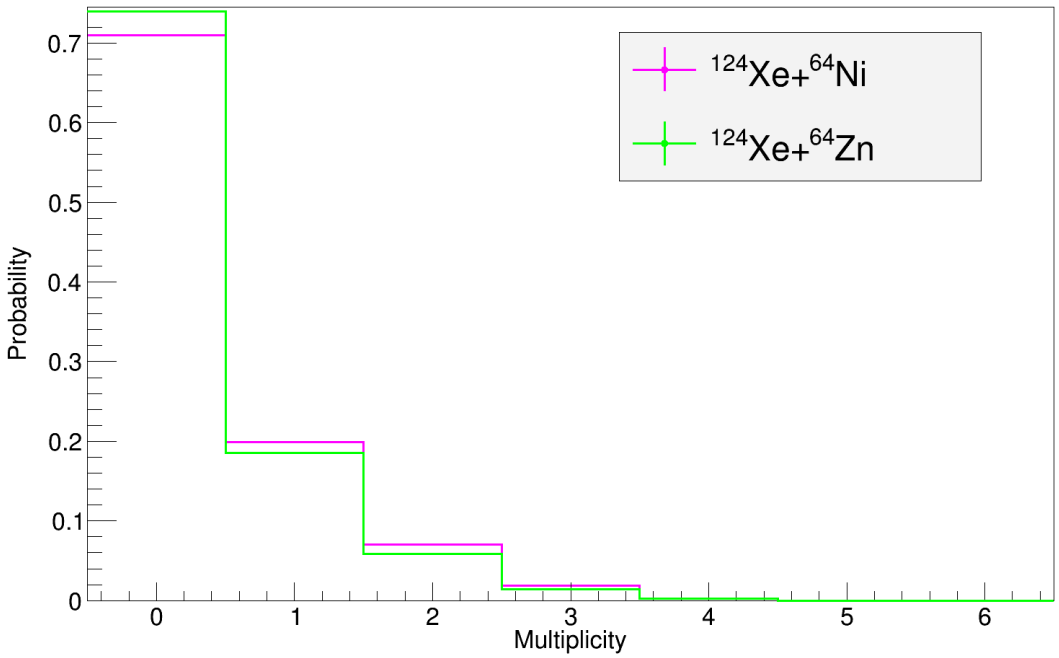

Figure 4.8: Multiplicity distributions of IMFs ($Z \geq 3$) for $^{124}Xe(35\ AMeV)+^{64}Ni$ (pink line) and $^{124}Xe(35\ AMeV)+^{64}Zn$ (green line) associated to PLF (see figure 4.6).

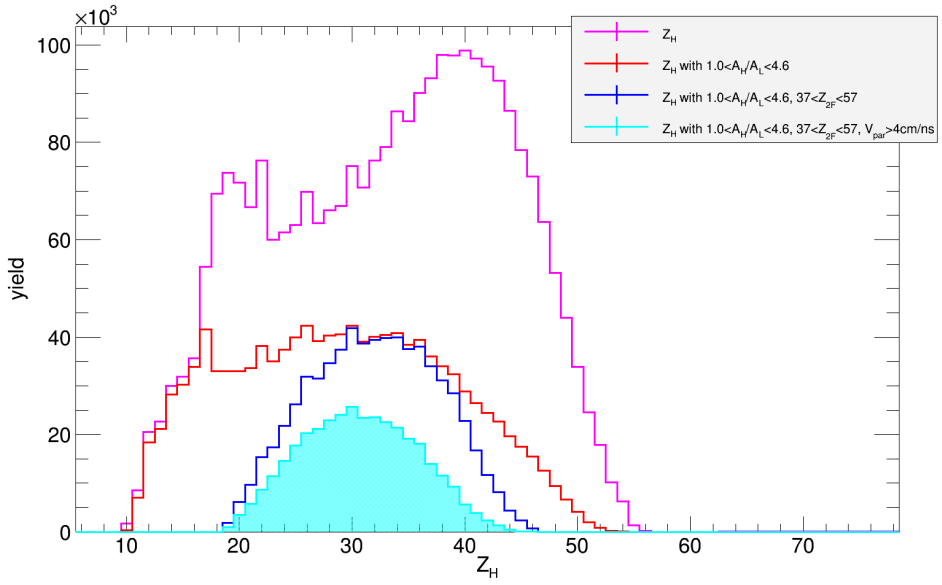

Figure 4.9: Distribution of Z_H for different selection conditions for $^{124}Xe(35\ AMeV)+^{64}Ni$ system. Specifically, purple line indicates Z_H distribution with only event selection (Z_{tot} and M_c); red line indicates Z_H distribution requiring also $1.0 < A_{Heavy}/A_{Light} < 4.6$; blue line indicates Z_H distribution requiring also $37 < Z_{2F} < 57$; light blue line indicates Z_H distribution requiring also $V_{par}^L > 4\ cm/ns$.

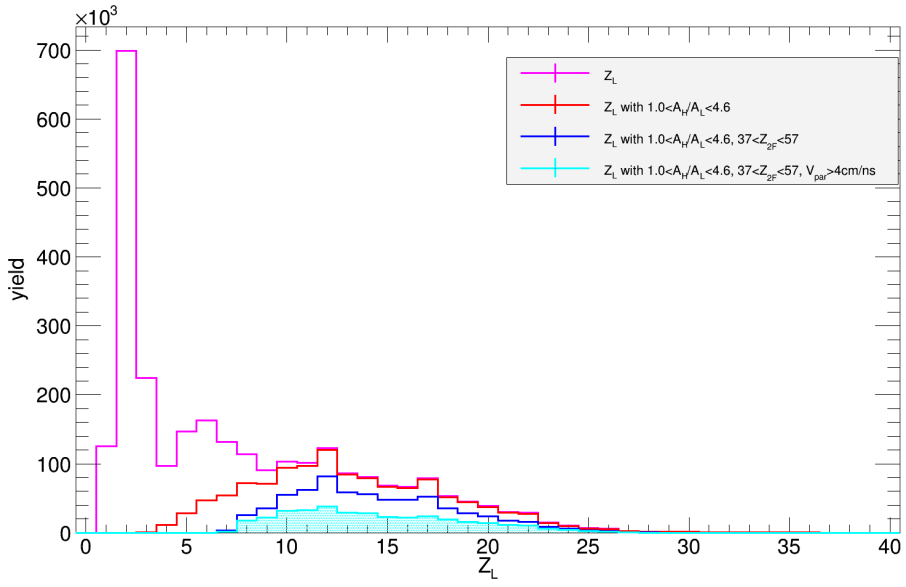

Figure 4.10: Distribution of Z_L for different selection conditions for $^{124}Xe(35\ AMeV)+^{64}Ni$ system. Specifically, purple line indicates Z_L distribution with only event selection (Z_{tot} and M_c); red line indicates Z_L distribution requiring also $1.0 < A_{Heavy}/A_{Light} < 4.6$; blue line indicates Z_L distribution requiring also $37 < Z_{2F} < 57$; light blue line indicates Z_L distribution requiring also $V_{par}^L > 4\ cm/ns$.

4.9 and 4.10, respectively. To eliminate TLF originating fragments, the distributions of

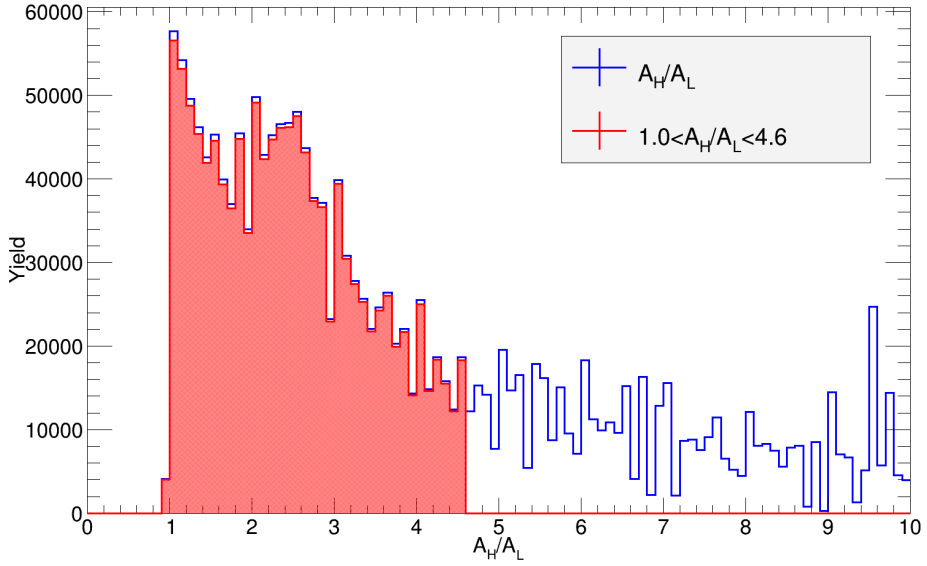

Figure 4.11: Distribution of mass ratio of the two heaviest selected fragments A_{Heavy}/A_{Light}; red area indicates the range in which the mass ratio was selected.

the number of counts as a function of Z_{2F} (sum of the charge of the two heaviest fragments $Z_{2F} = Z_H + Z_L$) and the parallel to the beam velocity component (in the laboratory reference frame) of the lighter of the two fragment V^L_{par}, for the two systems ($^{124}Xe(35\ AMeV)+^{64}Ni$ (fig. 4.12) and $^{124}Xe(35\ AMeV)+^{64}Zn$ (fig. 4.13)) are considered (only the results for Light fragments are presented because the same kind of plots for the Heavy fragment shows that its parallel to the beam velocity component V^H_{par} was always close to the beam velocity). The nine panels of each figures correspond to three selections of mass asymmetries A_H/A_L (columns) and three ranges of the total kinetic energy of the two selected fragments $E_{2F} = E_H + E_L$ (rows). In particular, this quantity (E_{2F}) (shown in figure 4.14 for different selection conditions) is related to the total kinetic energy loss (and centrality of collision) and it's easily accessible in these measurements, whereas determination of the *total* kinetic energy loss requires complete recording and reconstruction of events. At this beam energy, the majority of the energy loss is caused by the loss of fragment mass owing to emission of light fragments and neutrons. Nevertheless, the microscopic transport model calculations [34] show that E_{2F} can be used as a measure of collision violence during the projectile-target collision step of the reaction.

Specifically, in figures 4.12 and 4.13 energy dissipation-collision violence increases from lower row (lower dissipation) to upper row (bigger dissipation) while mass asymmetry A_H/A_L decreases from leftmost column (asymmetric splitting) to rightmost column (almost symmetric splitting). The velocities of the lighter (of the two heaviest) have broad distributions consisting basically of two main components: one of very low velocity (about

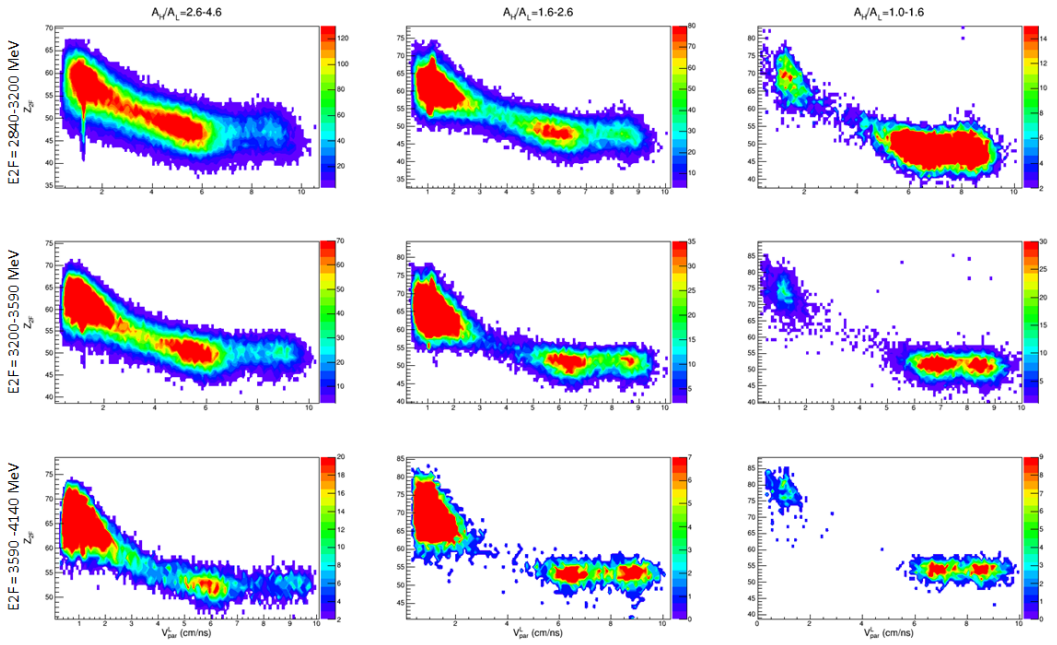

Figure 4.12: Distribution of the sum of charges of the two heaviest fragments (Z_{2F}) vs the lighter fragment parallel velocity (in the laboratory reference frame), for different mass asymmetries A_H/A_L, and different ranges of total kinetic energy of the two selected fragments $E_{2F} = E_H + E_L$, for the $^{124}Xe(35\ AMeV)+^{64}Ni$ system.

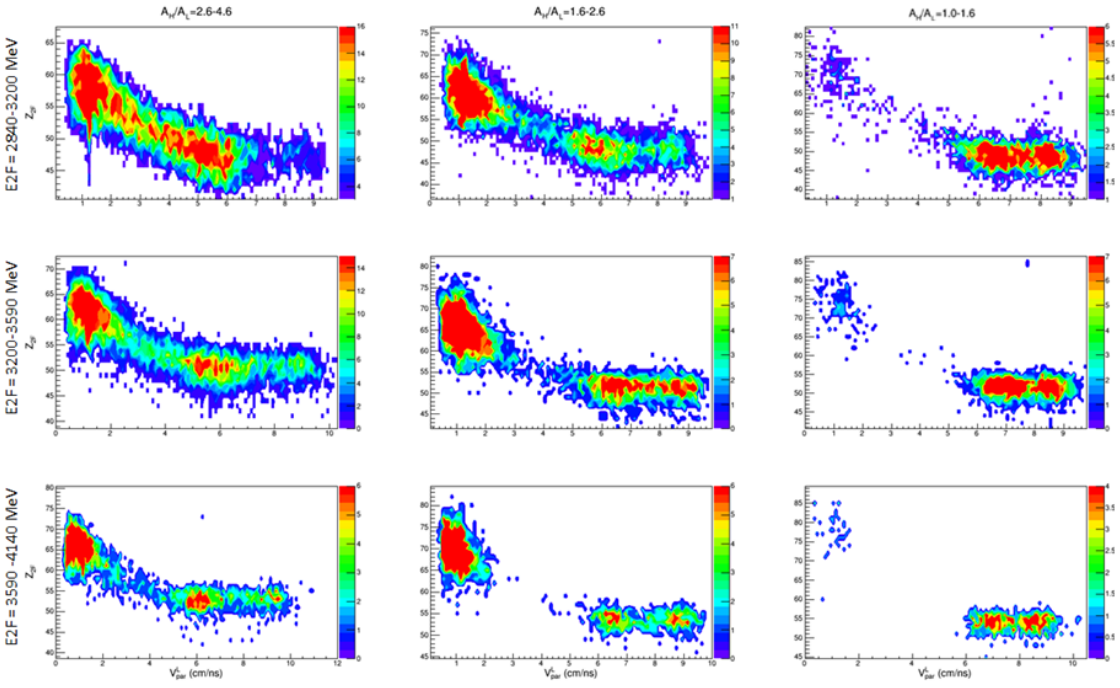

Figure 4.13: Distribution of the sum of charges of the two heaviest fragments (Z_{2F}) vs the lighter fragment parallel velocity (in the laboratory reference frame), for different mass asymmetries A_H/A_L (columns), and different ranges of total kinetic energy of the two selected fragments $E_{2F} = E_H + E_L$ (rows), for the $^{124}Xe(35\ AMeV)+^{64}Zn$ system.

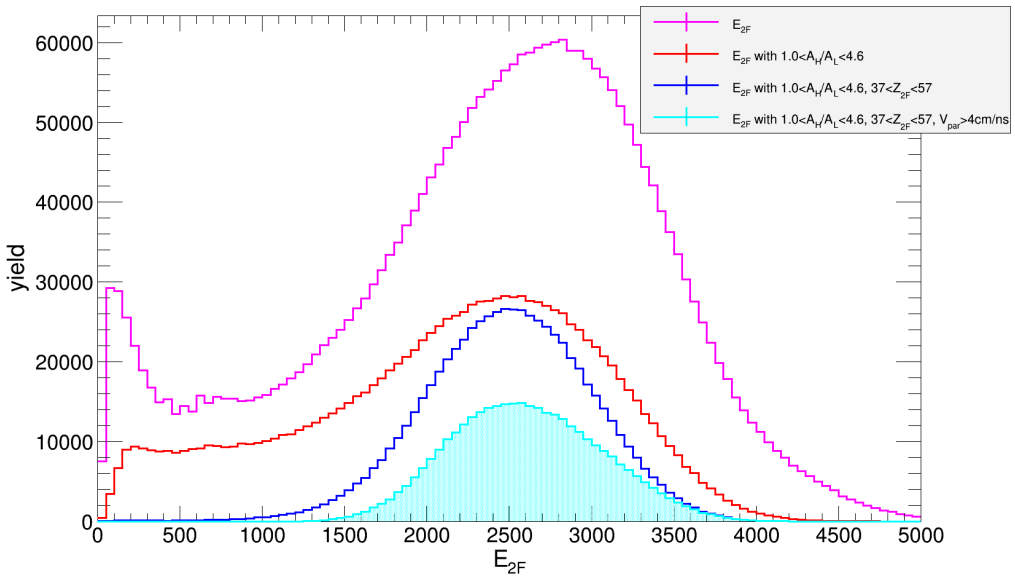

Figure 4.14: Distribution of E_{2F} for different selection conditions for $^{124}Xe(35\ AMeV)+^{64}Ni$ system. Specifically, purple line indicates E_{2F} distribution with only event selection (Z_{tot} and M_c); red line indicates E_{2F} distribution requiring also $1.0 < A_{Heavy}/A_{Light} < 4.6$; blue line indicates E_{2F} distribution requiring also $37 < Z_{2F} < 57$; light blue line indicates E_{2F} distribution requiring also $V^L_{par} > 4\ cm/ns$.

1-2 cm/ns) and the second one close to the beam velocity ($V_{beam} = 8\ cm/ns$). Low-velocity fragments can be interpreted as target remnants, in agreement with the binary character of semi-peripheral reactions at Fermi energies, as also suggested by calculations of ref. [34] and [67]. The high-energy group has Z_{2F} close to about 45-55: this suggests that for $V^L_{par} > 4\ cm/ns$ a splitting of the PLF into two main fragments is essentially observed. As it's possible to see in figures 4.12 and 4.13, to cut low velocity TLF originating fragments, is useful a selection on Z_{2F} close to the Z of projectile. In particular, to do this, a reasonable Z_{2F} cut, for various E_{2F} and mass asymmetries A_H/A_L gates considered, is $37 \leq Z_{2F} \leq 57$. The value of 57 as upper limit of Z_{2F} is chosen considering the Z_{2F} distributions for $^{124}Xe +^{64} Zn$ and $^{124}Xe +^{64} Ni$ systems (fig. 4.15), with a selection on parallel to beam velocity component of the Light fragments $V^L_{par} > 4\ cm/ns$. Z_H and Z_L distributions corresponding to all these conditions are identified by the light blue regions of figures 4.9 and 4.10, respectively. Moreover, figure 4.16 shows Z_H vs. Z_L distribution for different selection conditions; specifically, panel d) presents Z_H vs. Z_L distribution obtained with all the conditions used up to now to select dynamical fission events. As already said, the quantity E_{2F} is used as selector of collisions violence. In order to select almost equal collision violence between the two experiments (InKiIsSy and REVERSE), energy intervals corresponding to equal E_{2F}/Z_{2F} values have been selected. Specifically, this condition is obtained increasing E_{2F} gates of $\sim 140\ MeV$ for the systems studied dur-

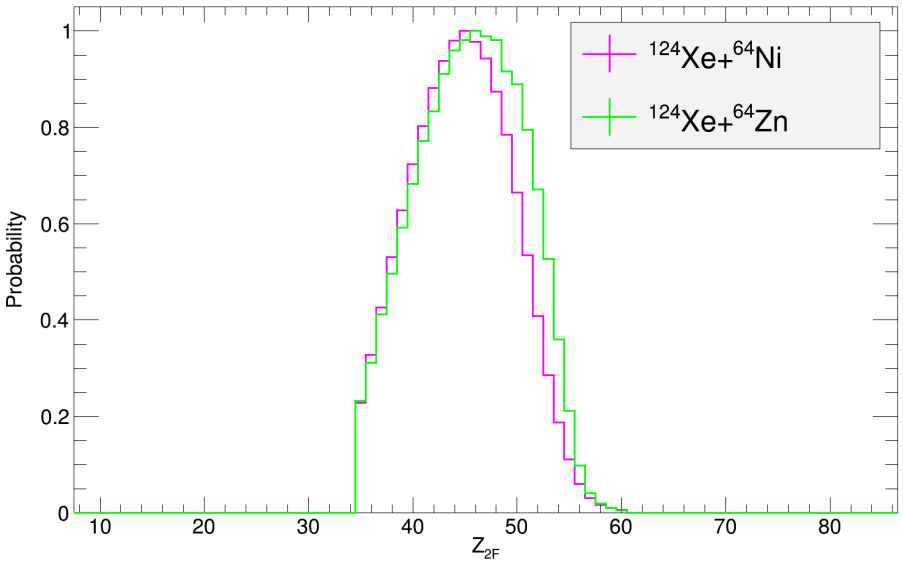

Figure 4.15: Distribution of the sum of charges of the two selected fragments ($Z_{2F} = Z_H + Z_L$) for $^{124}Xe(35\ AMeV)+^{64}Zn$ (green line) and $^{124}Xe(35\ AMeV)+^{64}Ni$ (pink line) systems (see the text for more details).

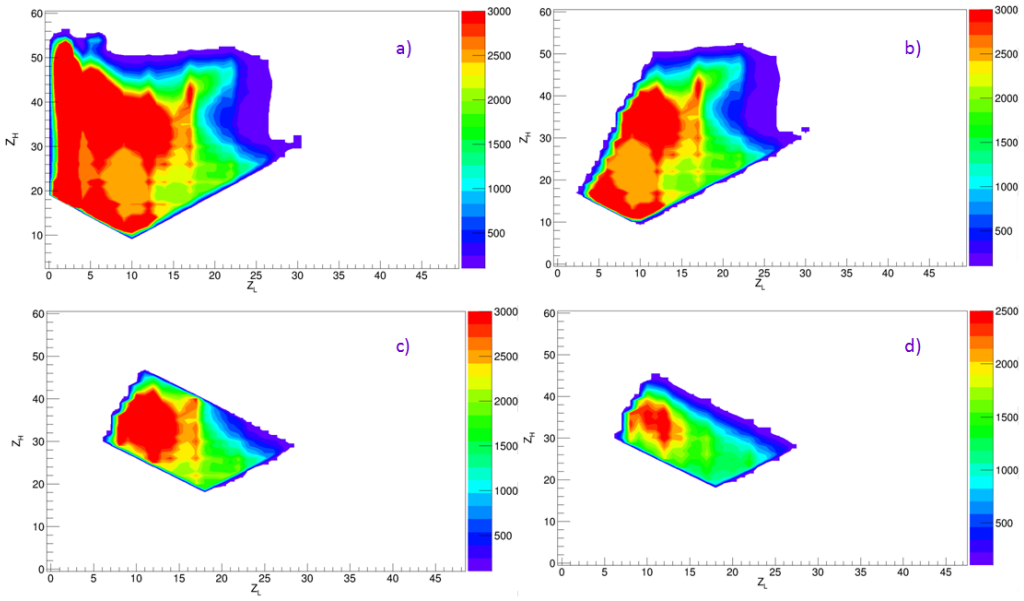

Figure 4.16: Distribution of Z_H vs. Z_L for different selection conditions for $^{124}Xe(35\ AMeV)+^{64}Ni$ system. Specifically panel a) indicates Z_H vs. Z_L distribution with only event selection (Z_{tot} and M_c); panel b) indicates Z_H vs. Z_L distribution requiring also $1.0 < A_{Heavy}/A_{Light} < 4.6$; panel c) indicates Z_H vs. Z_L distribution requiring also $37 < Z_{2F} < 57$; panel d) indicates Z_H vs. Z_L distribution requiring also $V^L_{par} > 4\ cm/ns$.

ing InKiIsSy experiment with respect to the ones of REVERSE experiment. The analysis has been limited to the less dissipative collisions with $E_{2F} > 2840\ MeV$, also in order to avoid to select more dissipative events with more than two IMF (and PLF) in the final state.

4.3 Velocity distribution

After the selection of these events, it's very important to better understand the scenario of PLF break-up considering the V_{par} vs. V_{per} Galilean invariant cross section $\frac{d^2\sigma}{v_\perp dv_\perp dv_\parallel}$, where V_{par} is the velocity component along the beam direction, while V_{per} is the orthogonal one, as measured in the laboratory reference system; fragment velocities were determined using TOF method. In particular, in figure 4.17 the V^H_{par} vs. V^H_{per} invariant cross-section plots of the Heavy fragments in $^{124}Xe + ^{64}Ni$ reaction, for different ranges of mass asymmetry (A_H/A_L) and kinetic energy loss (E_{2F}) are presented. These distribution show that the heaviest of the two selected fragments is always the main PLF remnant; in fact, it has atomic number $Z >\sim 25$ and velocity component parallel to the beam axis around beam velocity ($V_{beam} = 8.0\ cm/ns$). Figure 4.18 presents, instead, the V^L_{par} vs. V^L_{per} invariant

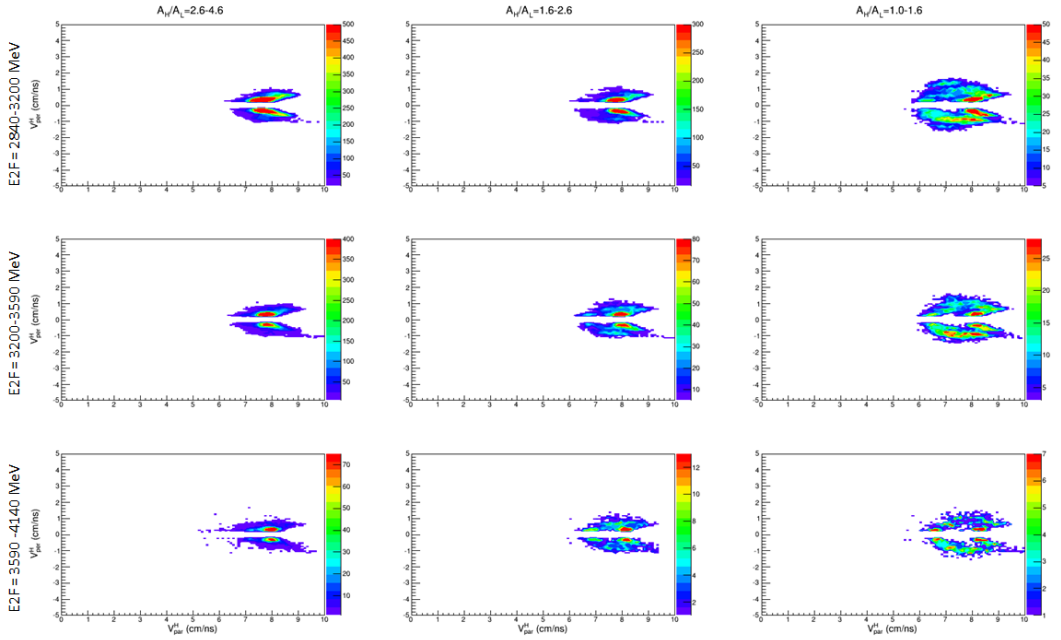

Figure 4.17: V^H_{par} vs. V^H_{per} invariant cross-section plots of the Heavy fragments in $^{124}Xe + ^{64}Ni$ reaction, for different ranges of mass asymmetry (A_H/A_L) and kinetic energy loss (E_{2F}).

cross-section plots of the Light of the two selected fragments for $^{124}Xe + ^{64}Ni$ reaction, always for different ranges of mass asymmetry (A_H/A_L) and kinetic energy loss (E_{2F}). In all panels of fig. 4.18 the characteristic "Coulomb rings" centered slightly below the beam

velocity are present. The presence of these rings points to PLF as a well-defined decay

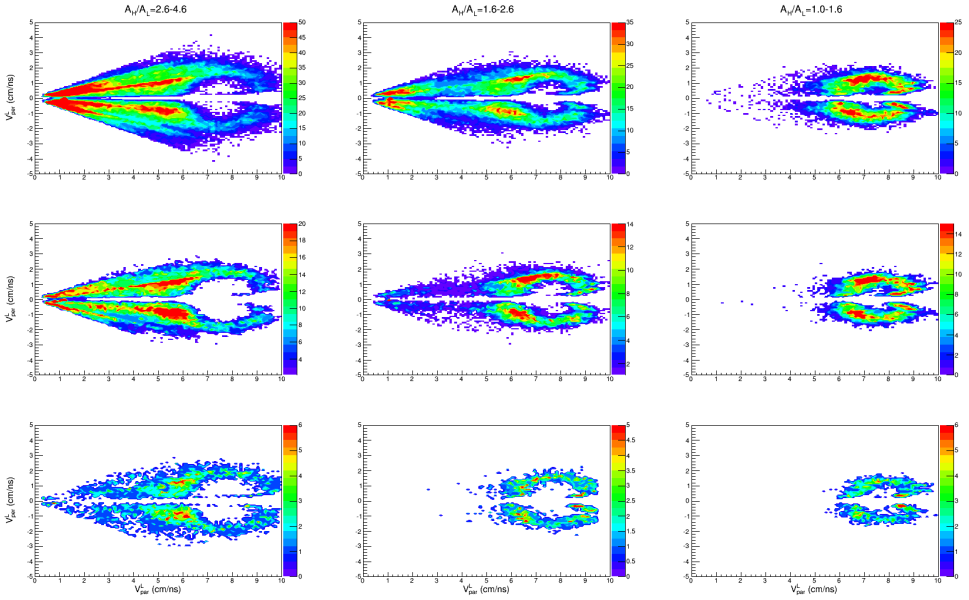

Figure 4.18: V^L_{par} vs. V^L_{per} invariant cross-section plots for the lightest (of two heaviest) fragments in $^{124}Xe + ^{64}Ni$ reaction, for different ranges of mass asymmetry (A_H/A_L) and kinetic energy loss (E_{2F}).

source and suggests the scenario of two separate reaction steps: scattering of PLF followed by its splitting into two fragments. Specifically, for almost symmetric splitting after less dissipative collisions (lower right panel of fig. 4.18) a well defined ring is observed. In this case, Light fragments distribution are forward/backward symmetric, that is, the Light fragment has equal probability to be emitted forward or backward in the reference frame of the PLF source. This result is characteristic of statistical (equilibrated) fission, in which PLF scission is expected to occur a long time ($\sim 10^{-20}$ s or more) after the preceding binary step in which the PLF + TLF system was produced. Thus, statistical fission takes place after a number of PLF rotations and equilibrated PLF doesn't keep memory of the previous reaction step. As just seen for REVERSE experiment (section 1.2.1), for more dissipative collisions and/or more asymmetric splits, instead, the population of the Coulomb ring is no longer forward/backward symmetric. In this case, the lighter fragments populate preferentially the low velocity side of the Coulomb ring, which means that they are backward-emitted in the PLF reference frame, i.e. toward the TLF, around $V_{par} \approx 1$ cm/ns. This observed forward/backward asymmetry is the main signature of "Dynamical Fission"; it indicates that PLF fission-like splitting is a fast process. However a forward/backward symmetric component is still present: the distributions are consistent with a superposition of a forward/backward symmetric component and an asymmetric one.

The same plots for $^{124}Xe + ^{64}Zn$ reaction (fig. 4.19) look similarly to those corresponding to $^{124}Xe + ^{64}Ni$ system and therefore they indicate the same reaction mechanisms. In

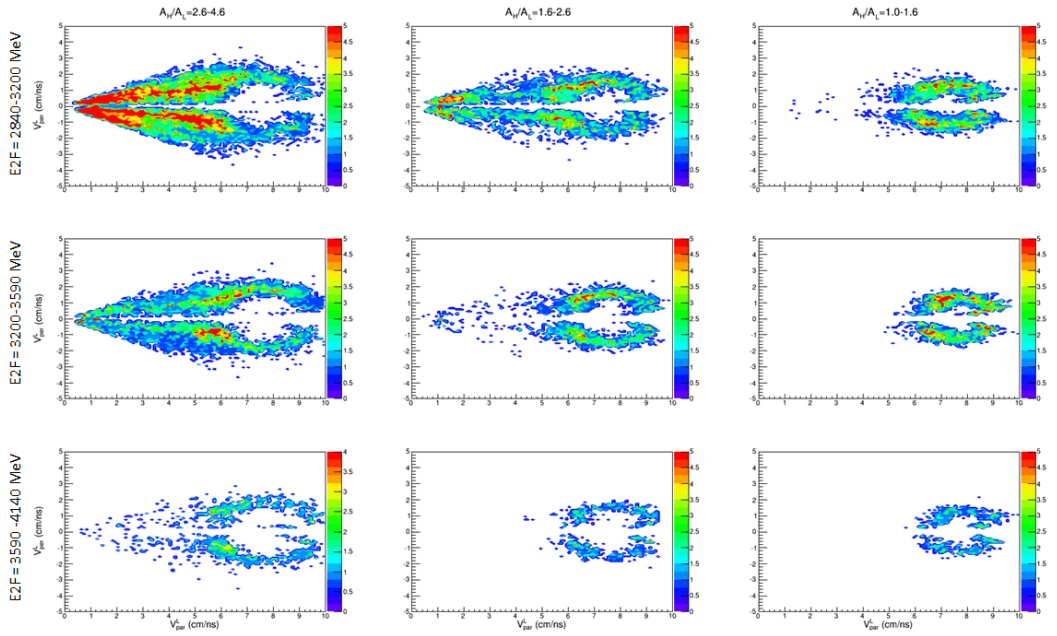

Figure 4.19: V^L_{par} vs. V^L_{per} invariant cross-section plots for the lightest (of two heaviest) fragments in $^{124}Xe + ^{64}Zn$ reaction, for different ranges of mass asymmetry (A_H/A_L) and kinetic energy loss (E_{2F}).

both figures, fragments with $V^L_{par} < 3\ cm/ns$ can be interpreted as target remnants, in agreement with model calculations [34]. Mid-velocity emission of light IMFs ($A_H/A_L \sim 4$) has been well described as "neck emission", related to fast neck fragmentation processes at times of 40-100 fm/c after beginning of re-separation between PLF and TLF [1, 34]. To better understand the scenario of PLF break-up, it's important to analyze the angular distributions of PLF decaying fragments. But, before calculating them, events with $V^L_{par} > 4\ cm/ns$ have been selected; in this way, a possible contribution to angular distribution of fragments originating from TLF is strongly reduced.

4.4 Angular distributions

In order to estimate the weight of the statistical and dynamical contribution, also in this case, the $cos(\theta_{prox})$ distributions for different mass asymmetry (A_H/A_L) and kinetic energy loss (E_{2F}) (fig. 4.20) have been extracted. The nine panels of figure 4.20 correspond to the three selections of mass asymmetries A_H/A_L (columns) and the three ranges of the total kinetic energy of the two selected fragments $E_{2F} = E_H + E_L$ (rows). In particular, for almost symmetric splitting after less dissipative collisions, the $cos(\theta_{prox})$ angular dis-

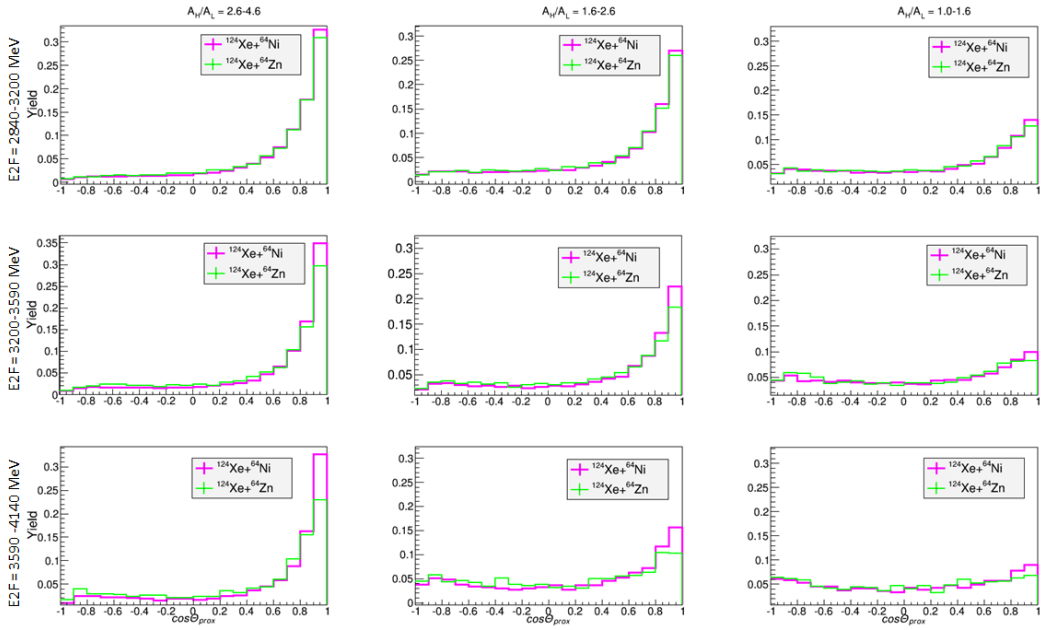

Figure 4.20: $cos(\theta_{prox})$ angular distributions for $^{124}Xe(35AMeV) +^{64} Ni$ (pink line) and $^{124}Xe(35AMeV) +^{64} Zn$ (green line) reactions. These distribution have been evaluated for different ranges of mass asymmetry A_H/A_L (columns) and different ranges of the total kinetic energy $E_{2F} = E_H + E_L$ (rows).

tributions are symmetrical with respect to $cos(\theta_{prox}) = 0$, typical of a standard fission of a rotating nucleus. Increasing mass asymmetry (bigger A_H/A_L) and/or energy dissipation (lower E_{2F}), the distributions present a peak at $cos(\theta_{prox}) = 1$, which indicates dynamical fission process. Specifically, comparing the two reactions ($^{124}Xe+^{64} Zn$ and $^{124}Xe+^{64} Ni$), it results that the dynamical component is stronger for the system with the neutron rich target. This result is similar to the one obtained in the REVERSE experiment but in this case the two systems are isobaric, with only different target. It indicates that the observed effect has to be related to the different isospin of the systems rather than to the initial size. From $cos(\theta_{prox})$ distributions, the relative contributions of statistical and dynamical components, for each selection, are estimated applying the method described in section 1.2.1. In particular, in tab. 4.1 the percentages associated to the dynamical component mechanism, as a function of mass asymmetry and energy dissipation, for the four systems studied during REVERSE ($^{124}Sn +^{64} Ni$ (red values) and $^{112}Sn +^{58} Ni$ (blue values)) and InKiIsSy experiments ($^{124}Xe +^{64} Ni$ (pink values) and $^{124}Xe +^{64} Zn$ (green values)) are presented, evaluated using the same angular coverage of the InKiIsSy setup. From this comparison results that dynamical component weight scale with the N/Z ratio of the system. Figures 4.21 and 4.22 present Dynamical component as a function of $(\frac{N-Z}{N+Z})^2$ and $\frac{N}{Z}$, respectively. In both figures it's possible to see as dynamical component varies with

DYN (%)	^{124}Sn+^{64}Ni; ^{112}Sn+^{58}Ni ^{124}Xe+^{64}Ni; ^{124}Xe+^{64}Zn		
	A_H/A_L		
E_{2F} (MeV)	2.6 - 4.6	1.6 - 2.6	1.0 - 1.6
2700 - 3060 2840 - 3200	73.8 ; 63.1 71 ; 67	56.3 ; 39.3 51 ; 45	21 ; 11.2 18 ; 14
3060 - 3450 3200- 3590	68.4 ; 49 63 ; 51	40.9 ; 16.8 31 ; 20	7.9 ; <5 7.1 ; <5
3450 - 4000 3590 – 4140	56.8 ; 36.2 54 ; 36	25.4 ; 12.6 13; 11	<5 ; <5 <5 ; <5

Table 4.1: Percentage associated to the Dynamical component mechanism for the four systems studied during the REVERSE ($^{124}Sn+^{64}Ni$ and $^{112}Sn+^{58}Ni$) and the InKiIsSy ($^{124}Xe+^{64}Zn$ and $^{124}Xe+^{64}Ni$) experiments.

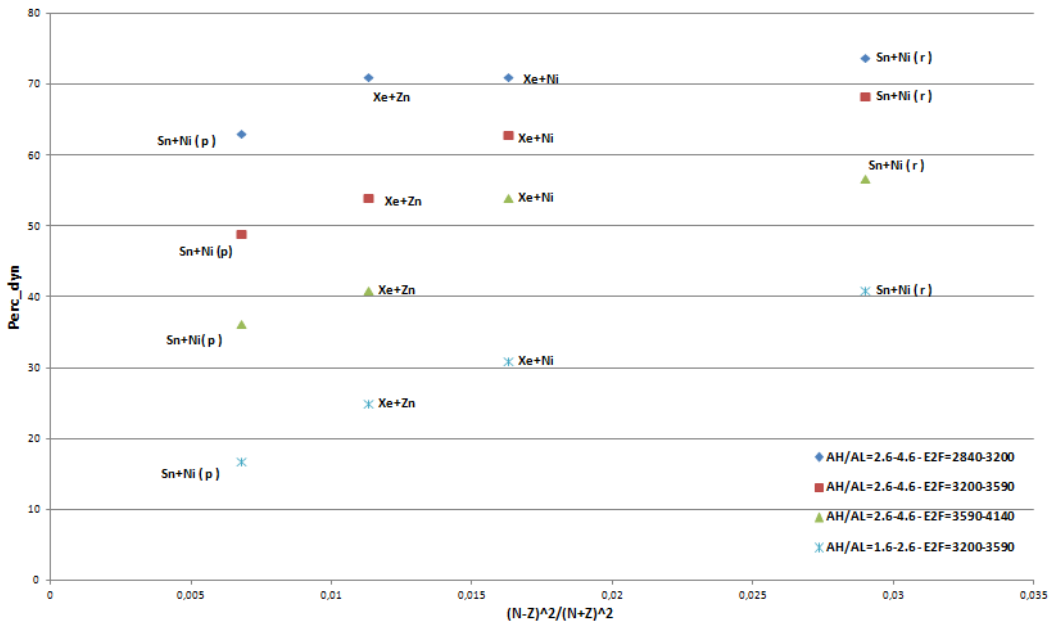

Figure 4.21: Dynamical component as a function of $(\frac{N-Z}{N+Z})^2$ for the systems studied during REVERSE and InKiIsSy experiments for different mass asymmetry and energy dissipation.

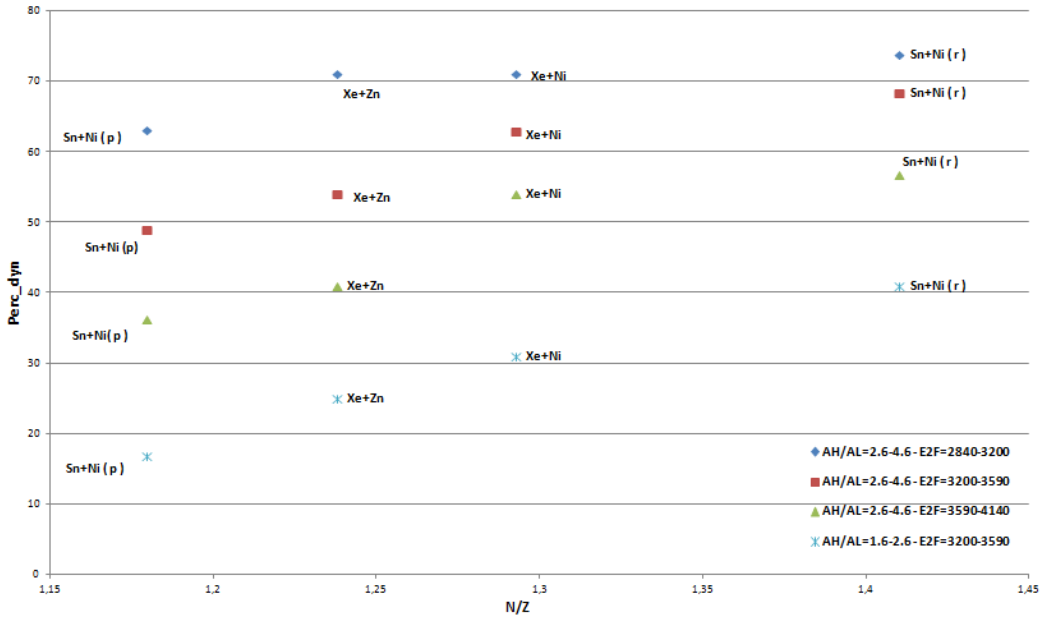

Figure 4.22: Dynamical component as a function of $\frac{N}{Z}$ for the systems studied during REVERSE and InKiIsSy experiments for different mass asymmetry and energy dissipation.

regularity with both isospin asymmetry (fig. 4.21) ($(\frac{N-Z}{N+Z})^2$) and N/Z ratio (fig. 4.22).

4.5 Relative velocities

The analysis of relative velocities of the two selected PLF fission-like fragments gives some information on the properties of the Dynamical Fission phenomenon. Specifically, the mean value of the fragment-fragment relative velocity is given by the following formula:

$$|\vec{V}_{rel}(H,L)| = |\vec{V}^H - \vec{V}^L| = \sqrt{(V_x^H - V_x^L)^2 + (V_y^H - V_y^L)^2 + (V_z^H - V_z^L)^2}. \tag{4.3}$$

Figure 4.23 shows the angular distributions of mean value of the fragment-fragment relative velocity, normalized to the velocity resulting from Coulomb repulsion that, given event by event by Viola systematics [17], is equal to:

$$V_{ratio} = \sqrt{\frac{2 \cdot E_k}{\mu}} \tag{4.4}$$

where μ, the reduced mass of the two body system H and L, and E_k, total kinetic energy (from [68, 69]), are given by the following formulas:

$$\mu = \frac{A_H * A_L}{A_H + A_L}, \tag{4.5}$$

$$E_k = \frac{0.755 \cdot Z_1 \cdot Z_2}{A_1^{1/3} + A_2^{1/3}} + 7.3[MeV], \tag{4.6}$$

this last value is assumed as an evaluation resulting from fit to several experimental data, for the most probable total kinetic energy E_k release in fission. In fact, some studies have shown that the total kinetic energy carried out by the two fission fragments can be described by a systematic evaluation based on the Coulomb repulsion between two prolate spheroids. According to this evaluation $< E_k >$ depends linearly on $\frac{Z^2}{A^{1/3}}$, the Coulomb parameter of the fissioning nucleus. The coefficients derived from a least-squares fit to several experimental data can be associated with the separation distance between the charge centres of the two fragments at the onset of the acceleration and the deformation of the fragments [17].

Since in sequential emission of PLF fission fragments total kinetic energy release will

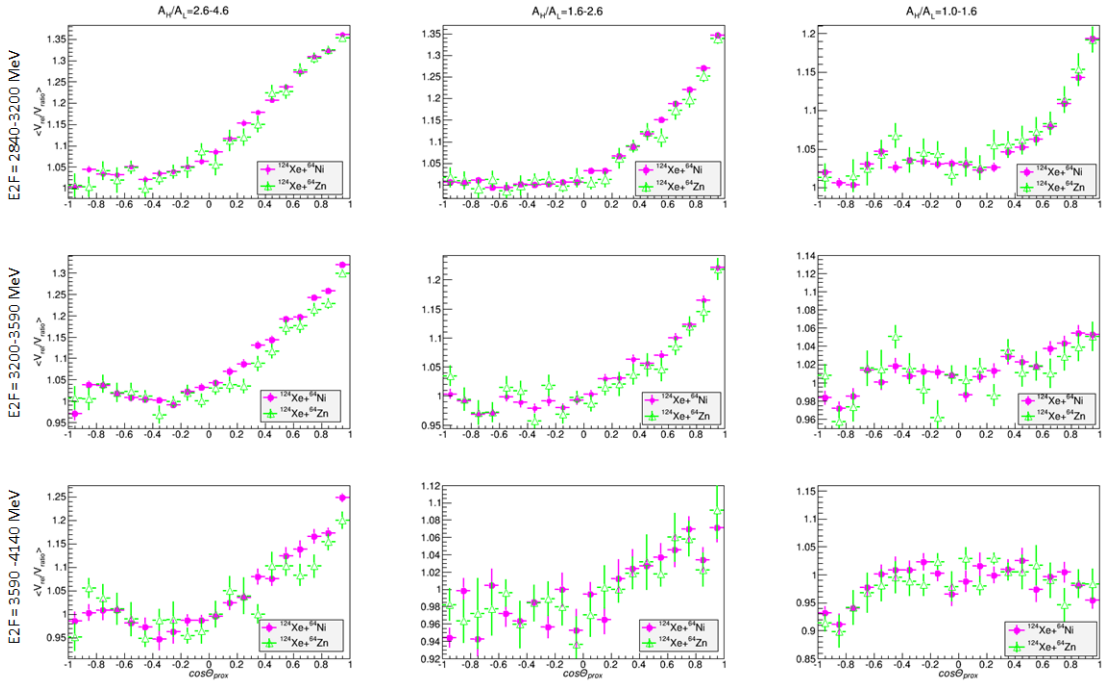

Figure 4.23: Mean value of the fission-like fragments relative velocity normalized by Viola systematic (V_{ratio}) as a function of $cos(\theta_{prox})$ for $^{124}Xe(35AMeV) + ^{64}Ni$ (pink circles) and $^{124}Xe(35AMeV) + ^{64}Zn$ (green triangles) reactions. These distribution have been evaluated for different ranges of mass asymmetry A_H/A_L (columns) and different ranges of the total kinetic energy $E_{2F} = E_H + E_L$ (rows).

be mainly governed by Coulomb repulsion, the "equilibrated" PLF fission should result in a V_{rel}/V_{ratio} distribution around $V_{rel}/V_{ratio} = 1$. As it's possible to see in figure 4.23, for almost symmetric splitting after less violent collisions, the predictions based on Viola systematic confirm angular distribution observations, that is a statistical fission scenario. Instead, in the other cases (asymmetric splitting or almost symmetric splitting after more violent collisions) the predictions based on the systematic established for equilibrium fis-

sion reproduce the experimental data only for those configurations resulting in $cos(\theta_{prox})$ values smaller than $\sim$ zero, while for the "dynamical" events ($cos(\theta_{prox}) \sim 1$) the most probable relative velocity is higher up to some 25% than the Viola systematic. Specifically, increasing the weight of the dynamical component, the most probable velocity values increases and the relative velocities distributions become wider (not shown here). The observation of this deviation from equilibrium fission systematic, behavior observed also in the light IMFs neck-like emission mechanism [1, 34], is compatible with a non equilibrated velocity field of the PLF before undergoing the fission-like step.

4.6 Dynamical and statistical IMF production

Also for InKiIsSy experiment, IMFs production cross sections in semi - peripheral reactions have been evaluated for dynamical and statistical emission, applying the analysis method described in ref. [3]. The previous analysis has been extended by enlarging by about a factor 2 the impact parameter window of the collision toward more dissipative collisions, evaluating cross section of the observed IMFs from atomic number $Z = 3$ up to $Z = 22$. In this case, the events have been selected by requiring a PLF residue having atomic number $Z >\sim 22$ (see fig. 4.6) and parallel velocity with respect to the beam axis (in laboratory reference frame) $V_{par} >\sim 6\ cm/ns$. The same condition of REVERSE experiment (see section 1.2.1), in which the events selected were those with reduced impact parameter $b_{red} \geq 0.4$ (corresponding to $M_c \leq 10$), is obtained with the condition $M_c \leq 8$. In order to disentangle dynamical and statistical IMF emission from PLF source, the case of IMF multiplicity equal to one is selected. In fact, in this case of ternary emission, relative-energy kinematic correlation method [1] has shown high sensitivity with respect to the different phase of the reaction (from dynamical decay to sequential one), allowing to estimate the contribution of the different mechanisms. To do this, the IMFs emitted from TLF having velocity component parallel to the beam axis smaller than 3 cm/ns have been removed by rejecting the case of the relative velocity between PLF and IMF, $V_{rel}(PLF, IMF)$, larger than 1.5 times the relative velocity due to mutual PLF-IMF Coulomb repulsion, V_{Viola}, evaluated using the Viola systematics [17]. The choice of this cut has been guided by the previous analysis of ref. [1] on the relative correlations between IMF and PLF or IMF and TLF.

Figure 4.24 presents the IMF multiplicity distribution obtained applying such selection for the four systems studied during REVERSE ($^{124}Sn +^{64} Ni$ and $^{112}Sn +^{58} Ni$) and InKiIsSy ($^{124}Xe +^{64} Zn$ and $^{124}Xe +^{64} Ni$) experiments at 35 $AMeV$ beam energy evaluated using the same angular coverage of the InKiIsSy setup and corrected for detection efficiency.

In particular, IMF emission probability increases with the increase of the isospin content, while binary events (IMF multiplicity = 0) are more probable in the system with a lower N/Z ratio. Moreover for the reactions studied during the InKiIsSy experiment it's possible to observe a decrease of this relative probability of events with no IMF emission with respect to REVERSE experiment data presented in ref. [3]. The difference arises from the fact that in the current analysis only fragments having $\theta_{lab} > 1.8^o$ are included; thus, very peripheral-low dissipation collision included in previous analysis [3] are not present here.

For data satisfying the condition

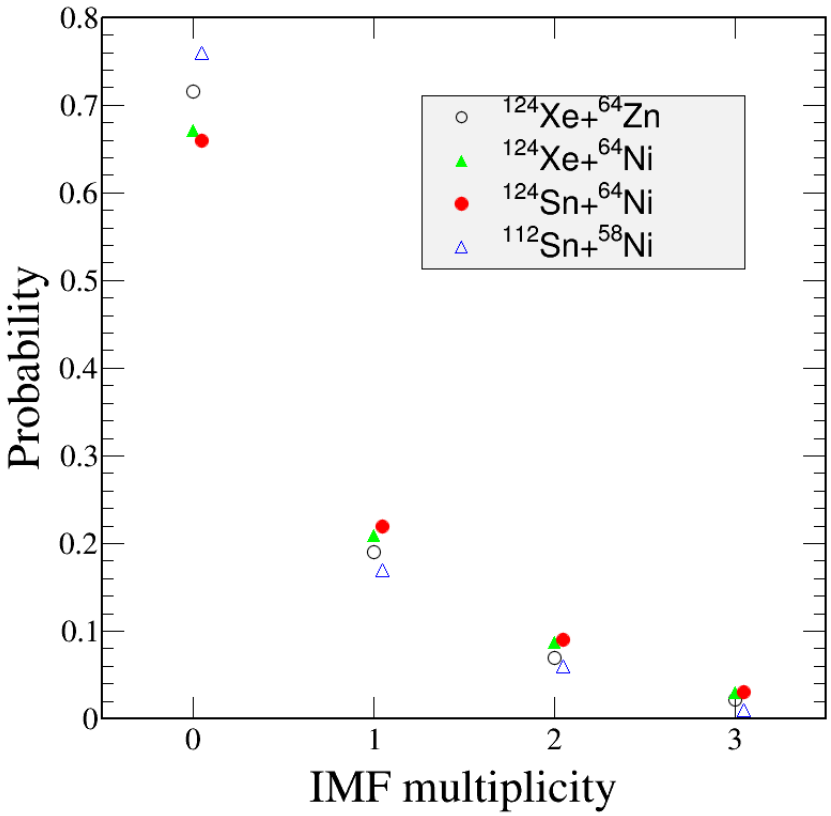

Figure 4.24: Probabilities of different IMF multiplicities (in coincidence with PLF residues) normalized to the number of selected events the four systems studied during REVERSE (^{124}Sn+^{64}Ni (full circles) and ^{112}Sn +^{58} Ni (empty triangles)) and InKiIsSy (^{124}Xe +^{64} Zn (empty circles) and ^{124}Xe +^{64} Ni (full triangles)) experiments.

$$V_{rel}(PLf, IMF)/V_{Viola} \leq 1.5, \tag{4.7}$$

the V_{par} vs. V_{per} Galilean invariant cross section for the lighter fragment in the PLF source reference frame is shown in figure 4.25, for different mass asymmetry. Specifically, left panel of fig. 4.25, relative to the most asymmetric splittings ($2.6 < A_H/A_L < 4.6$), shows clearly a forward-backward asymmetry characteristic of dynamical fission. Instead, in the right panel of fig. 4.25, relative to symmetric splittings ($1.0 < A_H/A_L < 1.6$), a

forward-backward symmetry around a well defined Coulomb ring is observed, typical of a equilibrated break-up. To evaluate quantitatively the dynamical and statistical component

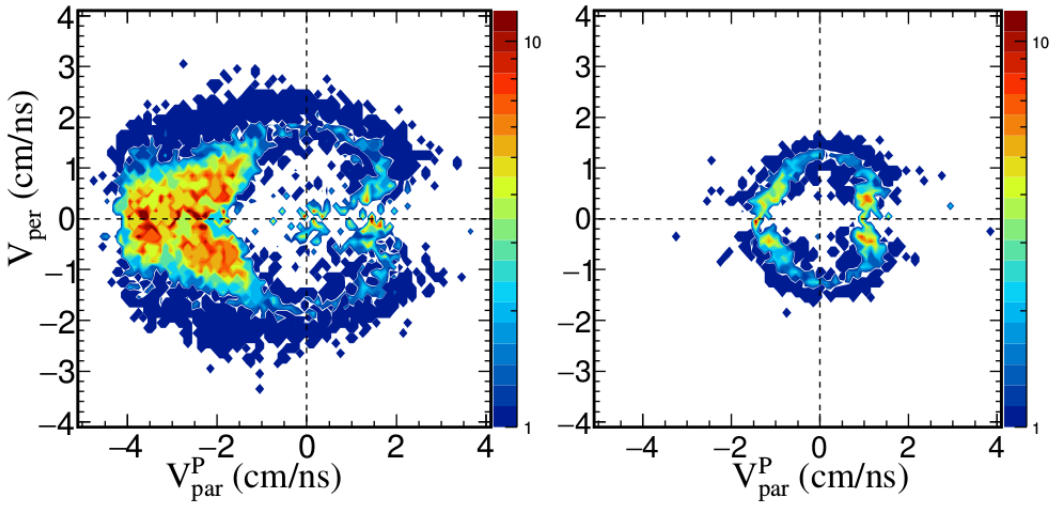

Figure 4.25: Invariant cross section for the lighter fragment in the reference frame of the PLF source for $2.6 < A_H/A_L < 4.6$ (left panel) and $1.0 < A_H/A_L < 1.6$ (right panel).

emission as a function of the charge of the emitted fragments, the $cos(\theta_{prox})$ distribution is used.
Thus, the most important points of this analysis are:

- the selection of events in which the IMF multiplicity is strictly equal to one;
- the rejection of events in which IMF originates from TLF fragmentation or decay;
- the dynamical component is obtained subtracting from the total $cos(\theta_{prox})$ distribution the portion of angular distribution that is symmetric around $cos(\theta_{prox}) = 0$ (see section 1.2.1).

Figure 4.26 shows the ratio of the dynamical component with respect to the dynamical+statistical one as a function of the IMF atomic number for the $^{124}Xe +^{64} Ni$ and $^{124}Xe +^{64} Zn$ reactions. In this representation it's possible to see an enhancement of dynamical emission for heavier IMF having $Z >\sim 8$ for the reaction with a neutron rich target (^{64}Ni). This result confirms that the observed effect is related to the different isospin of the two systems; in fact, in this case the two systems are isobaric, so the result is independent from the size of the projectile and target. These data have been also compared with the ones obtained during REVERSE experiment using the same angular coverage of the InKiIsSy setup (fig. 4.27). It results that dynamical component in the IMF emission scales with the isospin of the entrance channel.

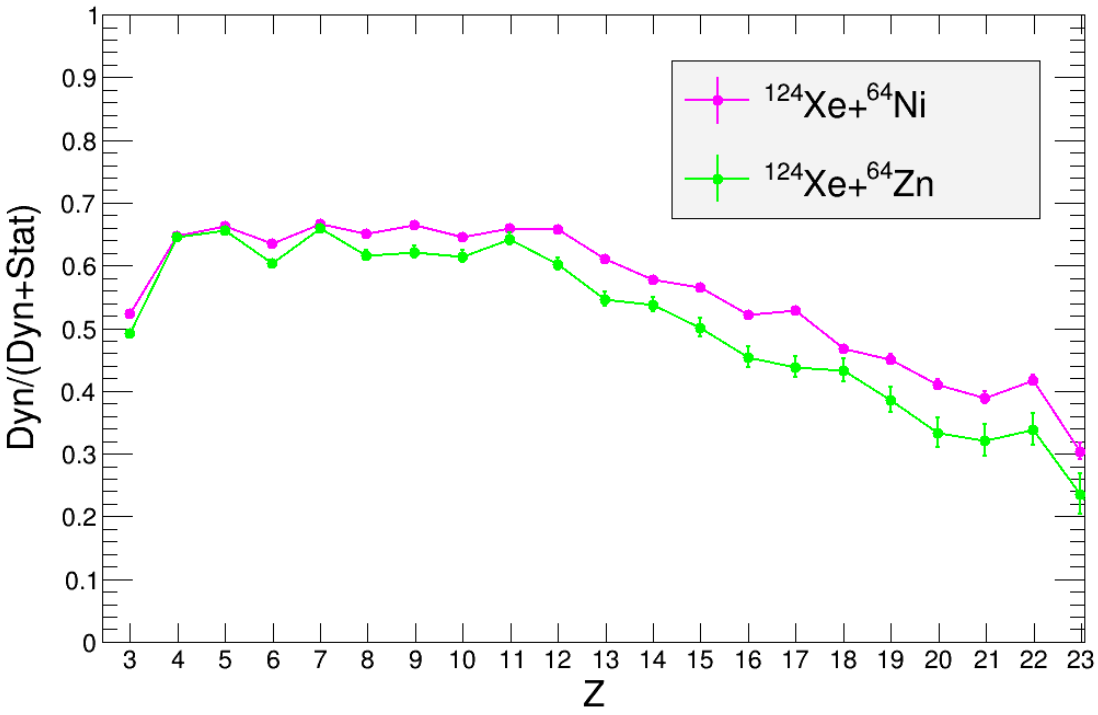

Figure 4.26: Ratio of the dynamical component vs. the total (statistical + dynamical) as a function of the IMF atomic number for the $^{124}Xe +^{64} Ni$ (pink line) and $^{124}Xe +^{64} Zn$ (green line) reactions.

4.7 N/Z isotopic distributions

In a different analysis, a careful study of the ternary events has been also performed. For these events selection, a complete event reconstruction is required, specifically the simultaneous detection of PLF TLF and IMF. Considering figure 4.4, the chosen events are those with $Z_{tot} > 60$ and total particles longitudinal momentum equal to at least 60% of the projectile momentum. In order to obtain more informations on the correlations between isospin, relative velocities and emission time-scale of IMFs, the average N/Z isotopic distributions for all charges between $Z = 3$ and $Z = 8$ have been determined. Specifically, to evaluate the time-scale of fragment formation, the fragment-fragment relative velocities, $V_{REL}(PLF, IMF)$ and $V_{REL}(TLF, IMF)$ have been calculated. These velocities are normalized to the one corresponding to the Coulomb repulsion, as given by Viola systematics [17]. Figure 4.28 show the correlations between relative velocities (V_{REL}/V_{VIOLA}) of the three fragments (PLF TLF and IMF) with the condition $cos(\theta_{prox}) > 0.8$ (left panel) and $cos(\theta_{prox}) < 0$ (right panel) for $^{124}Xe +^{64} Ni$ system. The conditions $cos(\theta_{prox}) > 0.8$ and $cos(\theta_{prox}) < 0$ have been used to select fragments dynamically and statistically emitted, respectively (see figure 4.20). The $cos(\theta_{prox})$ between PLF and IMF relative velocity (fission axis) has been evaluated with respect to the relative velocity between the PLF+IMF

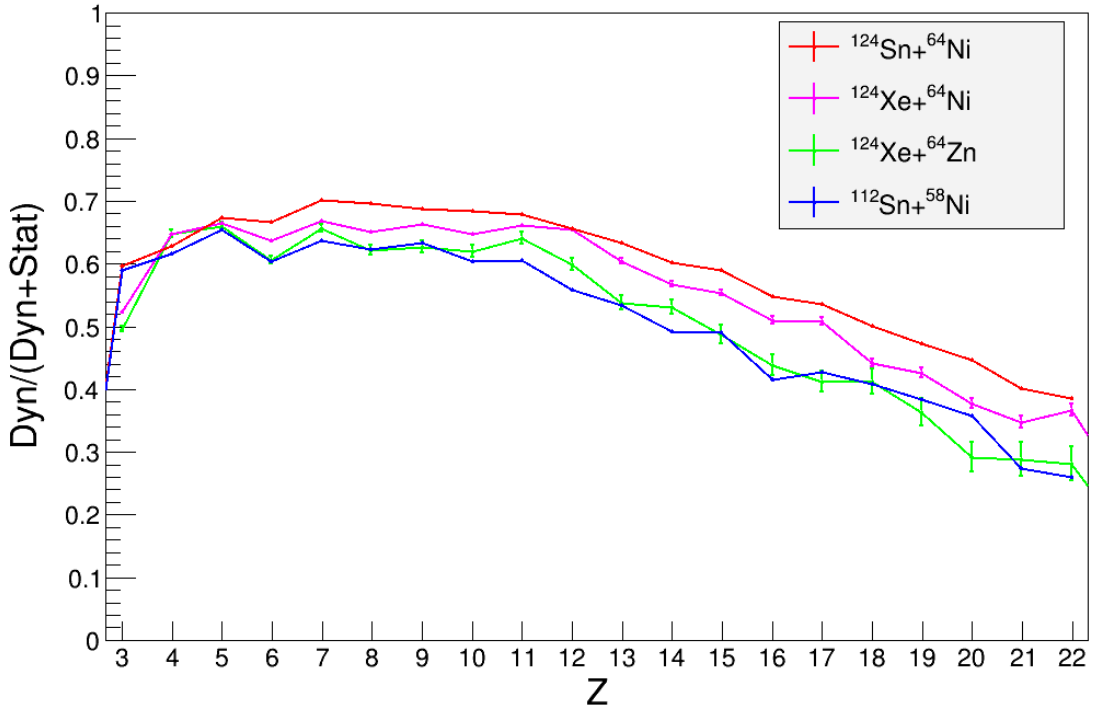

Figure 4.27: Ratio of the dynamical component vs. the total (statistical + dynamical) as a function of the IMF atomic number for the systems studied during REVERSE ($^{124}Sn+^{64}Ni$ (red line) and $^{112}Sn+^{58}Ni$ (blue line)) and InKiIsSy ($^{124}Xe+^{64}Zn$ (green line) and $^{124}Xe+^{64}Ni$ (pink line)) experiments.

(reconstructed center of mass) and the TLF (separation axis). Specifically, considering

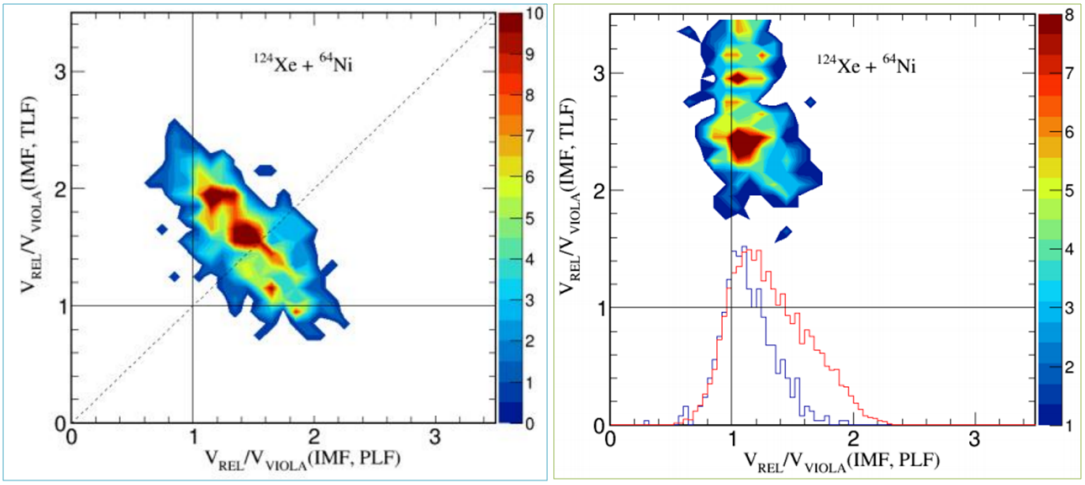

Figure 4.28: Correlations between relative velocities (V_{REL}/V_{VIOLA}) of the three biggest fragments with the condition $cos(\theta_{prox}) > 0.8$ (left panel) and $cos(\theta_{prox}) < 0$ (right panel) for $^{124}Xe + ^{64}Ni$ system, from [66].

these plots (fig. 4.28), events close to the diagonal indicates IMFs of dynamical neck fragmentation (left panel), while events approaching V_{REL}/V_{VIOLA}(IMF,PLF)=1 (right panel) correspond to the sequential split of the primary projectile-like nucleus.
In figure 4.29 the $< N/Z >$ distributions as a function of the IMFs charge Z, for statistical (red squares) and dynamical (black circles) emitted particles for the $^{124}Xe + ^{64}Ni$ reaction are shown. The purpose is to measure the degree of neutron enrichment at midvelocity and to compare it with the one related with the statistical emission from a PLF source. It's possible to observe that the N/Z ratio for dynamically emitted particles shows higher values with respect to the one obtained for statistically emitted particles.
Figure 4.30 presents the $< N/Z >$ distributions as a function of the IMFs charge Z for dynamical emitted particles for the four systems studied during the REVERSE ($^{124}Sn + ^{64}Ni$ and $^{112}Sn + ^{58}Ni$) and the InKiIsSy ($^{124}Xe + ^{64}Zn$ and $^{124}Xe + ^{64}Ni$) experiments. Comparing these distributions, it results that N/Z ratio for dynamically emitted particles presents large values for the systems with higher isospin content of the reaction channel. The neutron enrichment of the mid-velocityIMF has been succesful used to pin down the low density behaviour of the nuclear symmetry energi in ref. [16]. The InKiIsSy data respresents other valuable experimental information to be compared to the simulation codes, as it's planned to do in the future.

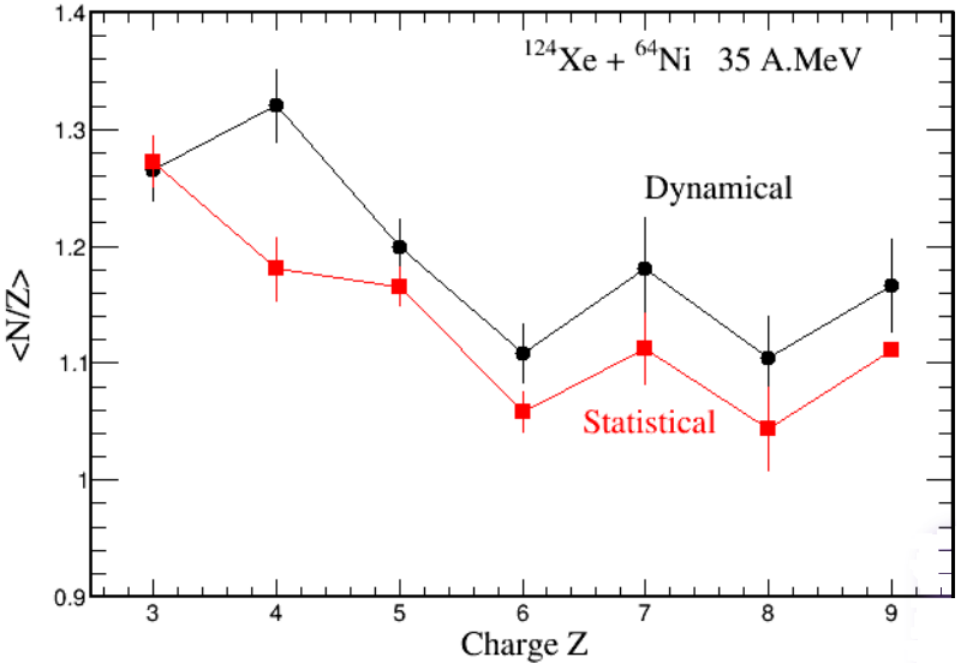

Figure 4.29: $< N/Z >$ distributions as a function of the IMFs charge Z for statistical (red squares) and dynamical (black circles) emitted particles for the $^{124}Xe + ^{64}Ni$ reaction.

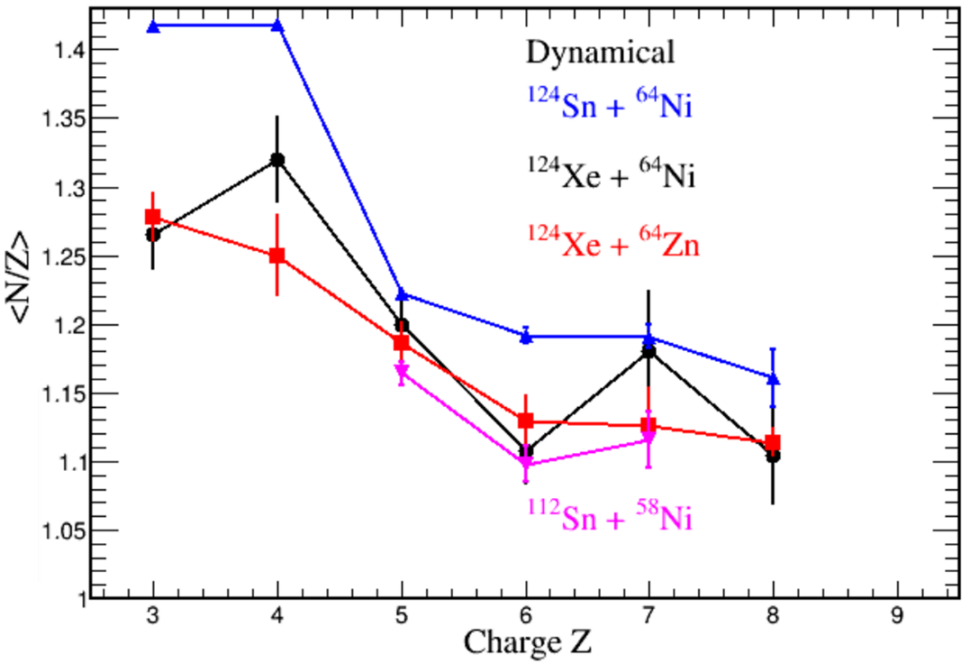

Figure 4.30: $< N/Z >$ distributions as a function of the IMFs charge Z for dynamical emitted particles for the four systems studied during the REVERSE ($^{124}Sn + ^{64}Ni$ (blue line) and $^{112}Sn + ^{58}Ni$ (pink line)) and the InKiIsSy ($^{124}Xe + ^{64}Zn$ (red line) and $^{124}Xe + ^{64}Ni$ (black line)) experiments.

Conclusion

In this work the experimental results of InKiIsSy experiment have been shown. During this experiment, the dynamical and statistical PLF binary decay probability and IMF production in semi-peripheral reactions have been evaluated for the $^{124}Xe(35AMeV) +^{64} Zn(^{64}Ni)$ systems. In previous experiments, the systems $^{124}Sn +^{64} Ni$ and $^{112}Sn +^{58} Ni$ were studied in inverse (REVERSE) and direct (TIMESCALE) kinematics at 35 $AMeV$. The analysis of these two reactions has shown that while the statistical fission assumes the same cross section for the two systems, the dynamical fission probability is enhanced for the neutron rich one. This effect can be related to the different N/Z ratio of the two systems but also to the different size of entrance channel. In order to disentangle these two effects, the $^{124}Xe +^{64} Zn(^{64}Ni)$ reactions have been analyzed at the same bombarding energy. In this case the two systems have same mass and only different Z (and N/Z) for the target. To separate the statistical from the dynamical contribution, the $cos(\theta_{prox})$ distributions have been calculated for different fission-like fragments Heavy/Light mass asymmetry (A_H/A_L) and kinetic energy loss (E_{2F}). It results that for almost symmetric splitting after less dissipative collisions, the $cos(\theta_{prox})$ angular distributions are symmetrical with respect to $cos(\theta_{prox}) = 0$, typical of a standard fission of a rotating nucleus. Increasing mass asymmetry (bigger A_H/A_L) and/or energy dissipation (lower E_{2F}), the distributions present a peak at $cos(\theta_{prox}) = 1$, which indicates the onset of the dynamical fission process. Comparing the two reactions, $^{124}Xe +^{64} Zn$ and $^{124}Xe +^{64} Ni$, it results that the dynamical component is stronger for the system with the neutron rich target. This result is similar to the one obtained in the REVERSE experiment but in this case the two systems are isobaric, with only different target. It indicates that the observed effect has to be related to the different isospin of the systems rather than to the initial size. Moreover, a first comparison of the four systems studied during REVERSE and InKiIsSy experiments, shows that dynamical component weight scale with the N/Z ratio of the system.

Recently, the $^{124}Xe+^{64}Ni$ system has also been investigated with a preliminary theoretical simulation in the frame of the constrained molecular dynamics, CoMD-III, code [72], in order to reproduce both "fast" light IMFs emission and heavy IMFs production in sequen-

tial PLF decay. The obtained results are very preliminary; however the data comparison seems very promising (see Appendix B). In the future there is the possibility to extend these studies at lower beam incident energy, studying the three systems, $^{124}Xe +^{64} Ni$, $^{124}Sn +^{64} Ni$ and $^{112}Sn +^{58} Ni$, around 20 $AMeV$ with stable beams and at lower energies (< 15 $AMeV$) with future radioactive beams at SPES [74, 75].

Appendix A

Cavata method to estimate impact parameter

In HI reactions at intermediate and relativistic energies, total charge particles multiplicity (total number of particles detected in each event) is correlated with the violence of the collision and, thus, to the impact parameter [29]. More precisely, multiplicity mean value decreases monotonously as a function of b. In order to extract a quantitative relation between measured multiplicity and impact parameter, it's necessary to do some assumptions. The first assumption is that the total nucleus-nucleus cross section is well approximated by the geometrical cross section $\sigma_g = \pi(R_T + R_P)^2$, where R_T and R_P are the equivalent hard-sphere radii of target and projectile nuclei respectively. Considering the reaction cross section as a function of the squared impact parameter, it results costant $\frac{d\sigma_g}{d(b^2)} = \pi$ up to the maximum value $(R_T + R_P)^2$ of b^2, while it is zero beyond this value.
Using a procedure, that is rigorous if there is no dispersion in the correlation between multiplicity and impact parameter, it's possible to associate the integral S of the measured reaction cross section $\sigma(M)$ to any value m of the multiplicity, from m to ∞:

$$S = \sum_{M=m}^{\infty} \sigma(M); \tag{A.1}$$

it is also possible to associate to m the impact parameter B:

$$\int_0^{B^2} \frac{d(b^2)d\sigma_g}{d(b^2)} \Rightarrow B^2 = \frac{S}{\pi}. \tag{A.2}$$

This procedure, though a finite dispersion is always present, should remain valid as long as the correlation is large enough in comparison to the dispersion [70].
During CHIMERA aquisition runs, usually, a telescope is used as monitor and putted in OR with the global triggering condition. For InKiIsSy experiment, this telescope was located in ring 1I (tel. no. 9), thus covering polar angle θ between 1^o and $1.^o8$, that is

inside the grazing angle for $^{124}Xe +^{64} Ni$ ($\theta_{gr}^{lab} = 2.37^o$) and $^{124}Xe +^{64} Zn$ ($\theta_{gr}^{lab} = 2.55^o$) reactions calculated according to nuclear tables of Wilcke [71] and defined as angle at which $\sigma_{ELASTIC}/\sigma_{RUTH} = 1/4$; thus, this telescope measures elastic cross section giving information about integrated incident current N_B.

Specifically, the multiplicity dependent reaction cross section $\sigma(M_c)$ is given by the following formula:

$$\sigma(M_c) = \frac{N_{Mc}}{N_B * N_T} \tag{A.3}$$

where N_{Mc} is the number of events with total charged particles multiplicity M_c, N_B is the number of particles impinging on the target, and N_T is the number of target nuclei per unit area. In order to evaluate N_B, a "Rutherford normalization" is performed, assuming that the theoretical cross section for Rutherford scattering inside angular range of monitor telescope is related to measured counts in monitor telescope:

$$\sigma_R^{tel=9} = \int_0^{\pi/8} \int_{\vartheta_1=1^o}^{\vartheta_2=1.8^o} \frac{d\sigma_R}{d\Omega} * sin(\vartheta) d\vartheta d\varphi = \frac{N_R^{tel=9}}{N_B * N_T}, \tag{A.4}$$

where N_R is given by the elastic peak registered in monitor telescope while the theoretical cross section σ_R has been calculated using the Rutherford elastic scattering cross section. From A.4, it follows:

$$\frac{1}{N_B * N_T} = \frac{\sigma_R^{tel=9}}{N_R^{tel=9}}. \tag{A.5}$$

Thus, relation A.3 becomes

$$\sigma(M_c) = \frac{N_{Mc} * \sigma_R^{tel=9}}{N_R^{tel=9}}. \tag{A.6}$$

Figure A.1 presents the obtained $\sigma(M_c)$ distribution, assuming an error of $\pm 10\%$ in $1/(N_B * N_T)$. For each value of multiplicity, S and b values are calculated using eq. A.1 and A.2, respectively. The relation between the multiplicity and the estimated impact parameter b is shown in fig. A.2.

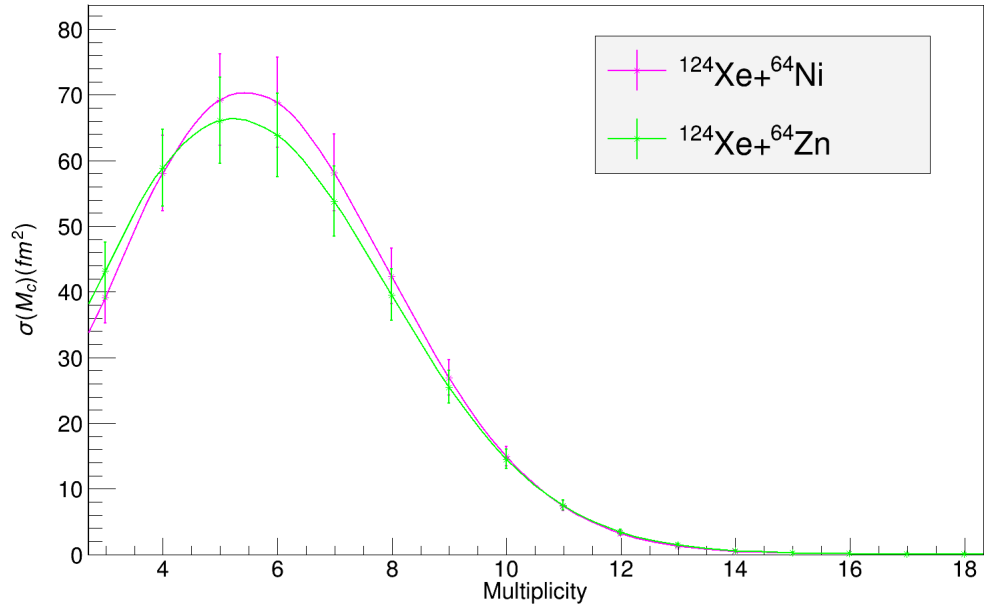

Figure A.1: Extrapolated cross section versus multiplicity for the $^{124}Xe +^{64} Ni$ (pink line) and $^{124}Xe +^{64} Zn$ (green line).

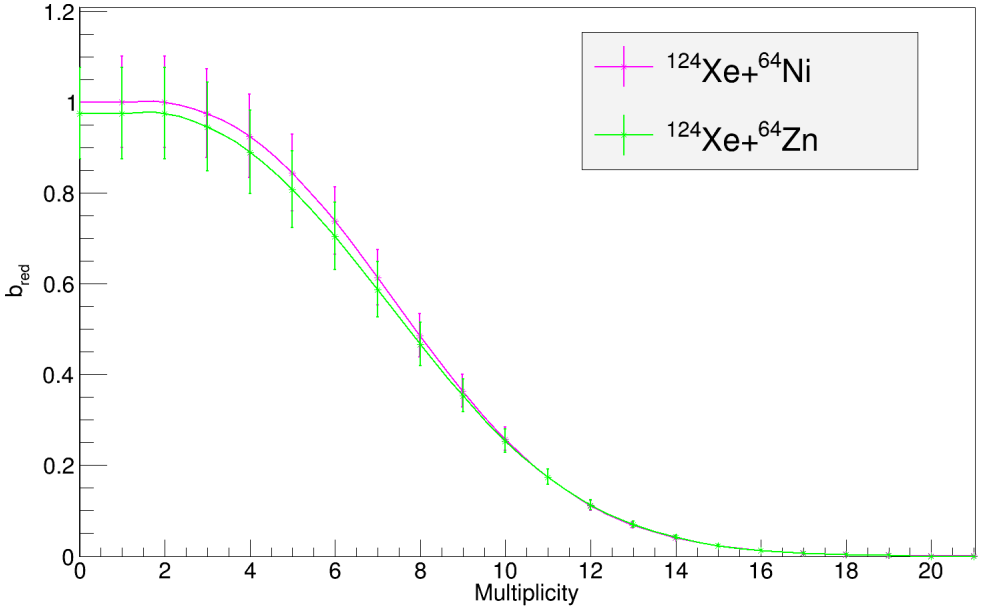

Figure A.2: Estimated reduced impact parameter $b_{red} = b/b_{max}$ versus multiplicity for $^{124}Xe+^{64} Zn$ (green line) and $^{124}Xe +^{64} Ni$ (pink line) systems at 35 $AMeV$.

Appendix B

Perspectives

In order to reproduce both "fast" light IMFs emission and heavy IMFs production in sequential PLF decay, the $^{124}Xe +^{64} Ni$ system has been investigated with a preliminary theoretical simulation in the frame of the constrained molecular dynamics, CoMD-III, code [72]. CoMD was used to describe the main features of dynamical emission phenomena in $^{124}Sn+^{64}Ni$ reaction at 35 $AMeV$ [5] (see section 1.3.1). In these preliminary calculations standard code parameters have not been varied; the $^{124}Xe +^{64} Ni$ has been simulated up to 650 fm/c. Moreover, GEMINI code [73] has been used to reproduce statistical de-excitation of hot particles. Thus, theoretical data have been analyzed as the experimental ones. Figures B.1 and B.2 show the results of CoMD-III calculations for the distribution of fragments as a function of their atomic number Z and their longitudinal velocity for the three biggest fragments with $Z \geq 3$ and the $cos(\theta_{prox})$ distributions for different mass asymmetry, respectively. In figure B.3, the comparison between the results of CoMD-III + GEMINI theoretical calculations and the experimental ratio of the dynamical component respect to the dynamical+statistical one as a function of the IMF atomic number for the $^{124}Xe +^{64} Ni$ reaction is shown. For these results, no detectors setup filter has been applied; however the data comparison seems very promising. In the future there is the possibility to extend these studies at lower beam incident energy, studying the three systems, $^{124}Xe+^{64}Ni$, $^{124}Sn+^{64}Ni$ and $^{112}Sn+^{58}Ni$, around 20 $AMeV$ with stable beams and at lower energies (< 15 $AMeV$) with future radioactive beams at SPES [74, 75].

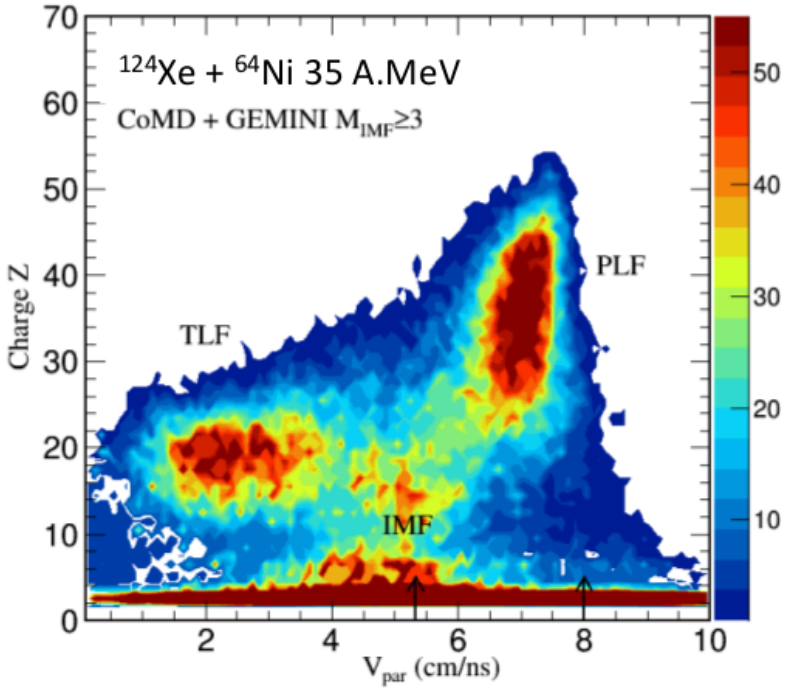

Figure B.1: Charge Z vs parallel velocity V_{par} plot for the three biggest fragments with $Z \geq 3$ for $^{124}Xe + ^{64}Ni$ system evaluated with the CoMD-III model.

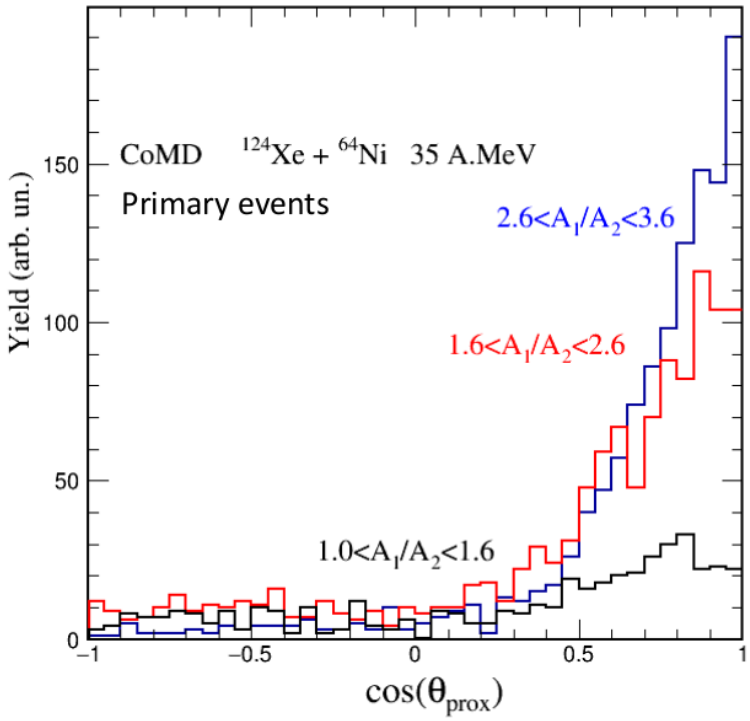

Figure B.2: $Cos(\theta_{prox})$ angular distributions for $^{124}Xe + ^{64}Ni$ system evaluated with the CoMD-III model, for different mass asymmetry.

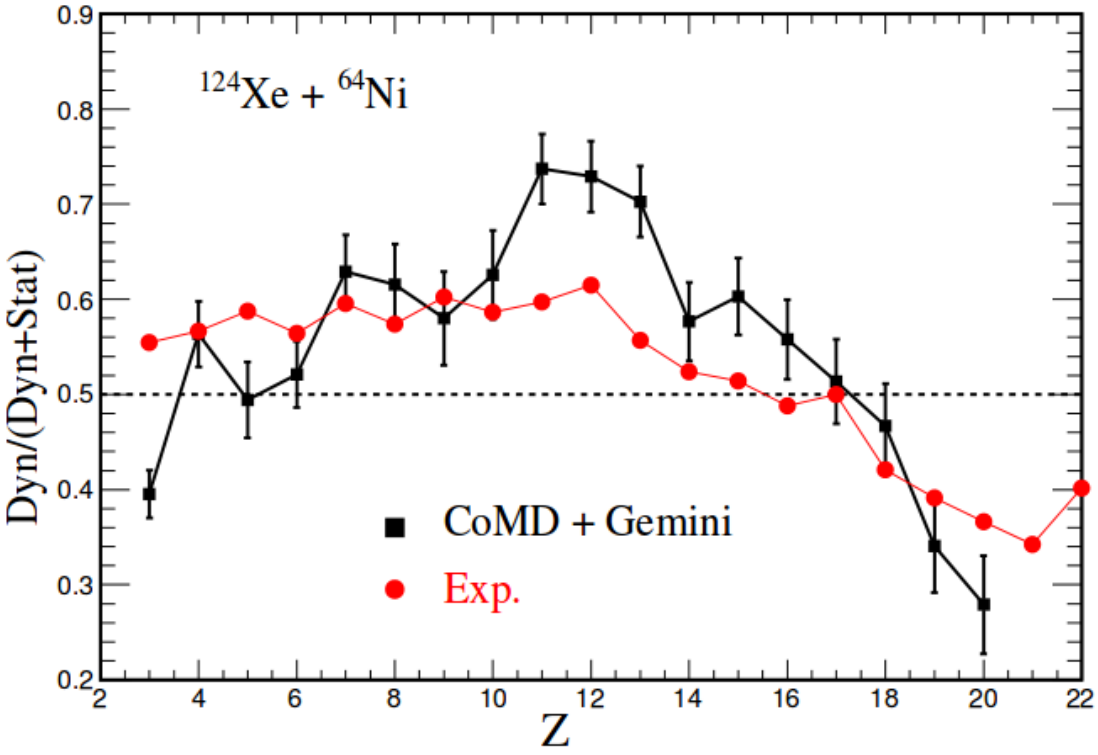

Figure B.3: Comparison between the experimental ratio of dynamical component respect to dynamical+statistical one as a function of the IMF atomic number (red circles) and the results of CoMD-III + GEMINI theoretical calculations (black squares) for the $^{124}Xe + ^{64}Ni$ reaction.

Bibliography

[1] E. De Filippo *et al.*, Phys. Rev. C 71, 044602 (2005).

[2] P. Russotto *et al.*, Phys. Rev. C 81, 064605 (2010).

[3] P. Russotto *et al.*, Phys. Rev. C 91, 014610 (2015).

[4] G. Giuliani *et al.*, Procs. of IWM2007, 311 (2007).

[5] M. Papa *et al.*, Phys. Rev. C 75, 054616 (2007).

[6] W.U. Schroder and J. Toke, 417, Nonequilibrium Physics at Short Time Scales(2004).

[7] C.P. Montoya *et al.*, Phys. Rev. Lett. 73, 3070 (1994).

[8] J.F. Lecolley *et al.*, Phys. Lett. B 354, 202 (1995).

[9] A.A. Stefanini *et al.*, Zeit. Phys. A 351, 167 (1995).

[10] E. De Filippo *et al.*, Phys. Rev. C 71, 064604 (2005).

[11] L.G. Sobotka *et al.*, Phys. Rev. C 55, 2109 (1997).

[12] J. Colin *et al.*, Phys. Rev. C 67, 064603 (2003).

[13] F. Bocage *et al.*, Nucl. Phys. A 676, 391 (2000).

[14] J. Toke *et al.*, Phys. Rev. Lett. 75, 2920 (1995).

[15] A. Pagano *et al.*, Nucl. Phys. A 734, 504 (2004).

[16] E. De Filippo *et al.*, Phys. Rev. C 86, 014610 (2012).

[17] V.E. Viola *et al.*, Phys. Rev. C 31, 1550, (1985).

[18] J. Wilczynski *et al.*, Int. Jour. of Mod. Phys. E 14, 353 (2005).

[19] P. Russotto *et al.*, Int. Jour. Of. Mod. Phys. E15, 410 (2006).

[20] P. Paul *et al.*, Annu. Rev. Nucl. Sci. 44, 65 (1994).

[21] J. Wilczynski *et al.*, Phys. Rev. C 54, 325 (1996).

[22] N. Bohr *et al.*, Phys. Rev. C 56, 426 (1939).

[23] P. Glassel *et al.*, Zeit. Phys. A 310, 189 (1983).

[24] G. Casini *et al.*, Phys. Rev. Lett. 71, 2567 (1993).

[25] D.J. Hinde *et al.*, Phys. Rev. C 45, 1229 (1992).

[26] W.Q. Shen *et al.*, Phys. Rev. C 36, 115 (1987).

[27] L. Stuttgé *et al.*, Nucl. Phys. A 539, 511 (1992).

[28] G. Poggi *et al.*, Nucl. Phys. A 685, 296c-311c (2001).

[29] Cavata *et al.*, Phys. Rev. C 42, 1760 (1990).

[30] P. Russotto *et al.*, Journal of Physics 515, 012020 (2014).

[31] P. Russotto, Ph.D. thesis, Università di Catania (2006).

[32] D. Lacroix, A.V. Lauwe and D. Durand, Phys. Rev. C 69, 054604 (2004).

[33] W. Gawlikowicz, TWI Report ZFGM-03-02, The software replica of CHIMERA multidetector (2003).

[34] V. Baran, M. Colonna and M. Di Toro, Nucl. Phys. A 730, 329 (2004).

[35] M. Papa, T. Maruyama, and A. Bonasera, Phys. Rev. C 64, 024612 (2001).

[36] M. Colonna *et al.*, Nucl. Phys. A 589, 160 (1995).

[37] F. Haddad *et al.*, Zeit. Phys. A 354, 321 (1996).

[38] E. V. Pagano *et al.*, EPJ Web of Conf. 117, 10008 (2016).

[39] J. Kemmer, Nucl. Instr. and Method A 226, 89 (1984).

[40] H.A. Rijken *et al.*, Nucl. Instr. and Method B 64, 272 (1992).

[41] S. Aiello *et al.*, Nucl. Instr. and Method A 369, 50 (1996).

[42] P. Kreutz *et al.*, Nucl. Instr. and Method A 260, 120 (1987).

[43] R.J Meijer *et al.*, Nucl. Instr. and Method A 264, 285 (1988).

[44] M.Alderighi et al, Nucl. Phys. A 734, E88-E91 (2004).

[45] M.Alderighi et al, IEEE Trans Nucl. Sci. 52, 1624 (2006).

[46] S. Aiello *et al.*, IEEE Trans Nucl. Sci. 45, 1798 (1998).

[47] S. Aiello *et al.*, IEEE Trans Nucl. Sci. 45, 1877 (1998).

[48] S. Aiello *et al.*, Nucl. Instr. and Meth. B 136, 1172 (1998).

[49] S. Aiello *et al.*, IEEE Trans Nucl. Sci. 47, 114 (2000).

[50] S. Aiello *et al.*, IEEE Trans Nucl. Sci. 47, 196 (2000).

[51] M.Alderighi *et al.*, IEEE Trans. Nucl. Sci. 49, 432 (2002).

[52] GANIL Grand Accelerateur Nationals d'Ions Lourds. https://lise.nscl.msu.edu/lise.html

[53] A. Pagano *et al.*, Nucl. Phys. A 681, 331 (2001).

[54] H. A. Bethe, Ann. Phys. 5, 325 (1930).

[55] D. Guinet *et al.*, Nucl. Instr. and Meth. A 278, 614 (1989).

[56] M.Alderighi *et al.*, Nucl. Instr. and Meth. A 489, 257 (2002).

[57] W.F. Schneider *et al.*, Nucl. Instr. and Method 87, 253 (1970).

[58] G. Lanzalone *et al.*, LNS Activity Report, 125, TOF calibration of CHIMERA silicon detector (2004).

[59] Ortec Fast-Timing Discriminator.

[60] C. Boiano *et al.*, IEEE Transactions on nuclear science vol. 51, n.5 (2004).

[61] C. Boiano *et al.*, IEEE Nuclear ScienceSymposium Conference Record (2007).

[62] W.D. Emmerich *et al.*, Nucl. Instr. and Method 83, 131 (1970).

[63] G. Pausch, W. Bohne, D. Hilscher, Nucl. Instr. and Method in Physics Research A 337, 573 (1994).

[64] J.B.A. England *et al.*, Nucl. Instr. and Method A 280, 291 (1989).

[65] J. Han, Psdfit Program (2010).

[66] E. De Filippo, Talk at IWM 2016 Ganil, Caen (2016).

[67] M. Papa *et al.*, Procs. of International Workshop on Multifragmentation and related topics (2005).

[68] D.J. Hinde *et al.*, Nucl. Phys A 354, 318 (1987).

[69] D. Hilscher and H. Rossner, Ann. Phys. 17, 471 (1992).

[70] G. Cugnon and D. L'Hote, Nucl. Phys. A 397, 519 (1983).

[71] W. Wilcke, Atomic Data 25, Num. 5 (1980).

[72] M. Papa *et al.*, Phys. Rev. C 87, 014001 (2013).

[73] R.J. Charity *et al.*, Phys. Rev. C 82, 014610 (2010).

[74] Newchim collaboration, SPES Letter Of Intent (2016).

[75] C. Rizzo *et al.*, Phys. Rev. C 90, 054618 (2014).